

Resistive switching in $\text{Pt}/\text{TiO}_2/\text{Pt}$

Doo Seok Jeong

Schriften des Forschungszentrums Jülich
Reihe Information / Information

Band / Volume 6

Forschungszentrum Jülich GmbH
Institute of Solid State Research (IFF)
Electronic Materials (IFF-6)

Resistive switching in Pt/TiO₂/Pt

Doo Seok Jeong

Schriften des Forschungszentrums Jülich
Reihe Information / Information
ISSN 1866-1777

Band / Volume 6
ISBN 978-3-89336-579-1

Bibliographic information published by the Deutsche Nationalbibliothek.
The Deutsche Nationalbibliothek lists this publication in the Deutsche
Nationalbibliografie; detailed bibliographic data are available in the
Internet at <http://dnb.d-nb.de>.

Publisher
and Distributor: Forschungszentrum Jülich GmbH
Zentralbibliothek, Verlag
D-52425 Jülich
phone: +49 2461 61-5368 · fax: +49 2461 61-6103
e-mail: zb-publikation@fz-juelich.de
Internet: <http://www.fz-juelich.de/zb>

Cover Design: Grafische Medien, Forschungszentrum Jülich GmbH

Printer: Grafische Medien, Forschungszentrum Jülich GmbH

Copyright: Forschungszentrum Jülich 2009

Schriften des Forschungszentrums Jülich
Reihe Information / Information Band / Volume 6

D 82 (Diss., RWTH Aachen, Univ., 2008)

ISSN 1866-1777
ISBN 978-3-89336-579-1

The complete volume is freely available on the Internet on the Jülicher Open Access Server (JUWEL) at <http://www.fz-juelich.de/zb/juwel>

Neither this book nor any part may be reproduced or transmitted in any form or by any means, electronic or mechanical, including photocopying, microfilming, and recording, or by any information storage and retrieval system, without permission in writing from the publisher.

Kurzfassung

In letzter Zeit hat das resistive Schalten von TiO_2 im Hinblick auf eine Anwendung in "resistive random access memory" (RRAM) vermehrt Aufmerksamkeit auf sich gezogen. TiO_2 zeigt charakteristisches nichtflüchtiges resistives Schalten zwischen einem hochohmigen (HRS) und einem niederohmigen Zustand (LRS). Sowohl unipolares als auch bipolares Schalten in Abhängigkeit von der jeweils verwendeten Strombegrenzung während der Elektroformierung wurden in TiO_2 beobachtet.

Im Rahmen dieser Arbeit ist die charakteristische Strom-Spannungs (*I-V*) Hysterese von drei verschiedenen Ausgangszuständen, unformiert, unipolar aktiviert und bipolar aktiviert, untersucht und mittels der Bildung und Migration von Sauerstoffleerstellen erklärt worden. Die *I-V* Hysterese von unformiertem TiO_2 zeigte flüchtiges Verhalten, das durch eine zeitliche Änderung des Widerstandes zu erklären ist. Diese Änderung ist abhängig von der angelegten Spannung. Im Gegensatz dazu zeigten die unipolar und auch die bipolar formierten Zustände ein nichtflüchtiges Verhalten der Widerstände.

Es gibt einige Hinweise auf die Bildung von gasformigem Sauerstoff während der Elektroformierung, die sowohl durch TOF-SIMS, "time-of-flight secondary ion mass spectroscopy", als auch durch die beobachtete morphologische Änderung der Schaltzellen während der Formierung gestützt werden. Unter der Annahme, dass eine große Anzahl an Sauerstoffleerstellen während des Elektroformierungsprozesses induziert wurde, ist das *I-V* Verhalten von elektroformierten Schaltzellen durch eine Veränderung der Sauerstoffleerstellenverteilung innerhalb des TiO_x ($x \lesssim 2$) simuliert worden.

Die Simulation der bipolaren *I-V* Hysterese erfolgte unter der Berücksichtigung von Sauerstoff-Erzeugungs- bzw. Vernichtungsreaktionen an der Pt/TiO_x Grenzfläche. Diese Reaktionen sind eine Funktion der angelegten Spannung und bestimmen die Verteilung von Sauerstoffleerstellen in TiO_x . Resultierend daraus kann die Höhe der Schottky-Barriere an der Kathode/ TiO_x Grenzfläche durch die Änderung der Sauerstoffleerstellenverteilung beeinflusst werden. Daher kann das bipolare resistive Schalten einschließlich der Elektroformierung als eine elektrochemische Reaktion mit der Beteiligung von Sauerstoff verstanden werden.

Abstract

Recently, the resistive switching behavior in TiO_2 has drawn attention due to its application to resistive random access memory (RRAM) devices. TiO_2 shows characteristic non-volatile resistive switching behavior, i.e. reversible switching between a high resistance state (HRS) and a low resistance state (LRS). Both unipolar resistive switching (URS) and bipolar resistive switching (BRS) are found to be observed in TiO_2 depending on the compliance current for the electroforming.

In this thesis the characteristic current-voltage (I - V) hysteresis in three different states of TiO_2 , pristine, URS-activated, and BRS-activated states, was investigated and understood in terms of the migration of oxygen vacancies in TiO_2 . The I - V hysteresis of pristine TiO_2 was found to show volatile behavior. That is, the temporary variation of the resistance took place depending on the applied voltage. However, the I - V hysteresis of URS- and BRS-activated states showed non-volatile resistive switching behavior.

Some evidences proving the evolution of oxygen gas during electroforming were obtained from time-of-flight secondary ion mass spectroscopy analysis and the variation of the morphology of switching cells induced by the electroforming. On the assumption that a large number of oxygen vacancies are introduced by the electroforming process, the I - V behavior in electroformed switching cells was simulated with varying the distribution of oxygen vacancies in electroformed TiO_x ($x \lesssim 2$).

The I - V hysteresis undergoing the BRS was simulated with taking into consideration oxygen formation/annihilation reactions at a Pt/ TiO_x interface. The oxygen-related reactions given as a function of the applied voltage affect the distribution of oxygen vacancies in TiO_x , consequently, the Schottky barrier height at the cathode/ TiO_x interface is influenced by the oxygen vacancy distribution. Therefore, the BRS behavior including the electroforming characteristics could be understood in terms of the oxygen-related electrochemical reactions.

Contents

Contents	i
Introduction	v
1 Overview on the resistive switching in transition metal oxides	1
1.1 Bipolar and unipolar resistive switching	1
1.2 Resistive switching mechanism	2
1.2.1 Fuse-antifuse of conduction paths	3
1.2.2 Resistive switching induced by anion migration	4
2 Sample preparation	7
2.1 Sputtering of TiO ₂ and Pt	7
2.2 Fabrication of Pt/TiO ₂ /Pt stack resistive switching cells	9
2.3 Fabrication of planar resistive switching cells	9
2.4 Fabrication of modified stack switching cells	10
3 Structural and chemical properties of pristine TiO₂	13
3.1 Microstructural characteristics	13
3.2 Chemical characteristics	16
4 Electrical properties of pristine TiO₂	19
4.1 Current-voltage-time characteristics	19
4.1.1 Electrical conduction theory	19
4.1.2 Current-voltage characteristics of Pt/TiO ₂ /Pt	21
4.1.3 Current-time characteristics of Pt/TiO ₂ /Pt	26
4.2 Impedance spectra of Pt/TiO ₂ /Pt	29
4.2.1 Dielectric behavior in time and frequency domains	30
4.2.2 Impedance behavior in the frequency domain (60 Hz - 1 MHz)	33
4.2.3 Impedance behavior in the frequency domain (0.1 Hz - 100 kHz)	35
5 Electroforming characteristics in bipolar resistive switching	39
5.1 Electroforming effect on the structural and chemical properties	39
5.1.1 Electroforming theory	41
5.1.2 Structural changes by the electroforming	42
5.1.3 Resistance degradation using conductive atomic force microscope	45
5.1.4 Chemical changes by the electroforming	45
5.1.5 Calculation of the Joule heating during the electroforming	47

CONTENTS

5.2	Electroforming effect on the electrical conduction behavior of TiO_2	48
5.2.1	Electroforming with a voltage source	48
5.2.2	Electroforming with a current source	53
5.3	Modeling of the conduction behavior in the electroformed TiO_2	59
5.3.1	Calculation of the voltage distribution in $\text{Pt}/\text{TiO}_x/\text{Pt}$	61
5.3.2	Numerical calculation of the electric conduction behavior	62
5.3.3	Algorithm of the calculation	64
5.3.4	Calculation results	65
6	Unipolar resistive switching behavior	71
6.1	Electroforming for unipolar resistive switching	71
6.2	Unipolar resistive switching characteristics	72
6.2.1	Unipolar resistive switching in stack switching cells	73
6.2.2	Unipolar resistive switching in modified stack switching cells .	78
6.2.3	Impedance spectroscopy	80
7	Bipolar resistive switching behavior	85
7.1	Voltage-controlled BRS measurements	85
7.1.1	Polarity dependence of the BRS	85
7.1.2	Pad-size dependence of the BRS	88
7.1.3	Abnormal BRS behavior	89
7.2	Current-controlled BRS measurements	95
7.2.1	BRS measurements in vacuum	96
7.3	Electrical conduction behavior in the HRS and the LRS	98
7.3.1	Current-voltage characteristics at various temperatures	99
7.3.2	Current-time characteristics at various constant voltages	102
7.4	Transition to unipolar resistive switching characteristics	102
7.5	Modeling of the BRS behavior	103
7.5.1	Electrochemical reaction through the Helmholtz layer	103
7.5.2	Drift-diffusion of oxygen vacancies and electrons in TiO_x	107
7.5.3	Finite difference method for the calculation	109
7.5.4	Calculation results	114
Summary		123
Bibliography		127
Curriculum vitae		131

Acknowledgements

I would like to thank my official advisor *Professor Dr. Rainer Waser* for inspiring me with initiative and supporting excellent research facilities. I thank *Professor Dr. Günter Gottstein* for his interest in this work and being the co-examiner. I thank my advisor *Professor Dr. Herbert Schroeder* for supporting my research for this thesis and fruitful discussions all the time. The financial support of the *DAAD (Deutscher Akademischer Austausch Dienst)* for my research at the Forschungszentrum Jülich GmbH is greatly acknowledged.

- I thank *Professor Krystof Szot* for the AFM and the XPS analysis and precious discussions.
- I thank *Dr. Paul Meuffels* for keen advices for my research and kind help for impedance spectroscopy.
- I thank *Professor Dr. Cheol Seong Hwang* for fruitful discussion and advice.
- I thank *Dr. Uwe Breuer* for SIMS analysis and fruitful discussion.
- I thank *Tobias Menke* for helping me with switching measurements in vacuum.
- I thank *Dr. Adrian Petraru* for helping me with the reactive ion beam etching.

If it had not been for friends I have met in Jülich, my three-year life would have been lonely. Among many good intimate friends, I would like to thank *Christina Schindler* and *Mathias Schindler* for helping me a lot with adjusting myself to Jülich as friends and as colleagues sometimes. I thank *Dr. Martin Weides* for fruitful discussion on the business out of research. I thank *Sebastian Gliga* for being a kind dinnermate many days. I greatly acknowledge *Dr. Reji Thomas'* encouragement helping me with being on the track all the time. Last, I am grateful for the devotion of my parents and the support of my sisters.

Thank you very much!
Jülich, April 2008
Doo Seok Jeong

Introduction

Resistive switching of transition metal oxide (TMO) materials including TiO_2 [1–3], NiO [4, 5], and Nb_2O_5 [6] as well as perovskite-type oxides including SrZrO_3 [7, 8], $\text{Pb}(\text{Zr,Ti})\text{O}_3$ [9], and SrTiO_3 [10] is a very attractive subject of technical and scientific research. These materials show characteristic bistable resistance states, a high resistance state (HRS) and a low resistance state (LRS). Recently, studies to apply TMOs to resistive random access memory (RRAM) devices have been performed because of advantages, such as the high off/on ratio and the low inherent scaling problem compared to capacitance-based RAMs and even other resistance-based RAMs, such as phase change RAM (PcRAM) and magnetic RAM (MRAM).[11] Furthermore, some materials show multi-stable resistive switching behavior so that they have possibility to be applied to multi-bit operation devices.[12] However, the resistive switching of TMOs needs large current ($> 1 \text{ mA}$) for the reset switching (LRS \rightarrow HRS). As the density of integrated circuits increases, the size of the complementary metal-oxide-semiconductor (CMOS) shrinks according to the design rule. The channel area of the CMOS shrinks as well following the design rule so that the current provided through the channel decreases. Therefore, the large reset current hinders the application of TMOs to integrated RRAM devices.

Resistive switching behavior can be classified into unipolar resistive switching (BRS) and bipolar resistive switching (URS). URS behavior has been often observed in binary TMO such as TiO_2 , NiO , and Nb_2O_5 . The URS operation is barely dependent on the applied voltage polarity so that if a voltage as high as the switching voltage is applied the URS operation can be achieved regardless of the voltage polarity. Unlike the URS, the BRS depends on the applied voltage polarity. If the reset switching occurs under one voltage polarity, the set switching (HRS \rightarrow LRS) occurs under the other polarity. Therefore, the applied voltage as well as the voltage polarity should satisfy a proper switching condition for the BRS operation. The BRS has been often observed in perovskite-type oxides such as SrZrO_3 , $\text{Pb}(\text{Zr,Ti})\text{O}_3$, and SrTiO_3 . The BRS has been also observed in cation-doped glass materials such as Ag-doped GeSe_x [13], Ag-doped As_2S_3 [14], and Cu-doped SiO_x [15].

The resistive switching behavior in TMOs has been frequently explained in terms of the formation and rupture of conduction paths.[2, 3, 10] Owing to the advancement of microscopic observation technologies, e.g. scanning tunneling microscopy and atomic force microscopy, indications for the generation and rupture of local conduction paths as the mechanism of the resistive switching have been found, which support the conduction path model.[2, 10] Since the first report on oxide insulator by Hickmott[16], the resistive switching in TMOs has been studied for decades, nevertheless, the detail of the mechanism has been still not clearly identified leaving many

open questions.

The mechanism of URS might be the fuse-antifuse of conduction paths by the applied electric energy to switching cells. Considering very high power dissipation in the local conduction paths during the voltage or current application, the fuse-antifuse of the conduction paths by the Joule heating might explain the URS behavior.

Concerning the mechanism of BRS, has been suggested up to now, BRS can be classified into anion- and cation-migration-induced BRS and electronic BRS. The anion-migration-induced BRS includes the BRS in perovskite-type oxides and some binary TMOs. The migration of anions, due to the drift-diffusion, and their electrochemical reactions at the interface between the anode and the switching material leads to changes in the resistance.[10, 17, 18] That is, the BRS is attributed to an intrinsic element rather than extrinsic elements, for instance, an electrode material. The cation-migration-induced BRS includes the BRS in cation-doped glass materials and some crystalline materials with diffusive electrode. This BRS is attributed to the migration of extrinsic cations, doped cations or diffusing cations from electrode. The electronic BRS deals with the resistive switching resulting from the change in electronic transport behavior including the electronic charge injection at the cathode, and the trapping and de-trapping of electronic carriers.[19]

The purpose of this work is to investigate the electric conduction characteristics of non-doped TiO_2 in various resistance states, pristine, BRS-activated, and URS-activated states and the correlation between the structural and chemical change in TiO_2 , due to electroforming, and the accompanying change in the current-voltage behavior. And it is also the purpose of this work to suggest the proper mechanism of the resistive switching based on experimental observations.

This thesis is divided into seven chapters. In Chapter 1 the overview on the resistive switching behavior in transition metal oxides is given. Chapter 2 gives the preparation procedure of three different resistive switching cells, a stack, a planar, and a modified stack switching cell. Chapter 3 shows the microstructural and the chemical properties of pristine TiO_2 . The crystal structure, the microstructural characteristics, and the stoichiometry of the pristine TiO_2 are identified by various techniques. Chapter 4 gives the electrical properties of pristine TiO_2 . The current-voltage-temperature and the current-time relations are presented and the impedance spectra in a wide frequency range are also explained. Chapter 5 contains the electro-forming characteristics of TiO_2 and the modeling of the electric conduction behavior in electroformed switching cells. Electroforming is performed on the three different switching cells with various parameters such as voltage/current polarity, compliance current, voltage, and the atmosphere. The structural and the chemical variations induced by the electroforming are explained, suggesting that the electroforming is due to an electrochemical reaction involving the evolution of oxygen gas. Finally, the mechanism of the current-voltage behavior in electroformed switching cells is suggested in terms of the reduced schottky barrier height at the cathode/ TiO_x interface due to the presence of the oxygen vacancies introduced by the electroforming. Chapter 6 discusses the URS behavior of TiO_2 . The characteristics of the URS and the impedance spectra of TiO_2 in various resistance states are presented. In Chapter 7 the BRS behavior of TiO_2 with different thicknesses and different pad-size is given. The mechanism of the BRS is finally suggested in terms of an electrochemical

reaction involving oxygen ions.

Please note that in the text the term “ TiO_x ” means the oxygen-loss titanium oxide phase composing a conduction path and “ TiO_2 ” denotes pristine stoichiometric TiO_2 or the whole titanium oxide film including the conduction paths consisting of TiO_x .

Chapter 1

Overview on the resistive switching in transition metal oxides

In this chapter the overview on resistive switching behavior and materials is presented. In a broad meaning resistive switching materials can include giant magnetoresistance materials such as NiFe, CoFe, and Co and phase change materials such as $Ge_xSb_yTe_z$. However, this study covers the transition metal oxides showing resistive switching behavior. The resistive switching behavior in the transition metal oxides can be classified into two categories, unipolar resistive switching and bipolar resistive switching. The mechanism of unipolar resistive switching is estimated to be the fuse-antifuse of conduction paths. The fuse-antifuse-based resistive switching has been observed in many binary transition metal oxides. The mechanism of bipolar resistive switching is considered to be the migration of anions. The anion-migration-based resistive switching has been most often observed in perovskite-type oxides so that 'anion' mainly denotes an oxygen ion. Brief overview on both resistive switching categories are presented.

1.1 Bipolar and unipolar resistive switching

Resistive switching shows hysteretic current-voltage (I - V) behavior denoting the switching between two characteristics resistance states, a high resistance state (HRS) and a low resistance state (LRS). The resistive switching between the HRS and the LRS can be achieved by controlling the applied voltage. The switching from the HRS to the LRS is termed set switching and the switching the other way than the set switching is termed reset switching. If a voltage as high as one switching voltage is applied to a switching cell, the resistive switching takes place, that is, unless the applied voltage is as high as the switching voltage, no change in the resistance state takes place. This nonvolatile resistive switching behavior can be applied to nonvolatile memory devices.

Resistive switching can be classified into bipolar resistive switching (BRS) and unipolar resistive switching (URS). In URS resistive switching behavior is not dependent on the applied voltage polarity. Namely, the polarity of switching voltage does

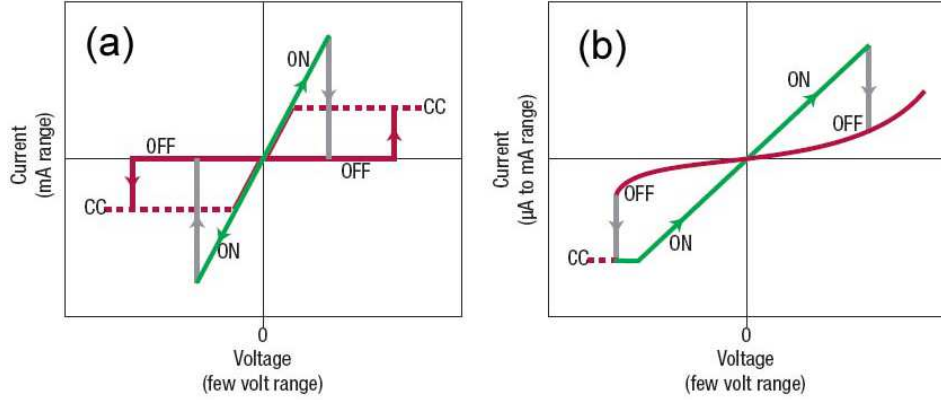


Figure 1.1: Schematic I - V curve of (a) URS and (b) BRS[20]

not influence the following switching behavior. For instance, if set switching takes place under one voltage polarity, the following reset switching can takes place under both voltage polarities. Therefore, an amount of the voltage applied to a switching cell is important for the URS operation rather than the applied voltage polarity. In BRS an amount of voltage as well as the applied voltage polarity plays a very crucial role in the resistive switching. The set and the reset switching voltages are opposite to each other. If the set switching takes place under one voltage polarity, the reset switching takes place under the other voltage polarity. Therefore, both an amount of the applied voltage and its polarity must satisfy proper conditions for the BRS operation unlike the URS. Schematic I - V curves of the URS and the BRS are depicted in Fig. 1.1. Compliance current is an important parameter for URS operation. At the moment when the set switching takes place the current abruptly increases so that the switching cell will undergo kind of permanent dielectric breakdown without setting compliance current. Therefore, the compliance current plays a role in avoiding the dielectric breakdown during the set switching of the URS. For the reset switching the compliance current used for the set switching should be deactivated because the reset current is normally higher than the compliance current. Otherwise, no reset switching will take place due to the lack of enough current. The compliance current is not necessary for the reset switching. For the BRS operation the compliance current is not necessary for some systems, for instance, the BRS in TiO_2 which will be mentioned in Chapter 7.

1.2 Resistive switching mechanism

Resistive switching mechanism has not been clarified yet leaving many open questions. Nevertheless, local conduction paths in a switching material are estimated to be involved in the resistive switching. Indeed, in many systems it has turned out that the resistance of the LRS is not scaled by the pad-size.[2, 7, 21, 22] From this observation it can be speculated that local conduction paths whose number can not be scaled by the pad-size exist in the insulating matrix. Electroforming plays a role

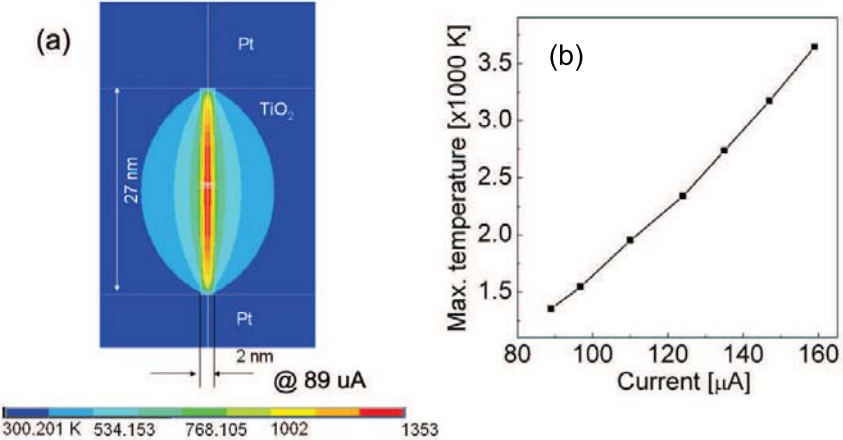


Figure 1.2: (a) Calculated temperature distributions in $\text{Pt}/\text{TiO}_2/\text{Pt}$ containing a conduction path under a current of $89 \mu\text{A}$. (b) Maximum temperature with respect to the applied current.

in the formation of the conduction paths. During the electroforming process a large amount of electric energy is provided for a switching cell so that the power dissipation in the cell is estimated to be high enough to change the local microstructure of the cell, forming the conduction paths.

1.2.1 Fuse-antifuse of conduction paths

The URS in many binary transition metal oxides falls into this category. The URS in binary transition metal oxides such as TiO_2 [1–3], NiO [4, 5], Nb_2O_5 [6] has been often reported. Considering URS characteristics, conduction paths are expected to be formed or ruptured by the applied voltage. At the reset switching the conduction paths become locally ruptured. The locally ruptured part of a conduction path has an insulating phase so that the overall resistance of the conduction path becomes insulating. Several literatures have reported that the rupture of the conduction path takes place at the anode.[23, 24] However, concerning the temperature distribution in the conduction path shown in Fig. 1.2, the antifuse of the conduction path is predicted to take place in the middle of the conduction path rather than the anode side. At the set switching the locally ruptured conduction paths can recover a conducting phase from an insulating phase so that the low resistance before the previous reset switching can be recovered. The reset switching can be attributed to local power dissipation in the conduction paths. Indeed, the remarkable increase in the temperature in the conduction paths due to the power dissipation can be identified using finite element analysis as shown in Fig. 1.2. The increase in the lattice temperature can lead to the phase transitions of the conduction paths although the detail of the reset switching is still obscure. In this sense the URS behavior is not different from the resistive switching in phase change materials.

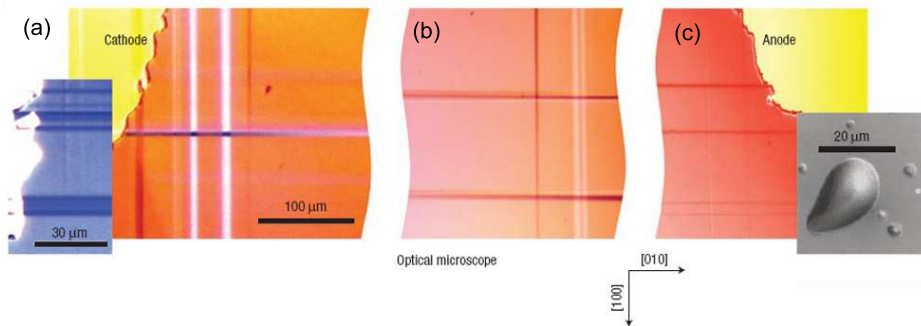


Figure 1.3: Optical microscope image of an electroformed undoped SrTiO_3 single crystal with two planar Au electrodes. (a), (b), and (c) show the region near the cathode, the central region, and the region near the anode, respectively. The left inset shows a probable fine filament structure at the cathode. The right inset shows the formation of gas bubble below the anode.[10]

1.2.2 Resistive switching induced by anion migration

The BRS in many perovskite-type ternary oxides falls into this category. The BRS behavior in $(\text{Ba},\text{Sr})\text{TiO}_3$ [25], SrZrO_3 [7, 8], SrTiO_3 [10], and $(\text{Pr},\text{Ca})\text{MnO}_3$ [18] has been frequently reported. Recently, it has been reported that TiO_2 shows not only URS but also BRS behavior.[26] The BRS in these systems is considered to be attributed to the migration of the anions (oxygen ions) and their reactions at the interface between the anode and the switching material. The conduction paths are considered to be composed of oxygen-deficient non-stoichiometric phases with a conductivity higher than that of the stoichiometric phase. Some clues indicating the oxygen ion-involved BRS behavior have been reported in some literatures.[10, 17, 18] Szot *et al.* have demonstrated that the BRS in undoped SrTiO_3 is due to the migration of the oxygen ions along the network of the extended defects and shown the evolution of oxygen gas at the anode as a result of the BRS operation.[10] Nian *et al.* have shown the difference of the resistive switching behavior between oxygen-sufficient and oxygen-deficient $(\text{Pr},\text{Ca})\text{MnO}_3$ films and measured the relaxation of the resistance. They have demonstrated that the relaxation of the resistance in the oxygen-deficient sample is attributed to the oxygen diffusion in $(\text{Pr},\text{Ca})\text{MnO}_3$ by solving the one-dimensional oxygen diffusion equation.[18] Janousch *et al.* have shown a more direct evidence indicating the role of oxygen vacancies in the formation of the conduction paths of a Cr-doped SrTiO_3 single crystal cell. They have shown the distribution of oxygen vacancies between two laterally located electrodes on the Cr-doped SrTiO_3 single crystal, which was obtained from Cr K-edge X-ray absorption near edge spectroscopy (XANES) spectra.[17] Indeed, the two electrodes were connected via oxygen vacancies by the electroforming. By these observations oxygen ion/vacancy migration and their reactions are judged to play a crucial role in the BRS behavior in the transition metal oxide switching cells.

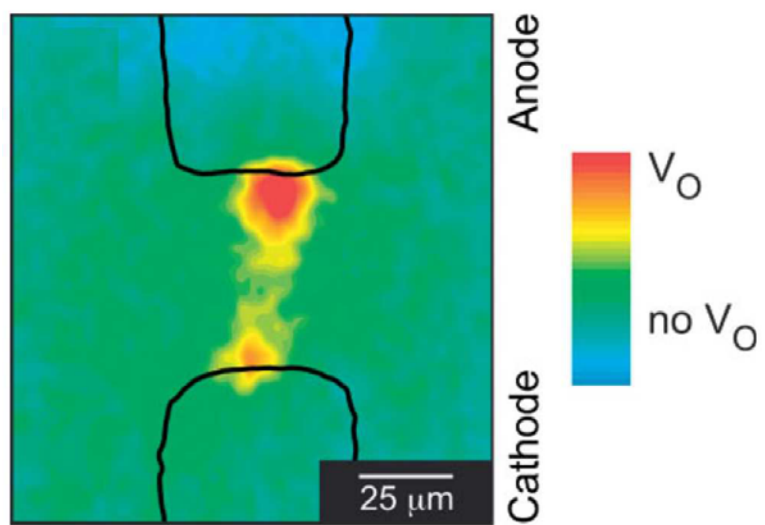


Figure 1.4: Cr X-ray fluorescence mapping showing the distribution of oxygen vacancies between the anode and the cathode.[17]

Chapter 2

Sample preparation

In this chapter the fabrication procedure of Pt/TiO₂/Pt resistive switching cells is introduced. For different purposes three different resistive switching structures i.e. stack, planar, and modified stack structures were fabricated using electron-beam and photo lithography techniques. Sputtering was used for both TiO₂ and Pt depositions.

2.1 Sputtering of TiO₂ and Pt

TiO₂ films were deposited using a Leybold Univex 450C magnetron sputtering system whose schematic is shown in Fig. 2.1(a). The robot arm in the transfer chamber moves wafers loaded in the load lock chamber to a Ti or Pt dc sputtering chamber, therefore, in situ deposition is possible. Ex-situ sputtering was mainly used for the patterned electrode. Using reactive sputtering TiO₂ could be deposited from a Ti metal target. The gas mixture of 77 % Ar and 23 % O₂ was injected into the chamber and a dc voltage was applied to the Ti target so that Ar+O₂ plasma could be generated. Plasma emits visible light resulting from the transition of electrons from excited states to the ground state so that the wave length of emitted light depends on the electronic structure of gas molecules. Ar+O₂ plasma emits red purple light since Ar emits purple light and O₂ red light. A schematic of reactive sputtering is shown in Fig. 2.1(b). An applied voltage is mainly dropped in the vicinities (sheaths) of cathode and anode because the electric field penetration depth in a glow region is very small due to a huge number of electrons and ionized gas molecules in a glow region. The momentum transfer from accelerated Ar⁺ ions in the sheath near the

Table 2.1: Sputtering parameters for TiO₂ and Pt depositions

materials	TiO ₂	Pt
Substrate temperature	room temp.	room temp.
Working pressure	2.2 Pa	1.35 Pa
Working gas composition	77 % Ar + 23 % O ₂	pure Ar
Presputtering time	300 s	30 s
Dc input power	300 W	375 W
Target diameter	4 inch	4 inch
Wafer dimension	1 × 1 inch ²	1 × 1 inch ²

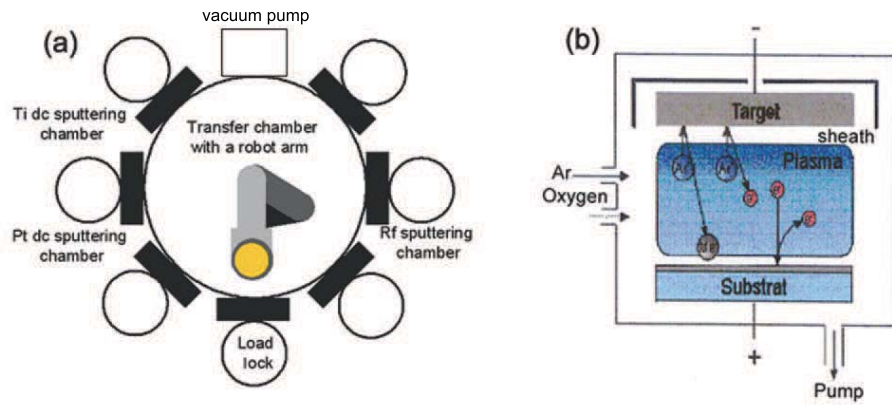


Figure 2.1: (a) Schematic layout of a Leybold Univex 450C; (b) Schematic of a sputtering process.

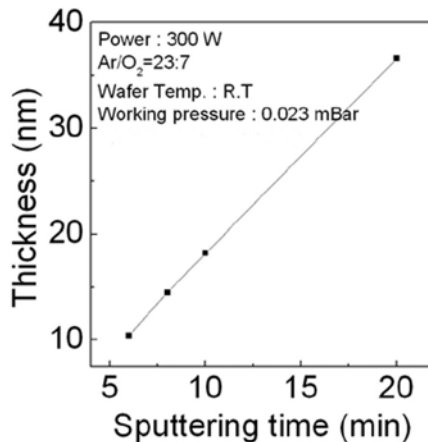


Figure 2.2: TiO_2 thickness with respect to sputtering time, measured by XRF.

cathode (Ti target) to Ti atoms on the target surface gives rise to the sputtering of Ti atoms. The sputtered Ti can react with O_2 molecules while they reach the substrate so that a TiO_2 film can be formed on the substrate. On the other hand, Pt was formed using dc sputtering in pure Ar atmosphere. The sputtering parameters for TiO_2 and Pt are shown in Table. 2.1.

Thickness of TiO_2 films was determined by the areal density of Ti atoms in deposited TiO_2 measured using x-ray fluorescence (XRF). The obtained areal density of Ti divided by the volume density of Ti gives the thickness of the TiO_2 films. The ideal volume density of Ti in TiO_2 anatase was taken as the volume density of Ti. Indeed, the sputter grown TiO_2 is found to have the anatase phase as will be

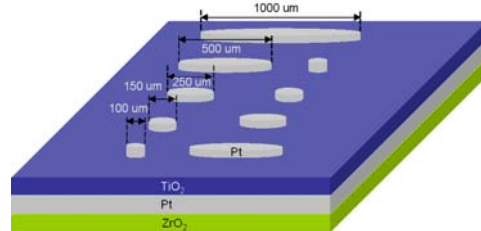


Figure 2.3: Schematic of a Pt/TiO₂/Pt stack resistive switching cell.

mentioned in Chapter 3. The determined film thickness with respect to sputtering time is shown in Fig. 2.2. The films were deposited on 100 nm thick sputter grown Pt substrates whose adhesion layer underneath Pt was ZrO_x instead of TiO_x. Using the ZrO_x adhesion layer is helpful to the correct XRF measurements by avoiding Ti signals from an adhesion layer. The XRF results were well-consistent with the film thicknesses determined from cross-sectional scanning electron microscope (SEM).

2.2 Fabrication of Pt/TiO₂/Pt stack resistive switching cells

Pt/TiO₂/Pt resistive switching cells with stack structures were fabricated. Blanket TiO₂ films were deposited on 100 nm thick sputter grown Pt substrates having a Pt/ZrO_x/SiO_x/Si structure with various sputtering times 15, 30, 45, and 60 mins corresponding to thicknesses of 27, 55, 75, and 100 nm, respectively. Top electrodes were patterned using a lift-off or a shadow mask process. Circular-shaped top electrodes with five different diameters, 100, 150, 250, 500, and 1000 μ m, were formed. For the lift-off process photoresist patterns were formed on a blanket TiO₂ layer, then dc sputtering for a 70 nm thick Pt film followed. Since the Pt sputtering was performed at room temperature, the sputtering barely imposed high heat on the photoresist so that the lift-off was successful. A schematic of the stack switching cell is shown in Fig. 2.3.

2.3 Fabrication of planar resistive switching cells

Concerning the study on the mechanism of resistive switching, the stack switching cells have the drawback that switching takes place in the volume of TiO₂ embedded in the structure, therefore, it is hardly possible to observe some clues of resistive switching mechanism using experimental techniques such as conductive atomic force microscope and SEM. Planar resistive switching cells have the advantage that the active area for resistive switching, considered to be in the gap between two electrodes, is exposed to the air so that observation of the active area is possible. An SEM image of the switching cell with a gap width of 100 nm is shown in Fig. 2.4(b) with an enlarged image of the gap in the inset. The fabrication procedure of this switching cell is as follows. First, a blanket TiO₂ layer was deposited on a SiN_x/SiO₂/Si substrate.

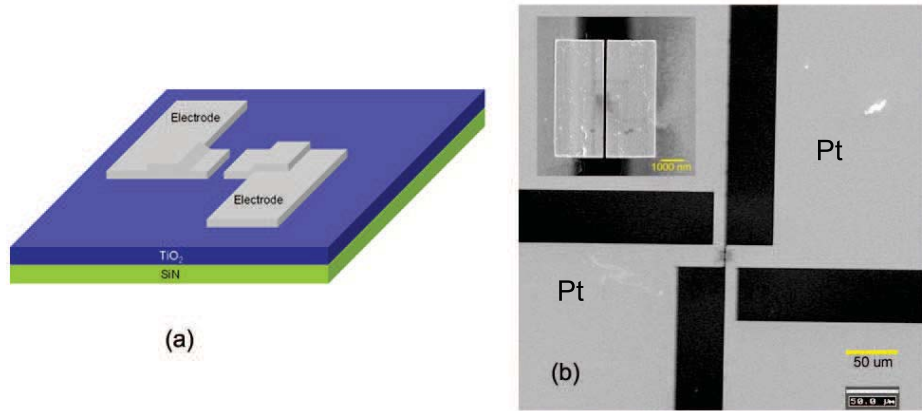


Figure 2.4: (a) Schematic of the planar switching cell. (b) Plane SEM image of the planar switching cell. The inset on the upper left side is an enlarged image of the gap between the two electrodes.

Coarse electrodes on the TiO₂ film as shown in the large area of Fig. 2.4(b) were patterned using photo lithography followed by Pt metallization. The smallest gap width between two electrodes which can be achieved by the photo lithography is about 1 μ m, which is considered to be too large to carry out electroforming with a reasonable applied voltage. Therefore, fine electrodes with a gap width as low as 100 nm as shown in the inset of Fig. 2.4(b) were patterned using electron-beam (e-beam) lithography after the coarse electrode formation. Polymethylmethacrylate (PMMA) was used as an e-beam resist for the direct e-beam lithography. Using spin coating a PMMA layer was coated and the gap was patterned by e-beam writing. Pt metallization followed the gap patterning. Electroforming voltage is considered to be proportional to gap width so that a planar cell with a large gap would show very high electroforming voltage which is hardly applied by normal voltage sources.[64] The detail of the electric transport characteristics of the planar switching cells will be given in Chapter 4.

2.4 Fabrication of modified stack switching cells

Modified stack switching cells were fabricated, where electric transport takes place along grain columns similar to the stack switching cell and experimental observations during or after resistive switching can be also obtained. Both top electrode (TE) and bottom electrode (BE) consist of a fine and thin electrode and a coarse and thick electrode as can be seen in Fig. 2.5. The configuration of the fine electrodes of the TE and the BE forms a small overlap where TiO₂ is in-between. The electrodes in the active (overlapped) region are thin so that the effect of resistive switching on the switching cell structure can be observed, which can be hardly observed with thick (> 70 nm) electrode. The coarse electrodes were formed for electrical measurements,

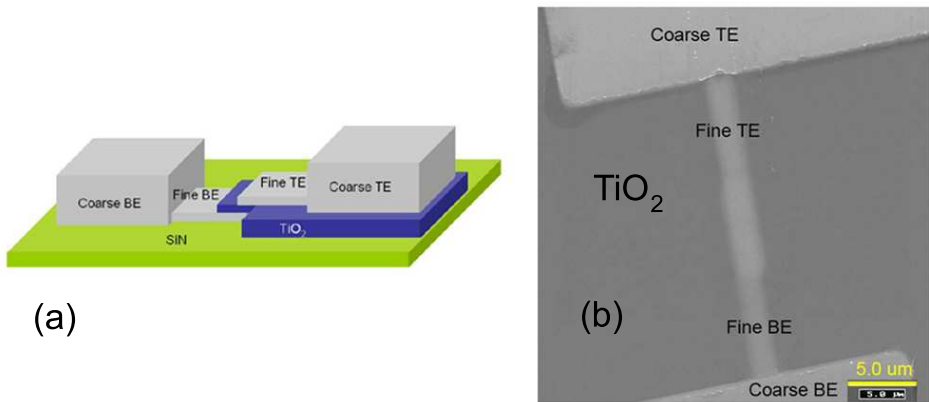


Figure 2.5: (a) Schematic of the modified stack switching cell. (b) Plane SEM image of the active area where top and bottom electrodes are overlapped.

which were thick (> 70 nm) enough not to be damaged by the mechanical stress imposed by probes (needles). First, the fine BEs were formed on a SiN_x substrate using photo lithography followed by Pt sputtering with the variation of sputtering time in order to identify the effect of electrode thickness on resistive switching behavior. Second, the coarse BEs were formed using the same method as for the fine BE formation. Third, a blanket TiO_2 film was deposited on the whole BEs and SiN_x . The whole area of TiO_2 apart from the several small squares covering the BEs partly was etched using reactive ion beam etching with a photoresist mask. Finally, the fine and coarse TEs were formed in the identical manner to that for the BE formation, giving rise to the overlap between the BE and the TE. Fig. 2.5(b) shows an SEM image of the modified stack switching cell. In the image the overlapping between the fine TE and the fine BE can be seen although the image is more or less vague. The advantages of the modified stack switching cells will be mentioned in Chapter 5.

Chapter 3

Structural and chemical properties of pristine TiO_2

In this chapter the microstructural and the chemical characteristics of pristine TiO_2 are presented. The microstructural characteristics were analyzed using X-ray diffraction, scanning electron microscope, and transmission electron microscope and the chemical characteristics using Rutherford back scattering and X-ray photoemission spectroscopy. From the analysis the crystalline structure of sputter grown TiO_2 was found to be stoichiometric TiO_2 anatase. The transmission electron microscope analysis showed that crystalline TiO_2 anatase was embedded in an amorphous phase and the grain size of the crystalline anatase was quite small (< 20 nm).

3.1 Microstructural characteristics

A 100 nm thick TiO_2 film was deposited on platinized Si and SiN_x substrates using reactive sputtering at room temperature. To identify the crystalline structure of the TiO_2 film X-ray diffraction (XRD) analysis was performed using a glancing mode with a small fixed angle of an incident X-ray. A normal θ - 2θ mode was also tried, however, no diffraction pattern could be observed. It can be guessed that the crystallinity of the film was not well evolved. Figures 3.1(a) and (b) show the XRD peaks of the TiO_2 films on the platinized substrate and the SiN_x substrate, respectively. Several peaks corresponding to TiO_2 anatase could be observed for both TiO_x films as shown in Fig. 3.1, and thus TiO_2 was found to be anatase regardless of the substrates. Anatase is generally regarded as a low temperature phase of TiO_2 . The TiO_2 film was deposited at room temperature so that TiO_2 was anatase as a matter of course.

The structure of TiO_2 anatase is depicted in Fig. 3.2. Anatase belongs to a space group of $I4_1/\text{amd}(141)$, tetragonal with the longer c lattice constant than a .[28] The lattice constants a and c are 3.7842 Å and 9.5146 Å, respectively.[29] The basic building block is a TiO_6 octahedron depicted in Fig. 3.2(b). The arrangement of TiO_6 octahedra determines the crystal structure of TiO_2 , anatase, rutile, and brookite. Indeed, all anatase, rutile, and brookite consist of TiO_6 octahedra.

It is known that titanium oxide undergo various phase transitions relying on thermodynamic variables i.e. temperature, oxygen partial pressure and so on. This

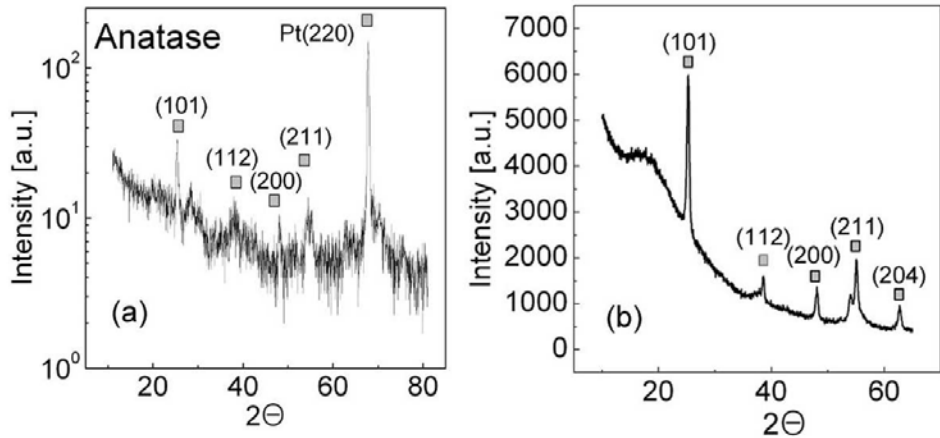


Figure 3.1: XRD peaks of the TiO₂ on (a) a platinized substrate and (b) a SiN_x substrate, measured using a glancing mode.

is attributed to transition metal Ti, which can have various valence states. The phase diagram of titanium oxides is shown in Fig. 3.3. The transition of the crystal structure and the stoichiometry of titanium oxide is accompanied with the that of the electrical properties. Indeed, TiO₂ is regarded as n-type semiconductor while TiO_{2-n/2}, where about $n > 1.5$, is regarded as metal. Even the small change in the stoichiometry of the Magnéli phase leads to the large change in the electrical properties. The Magnéli phase has a pseudo-rutile structure expressed as Ti_nO_{2n-1}, where $n \geq 4$.[31–33] In Fig. 3.3 the Magnéli phase is located between Ti₃O₅ and TiO₂.

Cross-sectional scanning electron microscope (SEM) image of a 110 nm thick TiO₂ film is shown in Fig. 3.3. It can be seen that the film consists of many thin columns termed columnar structure. The aspect ratio of the columns is quite high, implying that in the initial stage of the film growth the nucleation of seed grains is dominant rather than the lateral growth of seed grains. The lateral growth occurs by virtue of the surface diffusion of adatoms on the substrate, which is a thermally activated process. Since the working temperature of the TiO₂ deposition was room temperature, the surface diffusion of the adatoms is believed to be non-activated. Therefore, the nucleation was prior to the surface diffusion, resulting in the formation of the columns with the high aspect ratio.

For the observation of the microstructure of TiO₂ transmission electron microscope (TEM) was used. The procedure of TEM sample preparation is like following. First, a TiO₂ film was deposited on a SiN_x/SiO_x/Si/SiO_x/SiN_x substrate. Second, a photoresist mask was formed on the back side of the substrate for the ion beam etching of the SiN_x and SiO_x on the back side. The photoresist mask covered the whole surface of the back side apart from 9 squares whose side length was 770 μm . Third, the SiN_x and SiO_x in the open 9 squares were etched in turn using Ar ion beam exposing Si, and then the photoresist mask was removed in acetone remaining only SiN_x serving as a hard mask for the wet etching of the Si. Finally, the wafer with the

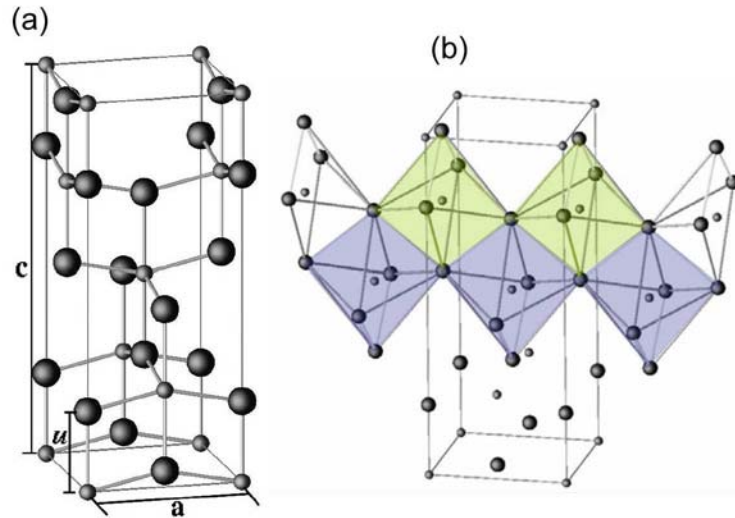


Figure 3.2: (a) TiO₂ anatase structure. (b) TiO₆ octahedron. The larger balls are O ions and the smaller balls Ti ions.[27]

SiN_x hard mask was placed in 20 % Tetramethylammonium hydroxide (TMAH) solution for 12 hours at 80 °C for the anisotropic etching of Si. The anisotropic etching is attributed to the surface energy difference between the different planes of the diamond cubic structure. Since the SiN_x layer on the front side served as an etch stop layer, the wet etching stopped at the SiN_x layer forming pyramid-shaped windows for TEM observation as can be seen in Fig. 3.4. The windows were necessary to be as small as possible (a square of about 20 to 30 μm) to minimize buckling of the sample due to residual mechanical stress being imposed on the thin membrane structure after the back etching.

Figure 3.5 shows a plane TEM image of a 30 nm thick TiO₂ film grown on the SiN_x/SiO_x/Si/SiO_x/SiN_x substrate. The figure is a bright field image so that diffracted electron beam makes dark image and transmitted electron beam makes bright image. In Fig. 3.5 it can be noticed that the locally crystallized TiO₂ grains (dark region) are embedded in the amorphous phase, implying that TiO₂ is not fully crystallized. The grain size is quite small, less than 20 nm. The small grain size as well as the poorly crystallized phase is estimated to be the reason for the difficulty in the XRD analysis using a θ -2 θ mode. The electron diffraction pattern is depicted in the inset of Fig. 3.5. The circles denote the electron beam diffracted from the underlying SiN_x layer and the bright spots around the central, transmitted beam denote the beam diffracted from many atomic planes of TiO₂.

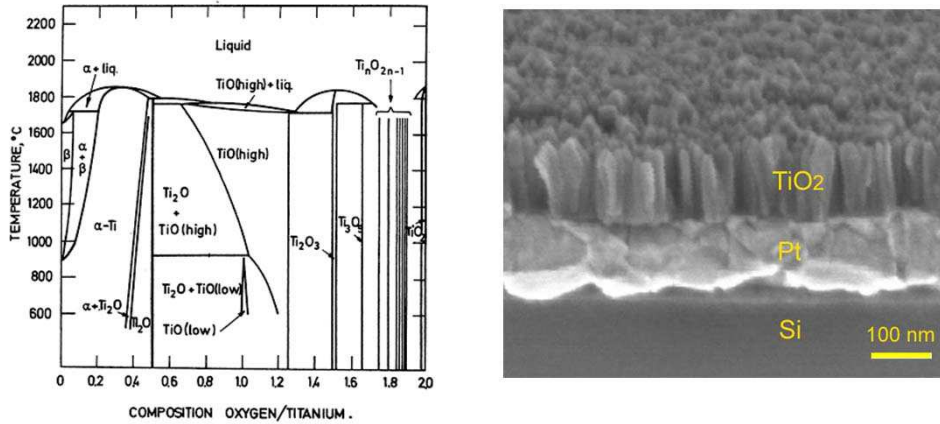


Figure 3.3: Phase diagram of titanium oxides.[30] Right: Cross-sectional SEM image of a 110 nm thick TiO_2 film

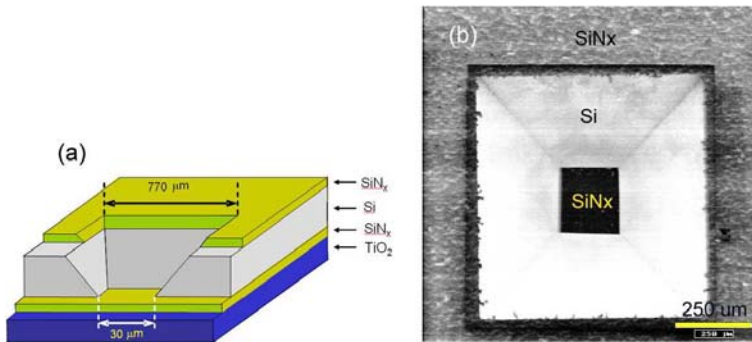


Figure 3.4: (a) Schematic of the TEM observation window. (b) SEM image of the window.

3.2 Chemical characteristics

The stoichiometry of TiO_2 were determined from Rutherford back scattering (RBS) analysis. For the RBS analysis a 27 nm thick TiO_2 film was deposited on a platinized Si substrate with an adhesion layer of ZrO_x rather than TiO_x . The ZrO_x adhesion layer was chosen to avoid the interference by the adhesion layer. The RBS and the data fitting results are shown in Fig. 3.6. The data fitting with the assumption of stoichiometric TiO_2 is well consistent with the RBS result, suggesting that the TiO_2 film is composed of stoichiometric TiO_2 .

The stoichiometry of TiO_2 was also identified using X-ray photoemission spectroscopy (XPS) analysis. The XPS measurement was performed on a 27 nm thick TiO_2 film on a platinized Si substrate with an X-ray incidence angle of 45° from the TiO_2 surface. The spectra of Ti 2p and O 1s are shown in Fig. 3.7. By fitting the obtained Ti 2p spectrum with Ti 2p spectra of different Ti valence states, Ti^{2+} ,

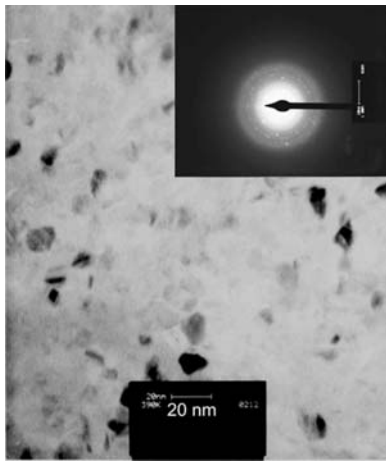


Figure 3.5: Plane TEM image of TiO₂. The inset shows the electron diffraction pattern.

Ti³⁺, and Ti⁴⁺, it was found that only a valence state of Ti⁴⁺ could be detected. This implies the contribution of the other valence states to the Ti 2p spectra is tiny so that they could not be detected. An O 1s spectrum could be divided into three different spectra as shown in Fig. 3.7(b). The peak with the highest intensity at a binding energy of 530.2 eV is from the lattice oxygen. The peak at 531.4 eV is attributed to the physisorption of (OH) on the TiO₂ surface. The lowest peak at 532.5 eV is attributed to the chemisorption of H₂O on the surface.[34]

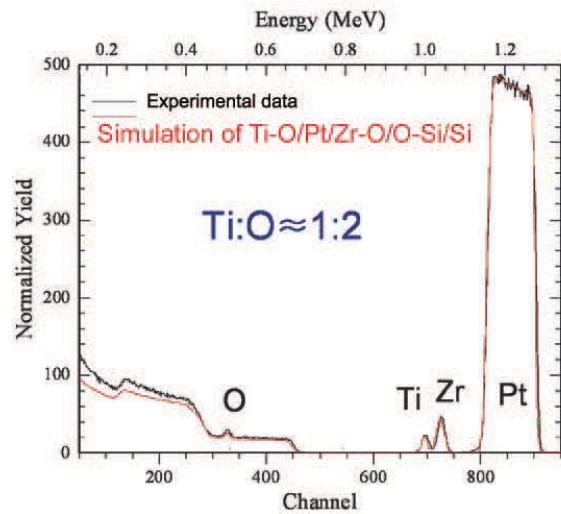


Figure 3.6: RBS spectrum and the data fitting result.

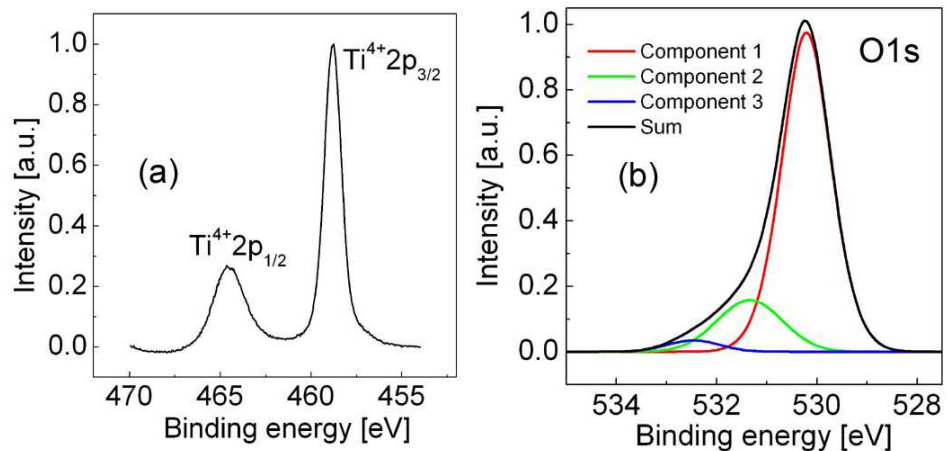


Figure 3.7: XPS spectra of (a) Ti 2p and (b) O 1s.

Chapter 4

Electrical properties of pristine TiO_2

In this chapter the electrical conduction behavior of TiO_2 films is presented in applied voltage, time, and temperature domains. TiO_2 is generally regarded as an electrolyte material, where both electronic and ionic conductances contribute to the overall electrical conduction. Current-time curves and their Fourier transformation data demonstrate the contribution of ionic conduction behavior to the total conduction. Furthermore, impedance spectroscopy was used to check dielectric relaxation as well as the contribution of ions to impedance spectra.

4.1 Current-voltage-time characteristics

Current-voltage (I - V) behavior of TiO_2 can reveal the electrical conduction mechanism. For instance, the conduction mechanism can be roughly guessed by fitting measured I - V curves with the confined conduction mechanisms: (a) electron injection such as thermionic emission and tunnel injection (b) film bulk conduction such as drift-diffusion and hopping conduction. However, it does not seem that the conduction mechanism of electrolyte TiO_2 can be easily understood using the conventional conduction equations because most of the conventional conduction equations deal with only steady state electronic leakage current rather than ionic current. In this section, the qualitative conduction description of TiO_2 will be reasoned with analyzing measured I - V curves at various temperatures and current-time (I - t) curves at various constant voltages.

4.1.1 Electrical conduction theory

By electrical conduction behavior materials can be classified into metal, semiconductor, and insulator. The conductivity of metal decreases with increasing the lattice temperature due to the decrease in the electron mobility resulting from the interaction between the free electrons and the thermally activated phonons. The number of the free electrons is barely influenced by the lattice temperature. As metal is considered to consist of lattices in an electron sea, the number of the free electrons in the sea is hardly affected by the small waves due to the change in lattice temper-

ature. In case of semiconductor, both decrease and increase in the conductivity can be observed depending on the lattice temperature. The number of the free electronic carriers, electrons and holes, increases as increasing the lattice temperature because the electrons in the valence band can move to the conduction band by virtue of thermal energy, resulting in the increase in the number of the free electrons and the holes. However, beyond a certain temperature the decrease in the electron and the hole mobilities will take place as happening in metal. The conductivity of insulator keeps on increasing as the lattice temperature increases. The electronic carriers are excited by thermal energy, implying the increase in the number of the carriers. In principle, the electronic carriers in insulator follow the Fermi-Dirac statistics, in which probability f , an electron or a hole will have energy ϵ , is given by $f(\epsilon) = [1 + e^{(\epsilon - \epsilon_F)/k_B T}]^{-1}$, where ϵ_F , k_B , and T mean the Fermi energy, the Boltzmann constant, and the absolute-temperature, respectively.

The probability, an electron or a hole following the Fermi-Dirac statistics has an energy higher than a certain energy ϵ_0 , is expressed as

$$p = \frac{\int_{\epsilon_0}^{\infty} f(\epsilon) d\epsilon}{\int_0^{\infty} f(\epsilon) d\epsilon} = \frac{\ln [1 + e^{-(\epsilon_0 - \epsilon_F)/k_B T}]}{\ln [1 + e^{\epsilon_F/k_B T}]} \quad (4.1)$$

However, the electronic carriers in insulator can be described using the Boltzmann statistics. Unless the conduction band edge (valence band edge) for the electrons (holes) is very close to the Fermi energy, the Boltzmann can replace the Fermi-Dirac statistics. For the Boltzmann statistics f can be described as $f = e^{-(\epsilon - \epsilon_F)/k_B T}$ so that the probability that an electron or a hole will have an energy higher than ϵ_0 is given by

$$p = \frac{\int_{\epsilon_0}^{\infty} e^{-(\epsilon - \epsilon_F)/k_B T} d\epsilon}{\int_0^{\infty} e^{-(\epsilon - \epsilon_F)/k_B T} d\epsilon} = e^{-(\epsilon_0 - \epsilon_F)/k_B T} \quad (4.2)$$

For the description of heavily doped insulator whose Fermi energy is close to the conduction band (valence band) for n-type (p-type) the Fermi-Dirac statistics should be applied. Later, the electric conduction behavior of heavily self-doped TiO_2 will be dealt with based on the Fermi-Dirac statistics rather than the Boltzmann statistics.

In order to describe the electric carrier transport in insulating films, one should solve the drift-diffusion equation of electric carriers based on the Crowell and Sze model with proper boundary conditions.[37] Baniecki *et al.* have reported that many different conduction equations, for instance, the thermionic emission and the modified Schottky equations and the drift-diffusion theories of Wagner and Schottky, can be derived from the Crowell and Sze model under various conditions.[38] However, most literatures have taken only electronic carriers, electrons and holes, into account so that the time-dependent drift-diffusion of ions has not been considered even for electrolyte materials.

The ionized donors and acceptors in insulator serve as space charges, and thus the space charges distribution varies with respect to time, resulting in the variation of the internal electric potential distribution. Considering the low diffusivity and the mobility of ions, it can be estimated that it takes a while for the ionic system to reach a steady state. Therefore, when the conduction behavior of electrolyte is dealt with, the conduction behavior should be taken into account in an applied voltage domain

as well as a time domain. Time-dependent conduction behavior in a one-dimensional case can be described using the one-dimensional drift-diffusion equation and Fick's second law. The drift-diffusion equation is given by

$$I_{DD}(x, t) = Aq \sum_i z_i \left(z_i c_i \mu_i E - D_i \frac{\partial c_i}{\partial x} \right) \quad (4.3)$$

where A , q , z_i , μ_i , D_i , and c_i denote the pad-size of insulator, the elementary charge, and the ionization number, the mobility, the diffusivity, and the concentration of charged particle i , respectively. And Fick's second law is given by

$$A \frac{\partial c_i}{\partial t} = - \frac{\partial I_{DD}^i}{\partial x}, \quad (4.4)$$

where I_{DD}^i denotes I_{DD} of charged particle i . The equations can be solved numerically with proper boundary conditions.

Current I at time t consists of I_{DD} as well as displacement current $A \partial D / \partial t$.

$$I(t) = I_{DD}(x, t) + A \frac{\partial D}{\partial t}, \quad (4.5)$$

where D denotes dielectric displacement. I is a constant along coordination x at a given time t . Equation 4.5 can be applied to all systems where mass transport takes place, including closed systems as well as open systems to atmosphere. D is attributed to dielectric response behavior and the change in the gravity center of space charge distribution. The details will be explained in Sec.1.2.1.

4.1.2 Current-voltage characteristics of Pt/TiO₂/Pt

For the dielectrics in which the ion-related current is negligible the electronic leakage current can be distinguished from the dielectric relaxation current using the method suggested by Dietz *et al.*[39] A sketch of the charging and the discharging currents responding to a voltage pulse is depicted in Fig. 4.1. In these dielectrics the discharging current is regarded as the dielectric relaxation current following the universal relaxation law, such as, the Curie-von Schweidler law. According to this method, the relaxation current behavior with respect to time in the time range ($t_1 < t < t_2$) is identical to that in the time range ($t > t_2$). Therefore, by subtracting the discharging current in $t > t_2$ from that in $t_1 < t < t_2$ the electronic leakage current can be evaluated.

However, in TiO₂ the discharging current in $t > t_2$ is attributed to not only the dielectric relaxation but also the redistribution of the ions (ionic relaxation) because the ion-related current in TiO₂ is not negligible. Therefore, the contribution of the dielectric relaxation to the discharging current is hard to be distinguished from the contribution of the ionic relaxation. In fact, the charging current behavior in TiO₂ is very different from the discharging current behavior so that the dielectric relaxation current could not be eliminated from the total current using the method.

I-V behavior of Pt/TiO₂/Pt stack cells was measured using a Keithley 2611 System SourceMeter by applying a stepwise voltage sweep with a voltage delay time t_d of 0.1 s. Figure 4.2 shows measured *I-V* curves of Pt/TiO₂/Pt stack cells with three

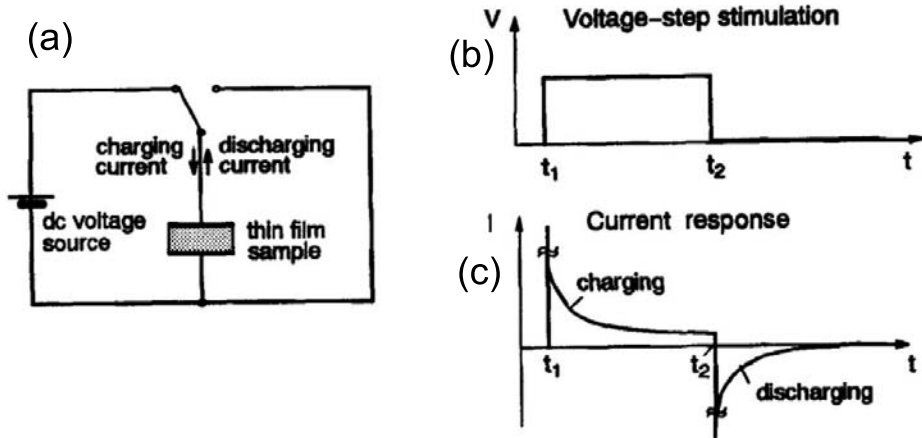


Figure 4.1: (a) Schematic of the charging and the discharging currents measurement. (b) Applied voltage pulse to the dielectric. (c) Sketch of the charging and the discharging currents responding to the voltage pulse shown in (b).[39]

different thicknesses of TiO_2 (27, 50, 75 nm) and circular-shaped top electrodes with a diameter of 100 μm . The measured current consists of three contributions: electronic current, ionic current, and the displacement current composed of dielectric relaxation and the variation of the gravity center of space charges. In Fig. 4.2 it can be noticed that the current, especially, under the positive voltage, does not remarkably depend on the thickness of TiO_2 . All I - V curves in Fig. 4.2 show hysteretic behavior. The I - V behavior near 0 V in Fig. 4.2(a) is enlarged in Fig. 4.2(b). The small letters, a , b , and c denote voltage sweep directions in the sequence $a \rightarrow b \rightarrow c$. During the downward sweep b reverse current is found to flow in the voltage range $0 < V < 0.36$ for 50 nm and $0 < V < 0.74$ for 75 nm thick TiO_2 . During the upward sweep c reverse current flows again found to follow in the voltage range $-0.3 < V < 0$ for 50 nm and $-0.58 < V < 0$ for 75 nm thick TiO_2 .

These reverse currents are unlikely to be the static leakage current because the reverse currents in a time domain show non-steady state behavior, varying with respect to time. Therefore, they can be speculated to be attributed to the ionic drift-diffusion undergoing relaxation and the displacement currents. Oxygen vacancy (V_O^-)¹ is a possibly dominant defect-type in TiO_2 as has been reported in many literatures.[40–43] By applying a voltage the oxygen vacancy distribution will be changed, that is, the concentration in the vicinity of the cathode (anode) will be increased (decreased) due to the drift of the oxygen vacancies. Jeong *et al.* has reported that the Schottky barrier height (SBH) at a metal/insulator interface is influenced by the space charge density and its distribution in the insulator, where the SBH at the interface between a metal and a n-type semiconductor decreases as increasing the positive space charge density.[35] The SBH at the anode of the Pt/ TiO_2 /Pt cell therefore decreases by virtue of the applied voltage causing the

¹ V_O^- means an oxygen vacancy in the Kröger-Vink defect notation

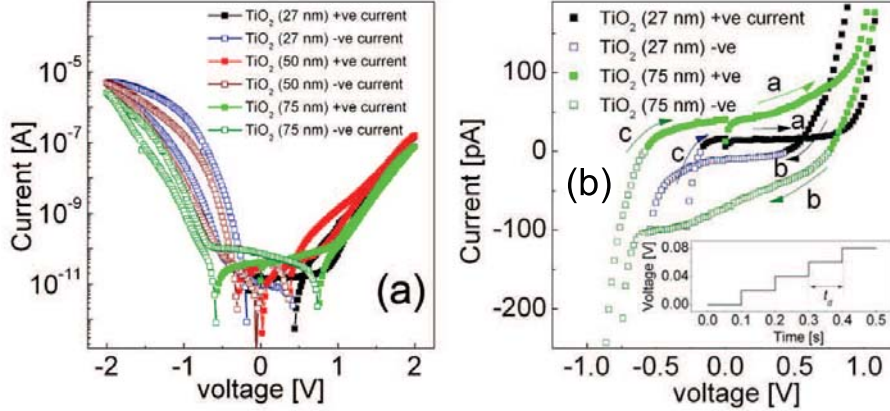


Figure 4.2: (a) I - V characteristics of Pt/TiO₂/Pt stack cells with three different thicknesses of TiO₂ (27, 50, and 75 nm). (b) enlarged I-V curves in the voltage range ($-1 < V < 1$). The inset depicts the applied stepwise voltage sweep with a voltage delay time t_d of 0.1 s.

accumulation of the oxygen vacancies at the anode. Consequently, the injection current increases.

A schematic of oxygen vacancy distribution and electron flow is depicted in Fig. 4.3. The accumulated oxygen vacancies near the cathode will undergo relaxation with decreasing the applied voltage. The relaxation time of the oxygen vacancies should be longer than the delay time t_d of the applied voltage steps, which is normally in the range $0.1\text{s} \leq t_d \leq 1\text{s}$. Therefore, the SBH at the anode during the upward sweep might be different from that during the downward sweep. The SBH after the turning points of the sweep ($\pm 2V$) is lower than that before the points, consequently, the current after the turning points is higher than that before the points. Therefore, the I - V curves show the hysteretic behavior shown in Fig. 4.2.

Effect of temperature on current-voltage curves

The electrical current in insulator is thermally activated. In case of electrolyte it is more or less difficult to analyze the conduction behavior with respect to temperature because the time-dependent drift-diffusion of the ions as well as the displacement current resulting from the drift-diffusion should be taken into consideration, which are insignificant for the electrons. The I - V curves of a Pt/TiO₂(55 nm)/Pt stack cell at various temperatures, 30, 44, 58, 72, 85, 98, 111, and 123 °C, are plotted in Fig. 4.4. The delay time of voltage steps was 0.1 s. In Fig. 4.4 it can be realized that the current is generally activated by the lattice temperature. However, the details of the thermal activation of the current are not completely understood in terms of the thermal activation of the electronic and the ionic currents. It is interesting that the reverse current (negative current) under the positive voltage vanishes with increasing the temperature, whereas the reverse current (positive current) under the negative

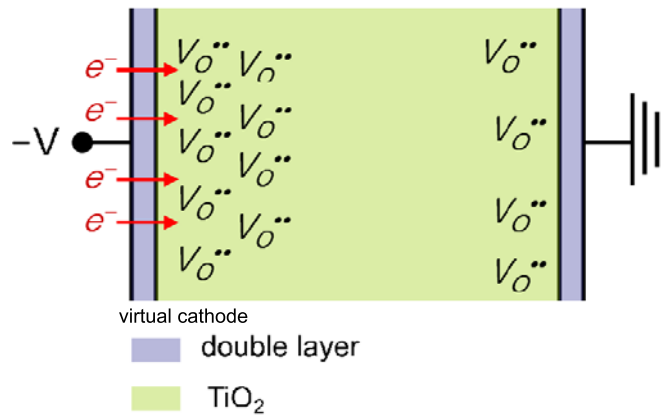


Figure 4.3: Schematic of $V_O..$ distribution and electron flow under an applied negative voltage

voltage is barely influenced by the temperature. Furthermore, it can be noticed that the current behavior during the upward sweep in the voltage regime after 4 indicated in Fig. 4.4 is barely affected by the temperature.

Effect of oxygen injection during Pt top electrode sputtering

$\text{Pt(O)}/\text{TiO}_2/\text{Pt}$ stack cells² were fabricated with injecting oxygen gas into the sputtering chamber during the Pt top electrode (TE) sputtering. The working gas consisted of 80 % Ar and 20 % O₂. The comparison between the I - V curves of $\text{Pt}/\text{TiO}_2/\text{Pt}$ and $\text{Pt(O)}/\text{TiO}_2/\text{Pt}$ can be seen in Fig. 4.5. It can be noticed that the leakage current as well as the hysteresis under the negative voltage remarkably decreases by incorporating oxygen into Pt TE while the conduction behavior under the positive voltage is hardly influenced. This oxygen injection effect is possibly attributed to the suppression of the oxygen vacancy formation in the TiO_2 surface due to the oxygen ion re-sputtering in the initial stage of the Pt sputtering. The oxygen-reduced TiO_2 surface can be re-oxidized by the injected oxygen gas preventing the oxygen vacancy formation so that the density of the oxygen vacancies in the vicinity of the TE will be much less than that in the $\text{Pt}/\text{TiO}_2/\text{Pt}$ cell. Consequently, the SBH at the TE/ TiO_2 interface of the $\text{Pt(O)}/\text{TiO}_2$ cell becomes higher compared with the $\text{Pt}/\text{TiO}_2/\text{Pt}$ cell. Therefore, the leakage current under the negative voltage is reduced in the $\text{Pt(O)}/\text{TiO}_2$ cell. The reduction of the I - V hysteresis can be also understood in terms of the lower oxygen vacancy concentration at the Pt(O)/ TiO_2 interface. The SBH reduction due to oxygen vacancies is insignificant in the $\text{Pt(O)}/\text{TiO}_2/\text{Pt}$ cell, and thus the variation of the oxygen vacancy distribution caused by the applied voltage does not remarkably influence the variation of the SBH. Therefore, the I - V hysteresis becomes less obvious.

² PtO_x is unlikely to be formed during the sputtering. The notation Pt(O) means Pt deposited with oxygen injection

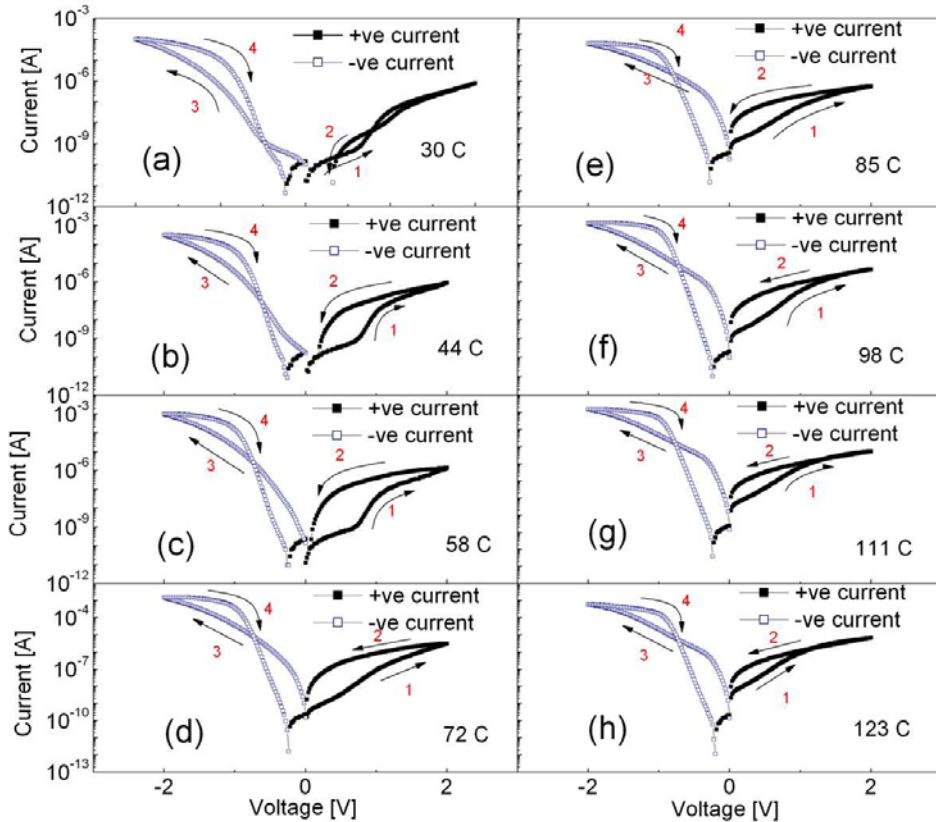


Figure 4.4: I - V curves at various measurement temperatures. The numbers, 1, 2, 3, and 4 denote the voltage sweep sequence. The closed and the open symbols denote positive current and negative current, respectively.

Current-voltage characteristics of the planar switching cells in a pristine state

The I - V curves of a planar switching cell at various temperatures are depicted in Fig. 4.6. First of all, it can be noticed that the curves hardly show hysteresis. This can be explained in terms of the re-oxidation of oxygen vacancies as mentioned in the previous section. Since the conduction area of TiO_2 between the electrodes is exposed to the air, the oxygen in the air can be easily involved in the annihilation of the oxygen vacancies so that the change in the SBH due to the variation of the oxygen vacancy concentration at the cathode is unlikely to occur.

It can be guessed that the electric conduction of the planar switching cells occurs along the surface of TiO_2 between the two electrodes. Surface conduction is expected to be different from bulk conduction due to the difference in the electronic structure of the surface from the bulk. The dangling bonds and the chemi- and the physisorptions on the surface of TiO_2 can influence the electronic structure giving rise to the distortion of the electronic structure compared to the bulk of TiO_2 . Furthermore,

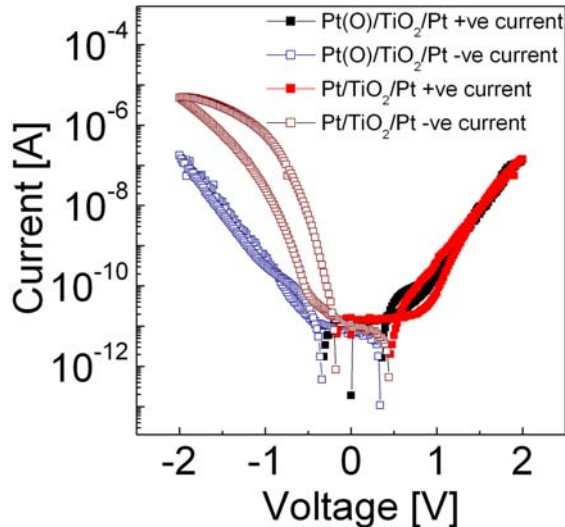


Figure 4.5: Comparison between the I - V curves of $\text{Pt}/\text{TiO}_2/\text{pt}$ and $\text{Pt(O)}/\text{TiO}_2/\text{Pt}$ stack cells.

the conduction may occur through many grain boundaries because of the columnar grains of TiO_2 , while for the stack cells the conduction occurs along the columnar grains with the much less influence of the grain boundaries, therefore, the conduction behaviors of the planar cells and the stack cells should be different.

In Fig. 4.6 the positive temperature coefficient of resistivity (PTCR)-like effect can be observed under the positive voltage and the negative voltage below about -2 V. The currents at 4 V with respect to temperature are plotted in Fig. 4.6(b). The PTCR effect in ferroelectric materials has been explained in terms of the abrupt decrease in the dielectric constant at the Curie temperature. The PTCR effect has been also observed in paraelectric $(\text{Ba},\text{Sr})\text{TiO}_3$, which has been explained in terms of the low dielectric constant layer near the electrode, so-called dead layer.[44] However, neither the ferro- to paraelectric transition nor the dead layer effect is likely to explain the PTCR-like effect in the planar TiO_2 cell. The effect may be caused by the grain boundaries between many columnar grains. However, the reason for the effect has not been clarified.

4.1.3 Current-time characteristics of $\text{Pt}/\text{TiO}_2/\text{Pt}$

Since a frequency space is the inverse of a time space, the dielectric response in a frequency domain can be obtained by Fourier transforming the current behavior in a time domain. For the dielectrics with only electronic dc conductance, dielectric response function f can be obtained by executing the Fourier transform of the measured I - t curves.[46] As given by Eq. 4.5, the drift-diffusion of charged particles and the variation of D contribute to the total current. D as a function of time is given

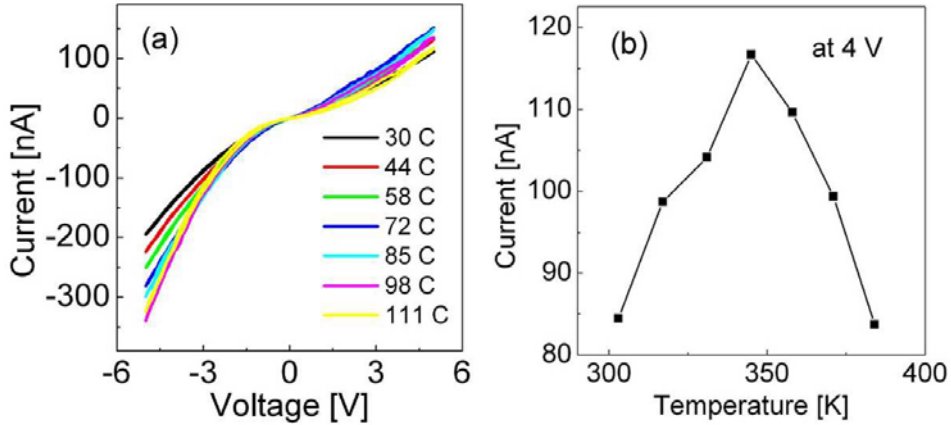


Figure 4.6: (a) I - V curves of the planar switching cell in a pristine state at various temperatures. (b) Current at 4 V with respect to temperature.

by

$$D(t) = \varepsilon_0 E_0 \left[1 + \int_0^t f(\tau) d\tau \right] + \frac{1}{d} \int_0^d x \rho(x, t) dx, \quad (4.6)$$

where ε_0 , E_0 , d , and ρ are the permittivity of vacuum, an averaged electric field, the thickness of dielectric, and a space charge concentration, respectively. The derivation of Eq. 4.6 will be given in Section 1.2. Therefore, Eq. 4.5 can be rewritten by

$$I(t) = I_{DD}(x, t) + A\varepsilon_0 E_0 [\delta(t) + f(t)] + \frac{A}{d} \int_0^d x \frac{\partial \rho(x, t)}{\partial t} dx. \quad (4.7)$$

From Eq. 4.7 f can be obtained after a simple arrangement as

$$f(t) = \frac{1}{A\varepsilon_0 E_0} [I(t) - I_{DD}(t)] - \delta(t) - \frac{1}{\varepsilon_0 E_0 d} \int_0^d x \frac{\partial \rho(x, t)}{\partial t} dx. \quad (4.8)$$

Dielectric susceptibility χ in a frequency domain can be obtained by Fourier transforming f in a time domain as shown in the following equation.

$$\chi(\omega) = \int_0^\infty f(t) e^{-i2\pi\omega t} dt. \quad (4.9)$$

Entering Eq. 4.8 into Eq. 4.9 gives the following equation that defines the relation between χ in a frequency domain and I in a time domain.

$$\begin{aligned} \chi(\omega) &= -1 - \frac{\mathcal{F}[I_{DD}(t)]}{A\varepsilon_0 E_0} + \frac{1}{A\varepsilon_0 E_0} \int_0^\infty I(t) e^{-i2\pi\omega t} dt \\ &\quad - \frac{1}{\varepsilon_0 E_0 d} \int_0^d x \left[\int_0^\infty \frac{\partial \rho(x, t)}{\partial t} e^{-i2\pi\omega t} dt \right] dx \\ &= -1 - \frac{\mathcal{F}[I_{DD}(t)]}{A\varepsilon_0 E_0} + \frac{1}{A\varepsilon_0 E_0} \int_0^\infty I(t) e^{-i2\pi\omega t} dt \\ &\quad - \frac{i2\pi\omega}{\varepsilon_0 E_0 d} \int_0^d x \left[\int_0^\infty \rho(x, t) e^{-i2\pi\omega t} dt \right] dx, \end{aligned} \quad (4.10)$$

where $\mathcal{F}[I_{DD}(t)]$ means the Fourier transform of $I_{DD}(t)$. By arranging Eq. 4.10 $\mathcal{F}[I_{DD}(t)]$ can be simply expressed as

$$\begin{aligned}\mathcal{F}[I_{DD}(t)] &= -A\varepsilon_0 E_0 [1 + \chi(\omega)] - \frac{i2\pi\omega A}{d} \int_0^d x \left[\int_0^\infty \rho(x, t) e^{-i2\pi\omega t} dt \right] dx \\ &\quad + \int_0^\infty I(t) e^{-i2\pi\omega t} dt.\end{aligned}\quad (4.11)$$

$\chi(\omega)$ can be obtained from impedance spectrum measurement. At a low dc voltage I_{DD} and time-dependent space charge redistribution are insignificant, and thus the second and the third terms on the right side of Eq. 4.7 are negligible. Therefore, complex χ ³ in a frequency domain can be measured with a low dc voltage. According to the Curie-von Schmidler relaxation law, both χ' and χ'' are given by a power-law, ω^{n-1} , with n slightly less than unity.[47, 48] The ratio of χ' to $1 + \chi''$ can be given by[47, 48]

$$\frac{\chi''(\omega)}{1 + \chi'(\omega)} \simeq \frac{\chi''(\omega)}{\chi'(\omega)} = \cot\left(\frac{n\pi}{2}\right). \quad (4.12)$$

Let us regard the sum of $\mathcal{F}[I_{DD}(t)]$ and the second term on the right side of Eq. 4.11 as $\mathcal{F}[I_{DD,D}(t)]$, where $I_{DD,D}$ means the drift-diffusion and displacement current. $\mathcal{F}[I_{DD,D}(t)]$ means the number of charges with respect to frequency, which can contribute to the total current at a given constant voltage. Therefore, it is not identical to $I_{DD,D}(\omega)$, the current measured by applying a constant dc voltage with a small ac signal. On the assumption that the amplitude of a small signal (\tilde{V}) is small enough to write $I_{DD,D}(V)$ using the Taylor expansion, $I_{DD,D}$ is given by the sum of a static current at constant voltage V_0 , $I_{DD,D}^0$, and a dynamic current with small ac voltage \tilde{V} , $\tilde{I}_{DD,D}$,

$$I_{DD,D} = I_{DD,D}^0(V_0) + \tilde{I}_{DD,D} = I_{DD,D}^0(V_0) + \frac{\partial I_{DD,D}}{\partial V} \bigg|_{V_0} \tilde{V}. \quad (4.13)$$

What can be obtained from the Fourier transform of I - t curves, $\mathcal{F}[I_{DD,D}(t)]$, is $I_{DD,D}^0$ while what can be obtained from impedance spectroscopy is $\tilde{I}_{DD,D}$, that is, $I_{DD,D}(\omega)$. Nevertheless, the dependence of $I_{DD,D}^0$ and $\tilde{I}_{DD,D}$ on frequency can be considered to be identical to each other because the small signal barely changes the frequency dependency. From the equations that have been dealt with up to now $\mathcal{F}[I_{DD,D}(t)]$ is given by

$$\mathcal{F}[I_{DD,D}(\omega)] = -A\varepsilon_0 E_0 [1 + \chi(\omega)] + \int_0^\infty I(t) e^{-i2\pi\omega t} dt. \quad (4.14)$$

The conduction behavior of a Pt/TiO₂/Pt stack cell in the time domain $0 \leq t \leq 1000$ s was measured at various constant dc voltages using a Keithley 2611 System SourceMeter. The cell consisted of 27 nm thick TiO₂. The measured I - t curves are plotted in Fig. 4.7. In Fig. 4.7 the I - V curves are found to hardly reach a steady state. These non-steady states cause the difficulty in the interpretation of low frequency impedance spectra. The abnormal impedance spectra in a low frequency

³complex χ can be described in terms of real and imaginary parts, $\chi = \chi' - i\chi''$.

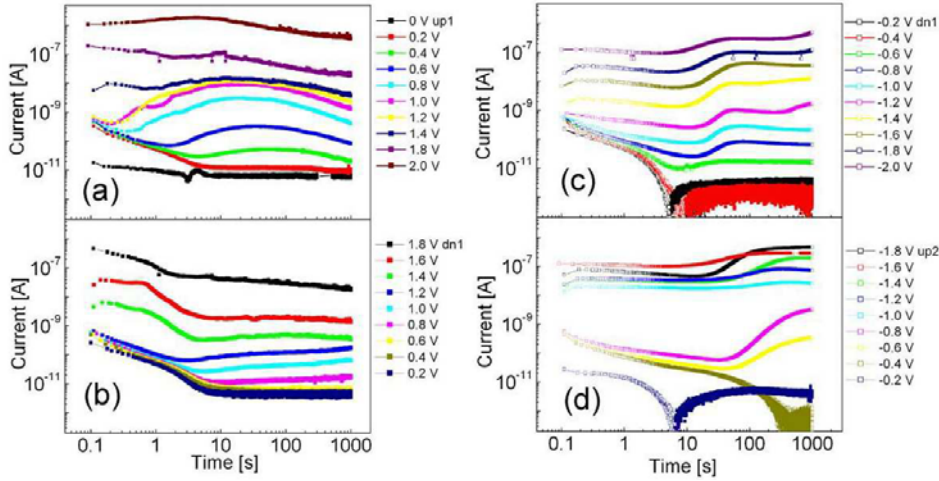


Figure 4.7: $I-t$ curves under applied constant voltages (a) from 0 to 2 V with an interval of 0.2 V (b) from 1.8 to 0.2 V (c) from 0 to -2 V and (d) from -1.8 to -0.2 V in turn. In Fig. (c) the reverse current (positive current) under -0.2 and -0.4 V is observed after about 6 s. In Fig. (d) the reverse current (positive current) is measured after about 6 s and 400 s under -0.2 and -0.4 V, respectively.

domain will be shown in Sections 1.2.2 and 1.2.3. Using Eq. 4.14, $I_{DD,D}$ can be obtained in a frequency domain. The fast Fourier transformation of I was carried out using a MATLAB.

The current as a function of frequency can be written by the following equation with taking into account the dielectric response to small ac signal \tilde{V} ,

$$I(\omega) = \mathcal{F}[I_{DD,D}(\omega)] + i2\pi\omega C\tilde{V}, \quad (4.15)$$

where C denotes complex capacitance. The Fourier transformed admittance data are plotted in the Cole-Cole plane as shown in Fig. 4.8. The curves in Fig. 4.8 show abnormal behavior in the low frequency regime, where the positive $Im(Z)$ values appear due to the frequency-dependent drift-diffusion and displacement currents. However, in the relatively high frequency regime ($1 \text{ Hz} < \omega < 10 \text{ kHz}$) the impedance spectra recover the semicircles because the ionic behavior can not respond to the frequencies. In the frequency regime ($> 10 \text{ kHz}$) the Cole-Cole plots again deviate from the semicircles because the Curie-von Schewidler relaxation becomes prominent in the frequency regime.

4.2 Impedance spectra of Pt/TiO₂/Pt

The impedance spectra of Pt/TiO₂/Pt stack cells in two different frequency domains, $60 \text{ Hz} < \omega < 1 \text{ MHz}$ and $0.1 \text{ Hz} < \omega < 100 \text{ kHz}$, are presented. The measurements in the domain ($0.1 \text{ Hz} < \omega < 100 \text{ kHz}$) were performed to identify the low frequency characteristics of the impedance, which are expected to involve the sluggish drift-

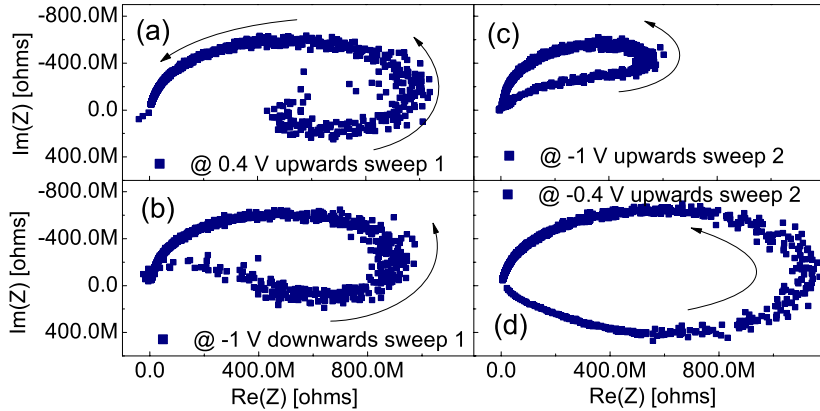


Figure 4.8: Cole-cole plots of the admittance-frequency curves obtained from the I - t curves at constant dc voltages of (a) 0.4 V in a upwards sweep, (b)-1 V in a downwards sweep, (c) -1 V, and (d) -0.4 V in a upwards sweep, respectively. The arrows indicate the direction of the increase in frequency

diffusion of the ions. And also the impedance spectra in the low frequency domain are compared with the Fourier transformation of the I - t curves shown in Fig. 4.7.

4.2.1 Dielectric behavior in time and frequency domains

D in Eq. 4.5 consists of D due to dielectric response (D_p) and the time-dependent behavior of space charge distribution (D_{sc}). Both D_p and D_{sc} are given by a function of x and t satisfying the continuity equation, $\partial D / \partial x = \rho$. On the assumption that the sum of dielectric response satisfies the rule of the superposition of the dielectric polarization P_p can be defined as a convolution integral over the time variable τ given as the following equation.[50]

$$P_p(t) = \epsilon_0 \int_0^t f(\tau) E(t - \tau) d\tau. \quad (4.16)$$

The physical meaning of the convolution integral is that P_p observed at time t is the sum of the responses to the electric fields in the past. D_{sc} is the displacement induced by time-dependent space charge distribution. Let us suppose sheet charge $-q$ placed at x between two parallel electrode plates with distance d . Using a simple one-dimensional electrostatic theory it can be calculated that the areal density of the induced charges on the left electrode $Q_{sc,L}$ and the right electrode $Q_{sc,R}$ are $q(1 - x/d)$ and qx/d , respectively. In case of arbitrarily distributed positive point charges q_i at x_i , the areal densities of the charges on the left electrode $Q_{sc,L}^+$ and the

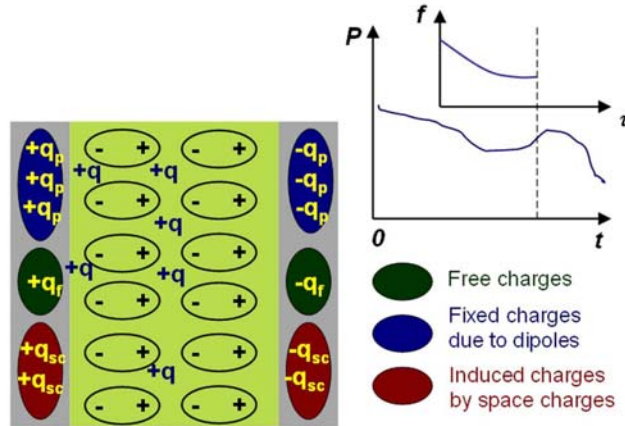


Figure 4.9: Schematic of charge distribution in dielectric.

right electrode $Q_{sc,R}^+$ are

$$Q_{sc,L}^+ = \frac{M^+}{d} = \frac{Q^+ s^+}{d} \quad (4.17)$$

and

$$Q_{sc,R}^+ = Q^+ - \frac{M^+}{d} = Q^+ - \frac{Q^+ s^+}{d}, \quad (4.18)$$

where Q^+ and M^+ denote the areal density of the positive charges between the electrodes and the first moment of the positive charge distribution, respectively. And s^+ denotes the center of the gravity of the positive charge distribution and can be given by

$$s^+ = \frac{\int_0^d x \rho^+(x) dx}{\int_0^d \rho^+(x) dx}, \quad (4.19)$$

where ρ^+ is a positive charge density. In case of negative charge distribution, the above equations are valid by changing + to -. Therefore, the areal densities of the charges induced by both positive and negative charges on the left electrode $Q_{sc,L}$ and the right electrode $Q_{sc,R}$ are

$$Q_{sc,L} = \frac{1}{d} \int_0^d x \rho(x) dx \quad (4.20)$$

and

$$Q_{sc,R} = Q - \frac{1}{d} \int_0^d x \rho(x) dx, \quad (4.21)$$

where ρ is the sum of ρ^+ and ρ^- . Q is zero to satisfy the charge neutrality condition, and thus $Q_{sc,R}$ is equal to $-Q_{sc,L}$. By applying the one-dimensional Poisson equation the electric field at $x = 0$ can be obtained in terms of the densities of the free charges ρ_f , the charges induced by the dielectric response ρ_p , and by the space charges ρ_{sc} as can be given by

$$\left. \frac{dE}{dx} \right|_{x=0} = \frac{\rho_f + \rho_p + \rho_{sc}}{\epsilon_0}. \quad (4.22)$$

And ρ_p and ρ_{sc} can be described using the divergence of the polarization vector due to the dielectric response P_p and that due to the space charges P_{sc} , respectively, giving the equations $\rho_p = -dP_p/dx|_{x=0}$ and $\rho_{sc} = -dP_{sc}/dx|_{x=0}$. Entering these equations into Eq. 4.22 gives the following equation.

$$\rho_f = \frac{dD}{dx} \Big|_{x=0} = \frac{d}{dx} (\varepsilon_0 E + P_p + P_{sc}) \Big|_{x=0}. \quad (4.23)$$

Therefore, $D(t)$ can be obtained by entering Eqs. 4.16 and 4.20 into Eq. 4.23 as given by

$$D(t) = \varepsilon_0 E + \varepsilon_0 \int_0^t f(\tau) E(t-\tau) d\tau + \frac{1}{d} \int_0^d x \rho(x) dx. \quad (4.24)$$

By executing the Fourier transform of $I(t)$ in Eq. 4.5 current behavior in a frequency domain $I(\omega)$ can be obtained. Since I is not a function of x at a given time, any x can be taken as a reference point. Let us take an origin point $x = 0$ as a reference point. Therefore, since now $D_p(t)$, $D_{sc}(t)$, and $E(t)$ are time-dependent functions at $x = 0$. By transforming $I(t)$ using the Fourier transformation $I(\omega)$ can be obtained.

$$I(\omega) = I_{DD}(\omega) + i2\pi\omega D(\omega). \quad (4.25)$$

$D(\omega)$ is obtained by the Fourier transform of Eq. 4.24 as expressed as the following equation.

$$D(\omega) = \varepsilon_0 E(\omega) + \varepsilon_0 \chi(\omega) E(\omega) + \frac{1}{d} \int_0^d x \left[\int_0^\infty \rho(x, t) e^{-i2\pi\omega t} dt \right] dx, \quad (4.26)$$

where $\chi(\omega)$ is given by Eq. 4.9. Entering Eq. 4.26 into Eq. 4.25 gives

$$I(\omega) = I_{DD}(\omega) + i2\pi\omega \varepsilon_0 E(\omega) [1 + \chi(\omega)] + \frac{i2\pi\omega}{d} \int_0^d x \left[\int_0^\infty \rho(x, t) e^{-i2\pi\omega t} dt \right] dx. \quad (4.27)$$

By dividing both sides of Eq. 4.27 by $V(\omega)$ which is a small ac signal admittance as a function of frequency is given by

$$Y(\omega) = \frac{I_{DD}(\omega)}{V(\omega)} + \frac{i2\pi\omega \varepsilon_0}{d} [1 + \chi(\omega)] + \frac{i2\pi\omega}{V(\omega) d} \int_0^d x \left[\int_0^\infty \rho(x, t) e^{-i2\pi\omega t} dt \right] dx. \quad (4.28)$$

$\chi(\omega)$ can be determined by measuring f in a time domain with applying a constant voltage. Under a constant voltage D with respect to time can be described as

$$D(t) = \varepsilon_0 E_0 \left[1 + \int_0^t f(\tau) d\tau + \frac{1}{d} \int_0^d x \rho(x, t) dx \right]. \quad (4.29)$$

Therefore, $I(t)$ is

$$I(t) = I_{DD}(x, t) + \varepsilon_0 E_0 \left[\delta(t) + f(t) + \frac{1}{d} \int_0^d x \frac{\partial \rho(x, t)}{\partial t} dx \right]. \quad (4.30)$$

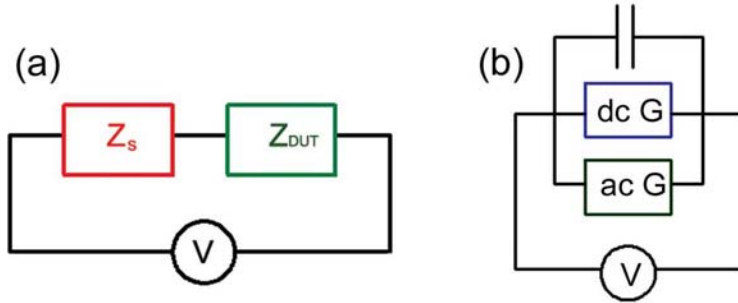


Figure 4.10: Equivalent circuit of (a) the impedance measurement configuration and (b) the dielectric in the steady state.

From Eq. 4.30 $f(t)$ can be obtained after a simple arrangement as

$$f(t) = \frac{1}{\varepsilon_0 E_0} [I(t) - I_{DD}(t)] - \delta(t) - \frac{1}{\varepsilon_0 E_0 d} \int_0^d x \frac{\partial \rho(x, t)}{\partial t} dx \quad (4.31)$$

Entering Eq. 4.31 into Eq. 4.9 gives χ in a frequency domain obtained from current measurement in a time domain as can be expressed as expressed as Eq. 4.10.

Finally, admittance as a function of the frequency of an applied small ac signal $Y(\omega)$ can be obtained by entering Eq. 4.10 into Eq. 4.28.

$$\begin{aligned} Y(\omega) = & \frac{I_{DD}(\omega)}{V(\omega)} + \frac{4\pi^2 \omega^2}{E_0 d^2} \int_0^d x \left[\int_0^\infty \rho(x, t) e^{-i2\pi\omega t} dt \right] dx \\ & - \frac{i2\pi\omega}{E_0 d} \left[I_{DD}(\omega) - \int_0^\infty I(t) e^{-i2\pi\omega t} dt \right] \\ & + \frac{i2\pi\omega}{E_0 d^2} \int_0^d x \left[\int_0^\infty \rho(x, t) e^{-i2\pi\omega t} dt \right] dx \end{aligned} \quad (4.32)$$

4.2.2 Impedance behavior in the frequency domain (60 Hz - 1 MHz)

The impedance behavior of a Pt/TiO₂(75 nm)/Pt stack cell was determined using an HP 4284A precision LCR meter in the frequency domain (60 Hz - 1 MHz). Beyond 100 kHz the parasitic components, mainly inductance, from the measurement setup and the wires became prominent in the impedance so that short circuit calibration was performed to remove the parasitic components. The parasitic components are considered to be connected to the device under test (DUT) in series as can be seen in Fig. 4.10(a). By short circuit measurement the parasitic impedance Z_s with respect to frequency could be defined. Therefore, the intrinsic impedance of the DUT (Z_{DUT}) could be evaluated by subtracting Z_s from the overall impedance including Z_{DUT} and Z_s .

Figure 4.11 shows the calibrated real and imaginary parts of the admittance [$Re(Y)$ and $Im(Y)$] in the frequency domain (60 Hz - 1 MHz) with applying various constant voltages. At zero voltage the time-dependent variation of the distribution

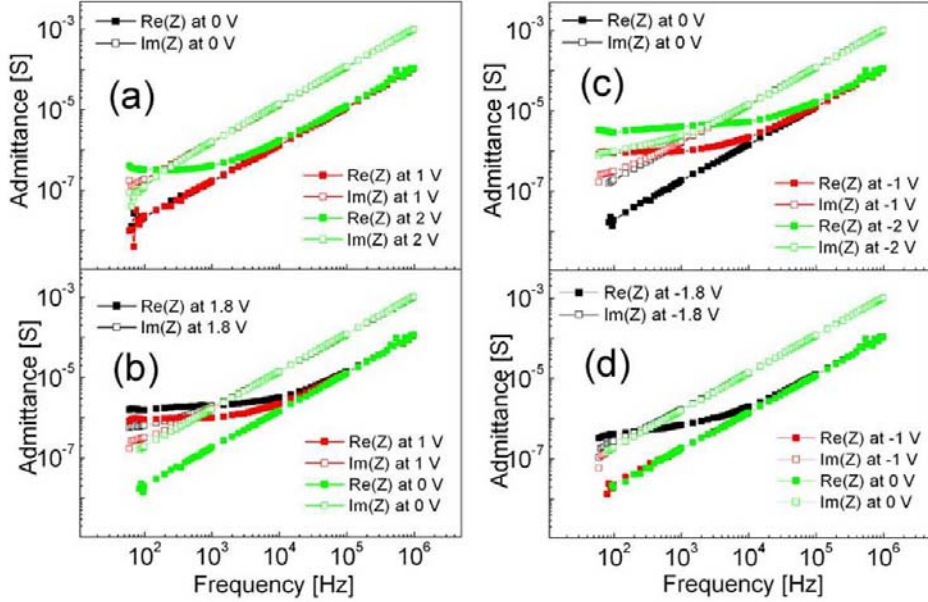


Figure 4.11: $\text{Re}(Y)$ and $\text{Im}(Y)$ in the frequency domain (60 Hz - 1 MHz) measured with varying a dc constant voltage. (a) Measurements with increasing the applied constant voltage, 0, 1, and 2 V in turn. Measurements immediately following the previous measurements (b) with decreasing the applied constant voltage, 1.8, 1, and 0 V, (c) with decreasing the constant voltage, -1 and -2 V, and (d) with increasing the constant voltage, -1.8, -1, and 0 V, in turn.

of the ions is negligible because the drift-diffusion of the ions serving as space charges are barely activated so that the last term on the right side of Eq. 4.28 can be ignored. Furthermore, by expressing χ as the complex function $\chi = \chi' - i\chi''$ Eq. 4.28 can be expressed as

$$Y(\omega) = \frac{I_{DD}(\omega)}{V(\omega)} + \frac{i2\pi\omega\epsilon_0}{d} [1 + \chi'(\omega)] + \frac{2\pi\omega\epsilon_0}{d} \chi''(\omega). \quad (4.33)$$

If I_{DD} is in-phase with $V(\omega)$, the first term of the right side of Eq. 4.33 can be regarded as ac conductance so that Eq. 4.33 stands for an equivalent circuit consisting of dc and ac conductors and a capacitor in parallel connection with one another as depicted in Fig. 4.10(b). In Fig. 4.11 it can be noticed that at zero voltage $\text{Re}(Y)$ and $\text{Im}(Y)$ satisfy the Curie-von Schweidler relaxation law, giving the ratio of χ'' to $1 + \chi'$,

$$\frac{\chi''(\omega)}{1 + \chi'(\omega)} \simeq \frac{\chi''(\omega)}{\chi'(\omega)} = \tan \delta = \cot \left(\frac{n\pi}{2} \right). \quad (4.34)$$

$\tan \delta$ and n obtained using Eq. 4.34 with respect to frequency under a constant voltage of 0 V are plotted in Fig. 4.12. From Fig. 4.12 n is determined to be between 0.93 and 0.94, showing the very weak dielectric dispersion in the given frequency domain. At zero dc voltage only the ac conductance behavior can be seen

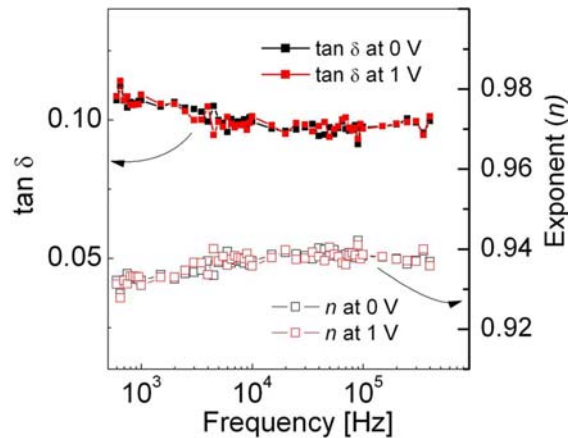


Figure 4.12: $\tan \delta$ with respect to frequency at 0 V and corresponding exponent n .

in the given frequency domain, implying the dc conductance is much lower than the ac conductance.

4.2.3 Impedance behavior in the frequency domain (0.1 Hz - 100 kHz)

The impedance spectra of a Pt/TiO₂/Pt stack cell in the frequency domain (0.1 Hz - 100 kHz) was measured using a Solartron SI 1260 Impedance/Gain-Phase Analyzer. The measured admittance spectra under various constant voltages are plotted in Fig. 4.13. The spectra in Fig. 4.13 are generally comparable to those measured in the frequency domain (60 Hz - 1 MHz) given in Fig. 4.11. The dielectric response satisfying the Curie-von Schweidler relaxation law can be observed in the frequency range above 10 kHz for all voltages. The measured admittance spectra under various constant voltages are plotted in Fig. 4.13. However, the low frequency spectra (< 10 kHz) show difference from the spectra in Fig. 4.11. The difference is believed to be caused by the non-steady state behavior of the current. As mentioned in Fig. 4.30 the current state hardly reaches a steady state so that both impedance spectra in the two different frequency domains are determined in two different non-steady states. Indeed, in the frequency range (0.1 Hz - 100 kHz) the total measurement time under a dc constant voltage was about 26 min, most time was spent on the measurement below 1 Hz, whereas in the other range (60 Hz - 1 MHz) the total measurement time was less than 1 min.

Figure 4.14 shows the Cole-Cole plots of the measured impedance spectra, which correspond to the admittance spectra shown in Fig. 4.13. In Fig. 4.14(a) the Warburg impedance spectrum is found to be dominant in the low frequency indicated by the dot line. The Warburg impedance spectrum follows the locus of the semicircle in the high frequency regime. The Warburg impedance is attributed to ionic diffusion and redox reactions. The Warburg impedance is proportional to $\omega^{-1/2}$, implying that as increasing the frequency the contribution of the ion-related impedance decreases,

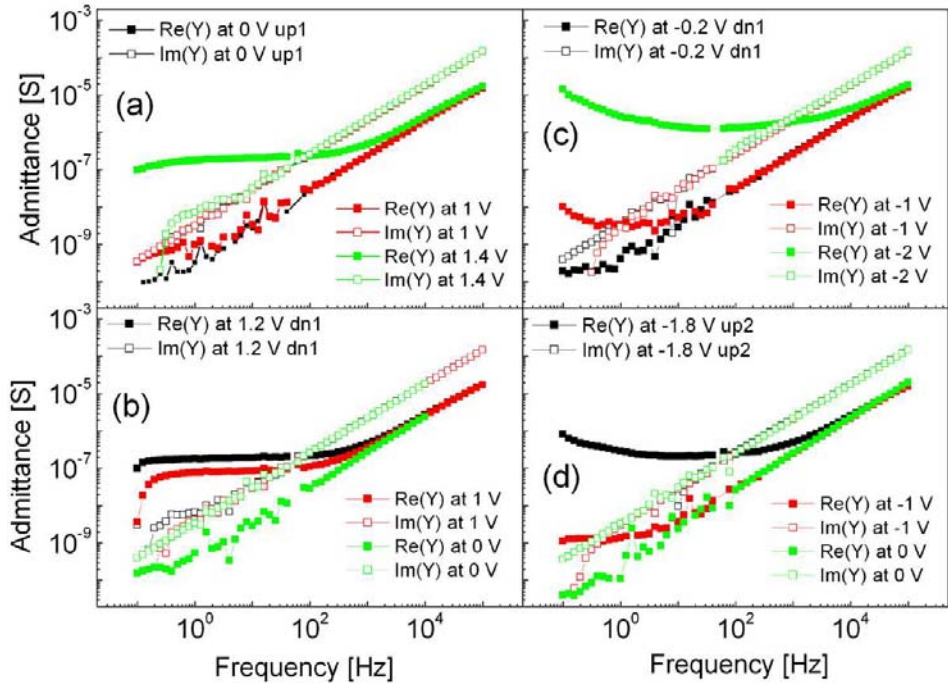


Figure 4.13: $\text{Re}(Y)$ and $\text{Im}(Y)$ in the frequency domain (0.1 Hz - 100 kHz) measured with varying a dc constant voltage; (a) increasing the voltage, 0, 1, and 1.4 V in turn (b) decreasing, 1.2, 1, 0 V, (c) -0.2, -1, and -2 V, and (d) increasing -1.8, -1, and 0 V in turn.

consequently, the contribution of the ion-related impedance to the overall impedance becomes negligible.[49] Therefore, the Cole-Cole plot in Fig. 4.14(a) recovers the semicircle with increasing frequency.

The Cole-Cole plots in Fig. 4.14 are comparable to the plots in Fig. 4.8. The deviation from the semicircles in the low frequency range shown in Figs. 4.14(b) and (c) can be found in Fig. 4.8 as well. It can be therefore concluded that the deviation is attributed to the time-dependent drift-diffusion and the displacement behaviors of the ions. There is also deviation from the semicircles in the high frequency range ($> 10^4$ Hz) although it can not be recognized in the Cole-Cole planes. The deviation is attributed to the Curie-von Schewidler law.

In summary, for TiO_2 electrolyte it took very long time to reach a steady state under the applied voltage, which might be caused by the sluggish ionic drift-diffusion. Therefore, the low frequency (< 1 Hz) impedance spectra can not be interpreted using a simple equivalent circuit model assuming a steady state. The abnormal impedance spectra in the low frequency domain could be proven to be attributed to be the ionic drift-diffusion and the displacement due to the ionic drift-diffusion by Fourier transforming the current behavior in the time domain. However, the contribution of the ionic drift-diffusion to the impedance spectra could not be distinguished from that of the displacement current on an experiment basis. Each contribution of the

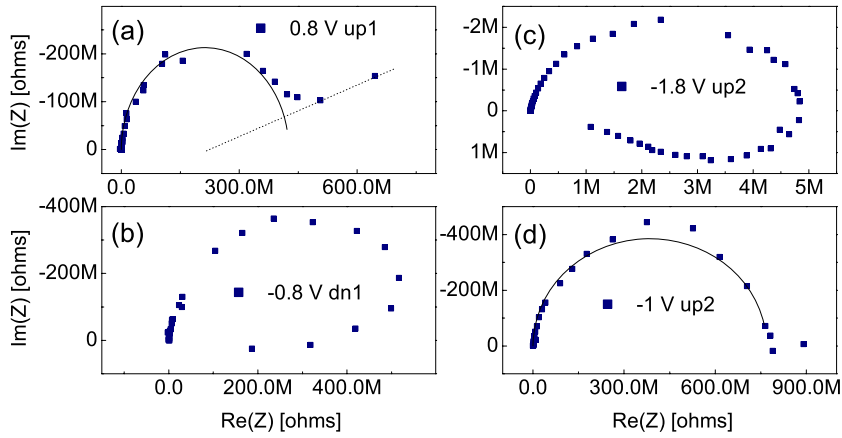


Figure 4.14: Cole-Cole plots in the frequency range (0.1 Hz - 60 Hz) at given voltages of (a) 0.8 V in a upwards sweep, (b) -0.8 V in a downwards sweep, (c) -1.8 V, and (d) -1 V in a upwards sweep, respectively.

drift-diffusion and the displacement current might be clarified by simulating the time-dependent drift-diffusion of the ions and the displacement current. In the relatively high frequency domain (> 1 Hz) the contribution of the ionic drift-diffusion could be ignored because the ions can not react to the applied ac signal. Consequently, the impedance spectra in the high frequency domain could be well interpreted using the simple equivalent circuit.

Chapter 5

Electroforming characteristics in bipolar resistive switching

Electroforming is an initial process for resistive switching measurements. During electroforming initially insulating TiO_2 undergoes a huge degradation of the resistance under an applied voltage/current. In this chapter, the effect of the electroforming in TiO_2 on the structural and chemical characteristics of switching cells and their electrical conduction behavior is introduced. Electroforming was performed by applying a voltage/current to $\text{Pt}/\text{TiO}_2/\text{Pt}$ stack cells as well as modified stack cells. The evolution of gas, most probably oxygen gas, at the anode during the electroforming could be observed in the modified stack cells. This implies the electroforming is an electrochemical reaction involving the reduction of TiO_2 introducing oxygen vacancies in TiO_2 . The modeling of the electric conduction behavior in the electroformed cells with assuming the asymmetric distribution of the oxygen vacancies was carried out. In this chapter the modeling results are presented and the consistency with the experimental results is demonstrated.

5.1 Electroforming effect on the structural and chemical properties

Electroforming in TiO_2 results in the resistance degradation of insulating TiO_2 as well as the microstructural and chemical changes in $\text{Pt}/\text{TiO}_2/\text{Pt}$ switching cells. During the voltage/current application for the electroforming the resistance of TiO_2 suddenly decreases by several orders of magnitude. Due to the sudden decrease in the resistance the power dissipation in the switching cell is to increase suddenly because the power dissipation is inversely proportional to the resistance. The power dissipation gives rise to Joule heating increasing the lattice temperature. As will be mentioned later, the Joule heating is regarded to be tremendous so that the maximum temperature in the switching cell reaches a few thousands K. At such a high temperature Pt as well as TiO_2 would undergo phase transitions. The resistance degradation of TiO_2 is therefore expected to be accompanied with changes in the microstructure and chemistry of the switching cell.

The microstructural changes of dielectrics induced by dielectric breakdown have

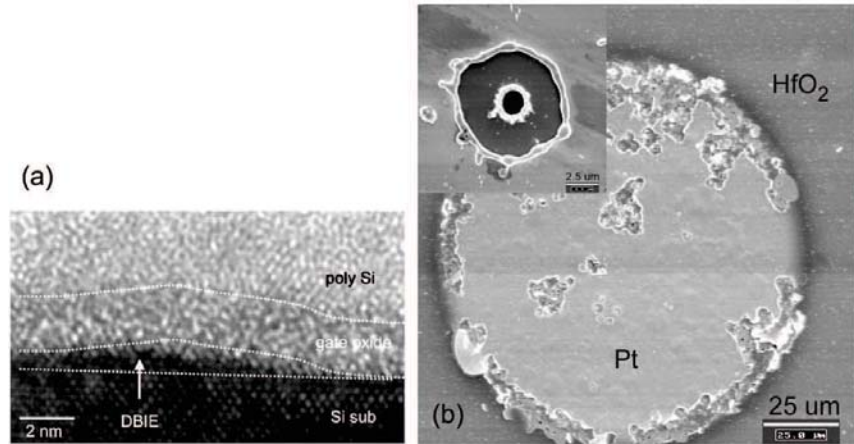


Figure 5.1: (a) Cross-sectional TEM image of poly-Si/SiO₂/Si after the DBIE.[55] (b) Plane SEM image of Pt/HfO₂/Si after dielectric breakdown. The inset shows an enlarged image of a hole in the Pt top electrode.

been frequently reported. The dielectric-breakdown-induced-epitaxy (DBIE) is one example of the resistivity degradation accompanied with microstructural changes.[55, 56] According to DBIE, the dielectric breakdown of the gate oxide in a metal-oxide-semiconductor capacitor induces the epitaxial growth of Si on the Si substrate so that it can be estimated that the Joule heating may cause the structural change. A cross-sectional transmission electron microscope (TEM) image of the DBIE is shown in Fig. 5.1(a).

A scanning electron microscope (SEM) image of a Pt/HfO₂/Si metal-oxide-semiconductor capacitor destroyed by dielectric breakdown is shown in Fig. 5.1(b). The inset of the figure is an enlarged image of a hole. An energy dispersive X-ray spectroscopy (EDX) analysis indicated no Pt signal in the outer circle and only Si signal in the inner circle meaning Pt was peeled off in the outer circle and even HfO₂ was peeled off in the inner circle. After the dielectric breakdown many holes were formed on the surface of the Pt with destroying the electrode as well as the HfO₂ layer.

A thin top electrode (TE) is helpful for the observation of the structural changes of a switching cell using, for instance, SEM and atomic force microscope. Thick electrode can well hide the changes taking place underneath the electrode so that the influence of the changes on the surface of the switching cell can be hardly observed. Therefore, modified stack switching cells with thin TE and bottom electrode (BE) such as 10 nm and 30 nm were chosen to investigate electroforming-induced structural changes using SEM. And electroforming carried out on a stack switching cell with 70 nm thick TE and 27 nm thick TiO₂ as well to check the distribution of ions over the whole volume of the cell using two-dimensional time-of-flight secondary ion mass spectroscopy (TOF-SIMS).

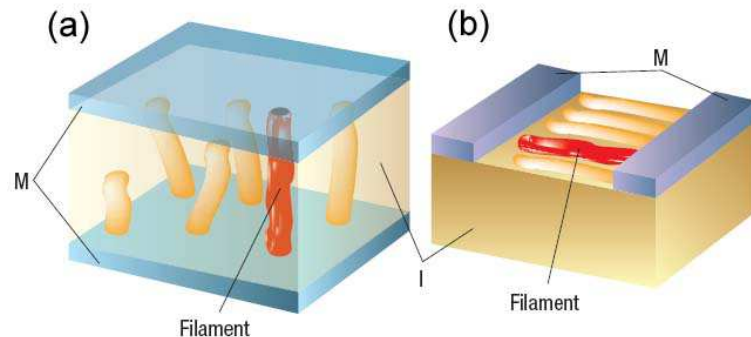


Figure 5.2: Schematics of the idealized configuration of conduction paths (filaments) in (a) a stack switching cell and (b) a planar switching cell.[20]

5.1.1 Electroforming theory

The mechanism of electroforming has been investigated for a long time, however, it has not been clarified yet. The electroforming mechanisms which have been suggested can be classified into two categories: (i) purely electronic process involving localized electronic energy states in the band gap of resistive switching materials where the localized states are attributed to inherent structural defects even before electroforming[57], intrinsic ionic defects such as interstitials and vacancies formed during electroforming,[58, 59] and the ion injection from the anode of a switching cell; (ii) electrolytic reactions at the anode of a switching cell involving the evolution of gas, for instance, fluorine gas for fluorides and oxygen gas for oxides.[60] The gas evolution introduces anion vacancies in crystal. Beyond the percolation threshold the anion vacancies can form conduction paths, through which electrons can flow by quantum mechanical tunneling or hopping.[60, 61] The models in Group (i) regard electroforming as a homogenous phenomenon uniformly occurring in the whole volume of a switching material. According to these models, the degradation of the resistance is caused by the degradation of the whole volume so that they can explain the electroforming using a one-dimensional electronic band diagram. The models in Group (ii) regard electroforming as a nonhomogeneous phenomenon occurring in localized particular volume in a switching material. The degradation of the resistance takes place in localized volume, and thus the volume contributes to the resistance of the overall resistance. Figure 5.2 depicts schematics of the configuration of conduction paths in stack and planar switching cells. Recently, conductive atomic force microscope measurements on transition metal oxide have directly shown that local conduction paths are involved in the resistive switching; their generation and rupture are the reason for the switching. In the sense that the electroforming is an initial process for the resistive switching, the electroforming can be also regarded as a localized phenomenon. Therefore, Group(ii) is proper to explain electroforming. Park *et al.* reported the electroforming and the switching behaviors of Au/ZrO₂/Zr.[63] The authors observed many molten spots on the Au TE after the electroforming, which look similar to the spot in the inset of Fig. 5.1(b). Therefore, the electroforming is considered to introduce large structural defects accompanied with the drastic change

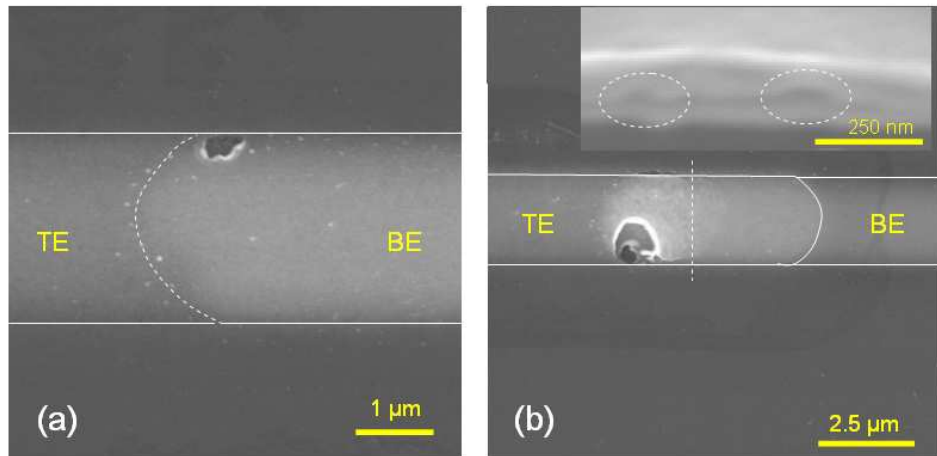


Figure 5.3: SEM images of a modified stack cell with 30 nm thick Pt TE and BE and 27 nm thick TiO_2 electroformed by applying (a) a positive voltage and (b) a negative voltage on the TE, respectively. The inset in the right figure shows the cross-sectional image along the dashed line depicted in the main figure, where the two dashed ellipses designate cavities most probably caused by the evolution of oxygen gas.

in the structure due to the Joule heating.

5.1.2 Structural changes by the electroforming

Electroforming was carried out on modified stack switching cells and a stack switching cell by applying a voltage source. The modified stack cells consisted of Pt TE and BE with the same thickness (10 or 30 nm) and 27 nm thick TiO_2 and the stack cell 70 nm (100 nm) thick TE (BE) electrode and 27 nm thick TiO_2 . An Agilent B1500A semiconductor device analyzer and a Keithley 2611 System SourceMeter were used as a voltage source.

Figures 5.3(a) and (b) show the surface SEM images of the modified stack cells with 30 nm thick electrodes, which were electroformed by applying a positive and a negative voltage on the TE, respectively. The TE is therefore the anode in Fig. 5.3(a) and the cathode in Fig. 5.3. Stepwise voltage sweep was applied with a sweep rate of 0.6 V/s and a current compliance of 50 μA for both cases. The voltage application time was about 10 s, however, the change in the resistance and the cell structure very suddenly took place at about 6 V so that the electroforming speed is difficult to evaluate. Comparing Figs. 5.3(a) and (b) notes the difference, in Fig. 5.3(a) the TE (anode) in the overlap between the TE and the BE is almost intact apart from the small area peeled off while in Fig. 5.3(b) the large area around the peeled off area is protruded. A cross-sectional SEM image of the cell shown in Fig. 5.3(b) could be obtained after cutting the cell using focused ion beam etching, which is shown in the inset of Fig. 5.3(b). The inset identifies that the protrusion was caused by the formation of cavities at the BE (anode).

The structural change induced by the electroforming can be more clearly observed

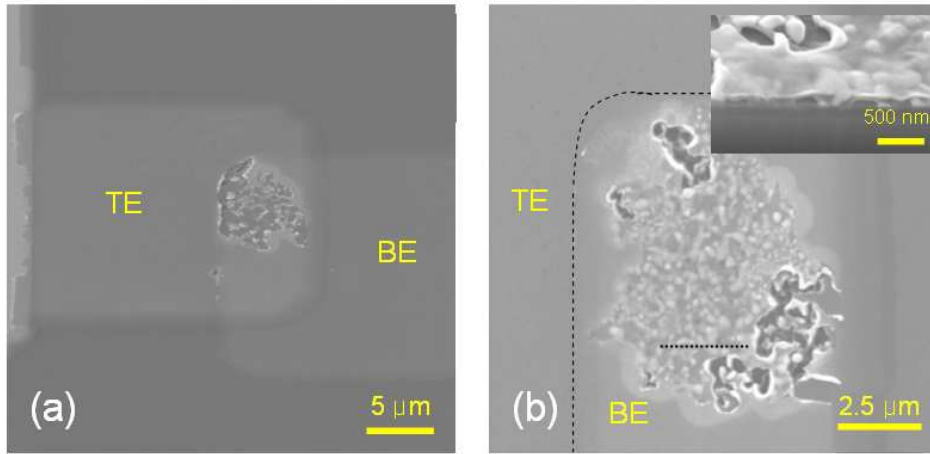


Figure 5.4: SEM images of a modified stack cell with 10 nm thick Pt TE and BE 27 nm thick TiO_2 electroformed by applying (a) a positive voltage and (b) a negative voltage on the TE, respectively. The inset in the right figure shows the cross-sectional image along the dashed line depicted in the main figure.

in the cell with a thinner (10 nm) TE and BE as can be seen in Fig. 5.4. Similar to Fig. 5.3 the change in the morphology relying on the polarity of the electroforming voltage can be observed in Fig. 5.4. However, the formation of cavities at the anode can be more obviously confirmed as shown in Fig. 5.4(b). It can be estimated that the cavities are attributed to the evolution of oxygen gas at the anode. When the BE was the anode, the oxygen gas evolved at the BE during the electroforming accumulates at the anode forming the cavities. When the TE was the anode, the gas at the TE could escape from the cell damaging the thin TE so that the TE became peeled off during the electroforming.¹ By these observations the electroforming in TiO_2 can be judged to be an electrolytic reaction forming oxygen gas with giving rise to the formation of oxygen vacancies in TiO_2 matrix. The reaction of oxygen gas formation can be expressed in the Kröger-Vink defect notation as



During the electroforming $n\text{TiO}_2$ is decomposed into free oxygen ions and oxygen vacancies and the free oxygen ions drift to the anode due to the applied electric field. The oxygen ions are accumulated at the anode, consequently, the oxygen ions form oxygen gas by donating two electrons per each oxygen ion to the conduction band. The oxygen vacancies are regarded to be fully ionized even at room temperature, having an effective charge of +2. The localized energy states introduced by the oxygen vacancies in TiO_2 have been found to be shallow, approximately 0.2 eV below the conduction band edge.[62] Therefore, the oxygen vacancies can be easily ionized by releasing electrons to the conduction band. In this sense the reaction in

¹The damage is likely to be caused by the explosion of molten TiO_2 with spouting gas like a volcano.

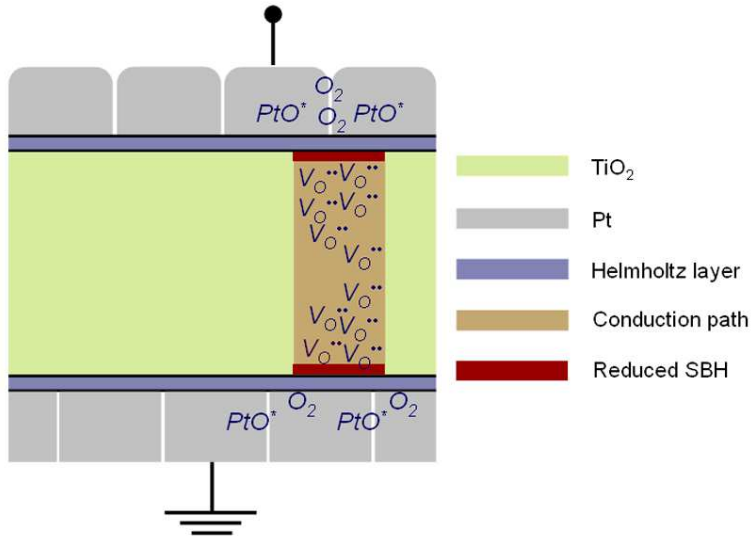


Figure 5.5: Schematic of the oxygen vacancy distribution in a Pt/TiO₂/Pt switching cell electroformed for the bipolar resistive switching.

Eq. 5.1 can be considered to be a self-doping process leading to the huge increase in the electrical conductivity. For this reaction the electrode should be inert so that the formation of oxide at the anode can be avoided.

On the other hand, the Ti ions in oxygen vacancy-enriched regions might be reduced to fulfill the local charge neutrality, according to



by capturing electrons from the cathode. Therefore, the captured electrons fill the Ti 3d band. The reduced Ti ions and the oxygen vacancies can form a metallic phase, TiO_{2-n/2}, where n is higher than 1.5, and thus the metallic phase composes a conduction path in an insulating TiO₂ matrix.

The schematic of the oxygen vacancy distribution in a Pt/TiO₂/Pt switching cell electroformed by positive voltage application is depicted in Fig. 5.5. The formation of oxygen vacancies during the electroforming is believed to be non-uniform over the switching cell, which is caused by the non-uniform electric field distribution in TiO₂ possibly due to the roughness of Pt/TiO₂ interfaces or the geometry of the TE. Consequently, the non-uniform oxygen vacancy distribution gives rise to a non-homogeneous conductivity distribution, implying the formation of local conduction paths. The detail of the Helmholtz layer and the reduced Schottky barrier height (SBH) depicted in Fig. 5.5 will be explained in Section 5.3.

Furthermore, it could be also observed that the structural changes shown in Figs. 5.3 and 5.4 initiated at the corner of the BE. A simple electrostatic calculation indicates that the highest electric field is applied at the corner of the BE. The electroforming can be therefore regarded as an electric field-driven process. Indeed, it has been reported that electroforming voltage is proportional to the thickness of a switching layer.[64]

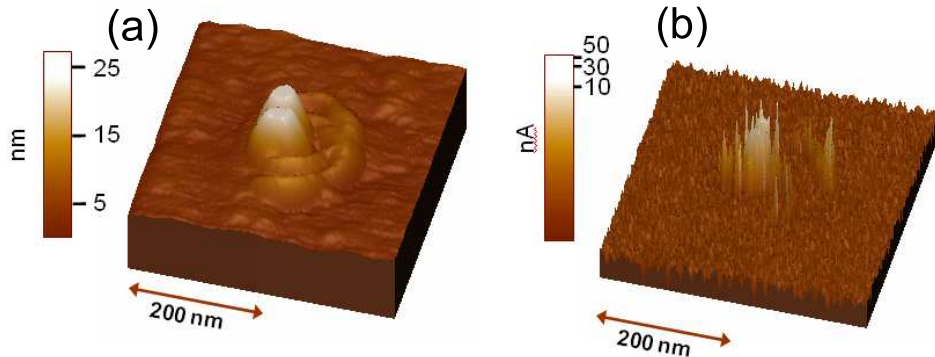


Figure 5.6: (a) Topography of TiO_2 and (b) conductivity mapping

5.1.3 Resistance degradation using conductive atomic force microscope

The resistance degradation of TiO_2 could be induced by applying a voltage on the surface of TiO_2 directly using conductive atomic force microscope (C-AFM). The sample consisted of 10 nm thick TiO_2 on 100 nm thick Pt. The tip of C-AFM was fixed at a point on the surface and two different voltages with positive and negative polarities were applied to identify the correlation between changes in the surface morphology and a voltage polarity during the resistance degradation. The applied negative voltage was found to cause huge protrusion on the surface as shown in Fig. 5.6(a). The conductivity mapping as shown in Fig. 5.6(b) identifies that the protrudent area has a much higher conductivity than the other area, implying that not only structural change but also resistance degradation occurred while the negative voltage was applied. However, applying the positive voltage could make no changes in the topography compared to the pristine surface. These observations are in a good agreement with the polarity dependence of electroforming as dealt with in the previous section. When the negative voltage was applied to the surface of TiO_2 , oxygen gas was evolved and accumulated at the BE (anode) causing the protrusion. However, when the positive voltage was applied, oxygen gas was pulled out of the TiO_2 layer so that no accumulation of oxygen gas and no consequent changes in the structure took place.

5.1.4 Chemical changes by the electroforming

During the electroforming changes in the composition of a switching cell is also expected to take place. In order to identify the changes in the composition in the depth direction two-dimensional TOF-SIMS measurements were performed on a stack switching cell with 70 nm (100 nm) thick top (bottom) electrode and 27 nm thick TiO_2 , which was electroformed by applying a positive constant voltage (5 V). For the depth profile measurements the surface of a specimen should be flat, otherwise, the profiles obtained from different areas cannot be compared with each other. As mentioned earlier, the modified stack cells with TE (10 and 30 nm) underwent the

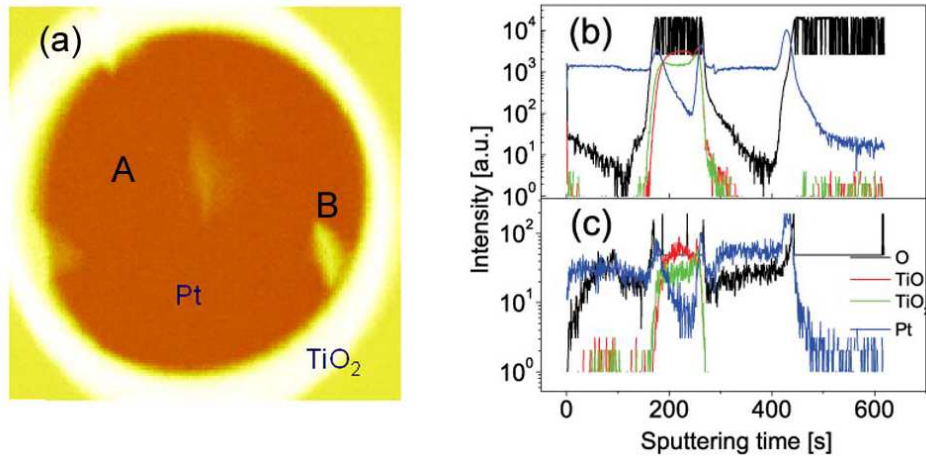


Figure 5.7: (a) Oxygen signal over the whole $100 \times 100 \mu\text{m}^2$ area, where the circle is the circular-shaped top electrode. (b) Depth profile at the point A in the dark area; (c) The depth profile at the bright point indicated by B.

serious damage so that the surface became very rough. The stack switching cell with 70 nm thick electrode hardly shows the damage on the surface of the TE. Therefore, the stack switching cell was chosen for the TOF-SIMS measurements so that it was possible to compare the depth profiles of each ion from many different points.

Figure 5.7(a) shows the integrated oxygen signal over the depth direction at all points in the $100 \times 100 \mu\text{m}^2$ scanning area including the whole TE depicted by the circle. The brightness means the intensity of the oxygen signal. The spatial resolution of the ion beam was about $1 \mu\text{m}$. In the figure the distribution of oxygen over the area of the switching cell is found to be nonhomogeneous, where a few spots with higher oxygen concentrations are present. Comparing Fig. 5.7(a) with an image of the pristine state reveals that these spots were caused by the electroforming. The depth profiles of each element at a point in the dark area and a bright spot are plotted in Figs. 5.7(b) and (c), respectively. The profile in Fig. 5.7(c) shows oxygen incorporation into both TE and BE, whereas the profile in Fig. 5.7(b) is almost identical to that of a pristine state sample. Since the TE was the anode during the electroforming, a larger amount of oxygen was incorporated into the TE than the BE, which can be identified by comparing the ratio of oxygen to platinum in the TE with that in the BE. The oxygen in the BE might be released from the ZrO_x adhesion layer underneath the BE due to the local reduction by the Joule heating during the electroforming. The incorporated oxygen most probably stays at grain boundaries of Pt by forming chemisorbed states rather than forming platinum oxide (PtO_x) phases.

The bright spots are expected to consist of a TiO_x ($x < 2$) phase instead of TiO_2 . Since the oxygen vacancies in TiO_2 serve as donors, the conductivity of TiO_x ($x < 2$) is higher than that of TiO_2 .^[65] Therefore, the bright spots in Fig. 5.7(a) are possibly conduction paths. Unfortunately, the oxygen content in TiO_x in the bright

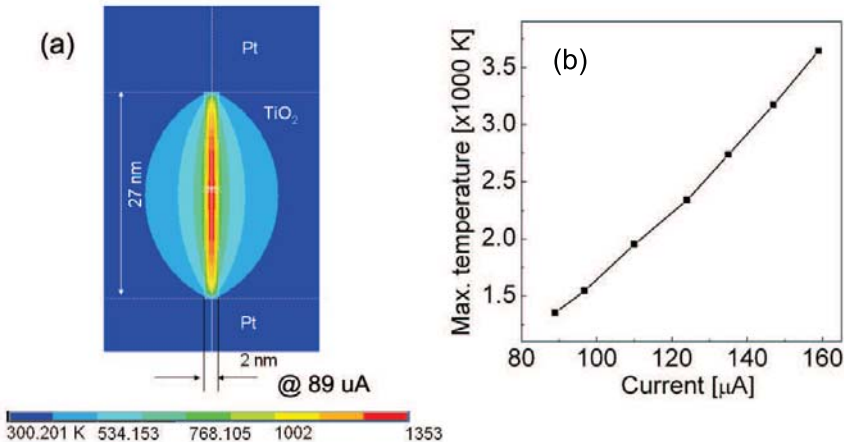


Figure 5.8: (a) Calculated temperature distributions in Pt/TiO₂/Pt containing a conduction path under a current of 89 μ A. (b) Maximum temperature with respect to the applied current.

Table 5.1: Parameters used for the calculation of the temperature distribution

materials	electric resistivity [$\Omega \cdot cm$]	Thermal conductivity [W/mK]
Pt	10 μ	71.6
TiO	300 μ	1.26
TiO ₂	3 M	6

spots could not be determined from the TOF-SIMS analysis because the oxygen signal in TiO_x was out of a measurable range.

The results of the TOF-SIMS measurements are in a good agreement with the observation of the structural changes in the modified stack cell. It can be identified that the electroforming involves the evolution of oxygen gas at the anode and the oxygen can be incorporated into Pt electrode.

5.1.5 Calculation of the Joule heating during the electro-forming

The damage on the surface of the modified stack cells does not seem to be caused by only the ejection of oxygen gas. By the shape of the broken regions it can be judged that those regions were molten during the electroforming. As a matter of fact, many re-solidified Pt droplets headed out of the broken regions could be found around the regions, implying the heat high enough to melt the local areas of the switching cell was generated during the electroforming. In order to deal with the electroforming, the Joule heating effect should be therefore taken into account.

The temperature distribution in a switching cell containing conduction paths is worth being calculated. On the assumption that the conduction paths consist of metallic TiO the calculation was carried out using finite element analysis. The

parameters used for the calculation is given in Tabel 5.1. The resistivity of TiO_2 was determined from the resistivity of pristine TiO_2 . Figures 5.8(a) and (b) show the simulated temperature distributions in a switching cell including a single TiO conduction path under an applied current of $89 \mu\text{A}$ and the maximum temperature in the conduction path with respect to the applied current, respectively. The diameter of the conduction path was assumed to be 2 nm. As shown in Fig. 5.8(b), the maximum temperature in the cell is already above 1000 K at a constant current of $89 \mu\text{A}$ and it is about 3000 K at $140 \mu\text{A}$, which is higher than the melting temperature of Pt and TiO_2 .² At this high temperature the variation of the crystal structure as well as the stoichiometry of TiO_2 is inevitable as shown in the phase diagram of TiO_x shown in Fig. 3.3. As mentioned in the previous section, the electroforming in TiO_2 is a self-doping process introducing a large amount of oxygen vacancies. Therefore, the self-doping is regarded to be accompanied with the local phase transition of TiO_2 to $\text{TiO}_x (x < 2)$.³

5.2 Electroforming effect on the electrical conduction behavior of TiO_2

The electroforming causes huge changes in the current-voltage (I - V) behavior of TiO_2 . The resistance undergoes irreversible degradation while electroforming occurs. The electroforming can be considered to be comparable to dielectric breakdown in the sense that both phenomena cause the degradation of the resistance. Dielectric breakdown can be classified into hard and soft breakdown by the possibility of the recovery from a degraded resistance state. The soft breakdown is regarded as the temporary degradation of the resistance that can be cured by thermal treatment to some extent while the hard breakdown is the permanent degradation that can not be cured. The electroforming might be therefore regarded as a sort of the soft breakdown. In this section the effect of the electroforming on the I - V characteristics of TiO_2 and the following bipolar resistive switching (BRS) behavior is investigated. The electroforming was performed using a voltage/current source.

5.2.1 Electroforming with a voltage source

Applying a voltage to a switching cell can bring about electroforming. In the air the electroforming for the BRS is completed by several electroforming steps with the alternate polarities of the electroforming voltage. Namely, at least two electroforming steps with the different voltage polarities are necessary to complete the electroforming. The compliance current is an important parameter for the voltage-controlled electroforming. Without the compliance current the sudden decrease in the resistance of TiO_2 during the electroforming causes the sudden flow of a large amount of current, resulting in a sort of hard dielectric breakdown. Therefore, the compliance current plays a crucial role in preventing the hard breakdown.

²The melting temperatures of Pt and TiO_2 at room pressure are 2041 K and 2143 K, respectively

³It can be the Magnéli phase or TiO in an extreme case

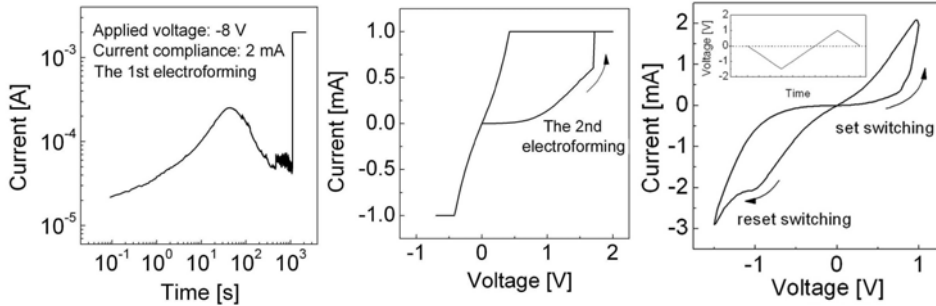


Figure 5.9: (a) Current-time curve of a Pt/ TiO_2 (100 nm)/Pt stack switching cell during the first electroforming step performed by applying a constant voltage of -8 V with a compliance current of 2 mA. (b) The second electroforming step performed by applying a voltage sweep with a compliance current of 1 mA. (c) BRS curve after the second electroforming step. The inset shows the applied voltage cycle.

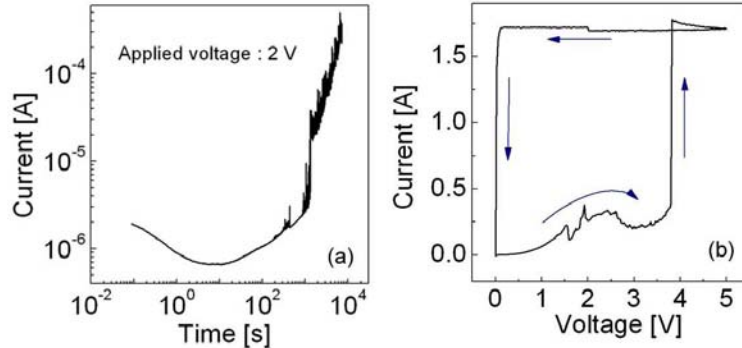


Figure 5.10: (a) The first electroforming with applying a positive constant voltage of 2 V to a Pt/ TiO_2 (75 nm)/Pt cell. (b) The second electroforming with applying a positive voltage sweep. After the second electroforming the cell was shorted.

Figure 5.9 shows the electroforming procedure in a Pt/ TiO_2 (100 nm)/Pt stack switching cell. The first sudden degradation of the resistance occurred at about 1500 s under a constant voltage of -8 V and the second degradation occurred at 1.7 V by the applied voltage sweep. Afterwards, the stable BRS shown in Fig. 5.9(c) could be measured. This alternate voltage application is essential to the electroforming for the BRS activation. The application of successive voltages of the same polarity caused the hard dielectric breakdown or the transition to the low resistance state of the unipolar resistive switching (URS) as shown in Fig. 5.10.

The gradual increase in the compliance current for successive electroforming steps is helpful to the activation of stable BRS. In case that the second electroforming is performed with a compliance current much higher than that for the first electroforming, the electroforming often gives rise to the transition to the low resistance state of URS. The completion of the electroforming could be confirmed by the observation of negative differential resistance (NDR). Before the completion of electroforming only

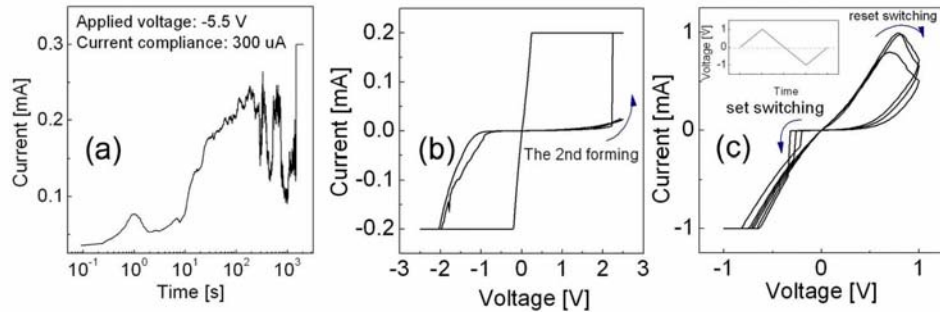


Figure 5.11: (a) Current-time curve of Pt/TiO₂(55 nm)/Pt during the first electroforming by applying a constant voltage of -5.5 V with a compliance current of 300 μ A. (b) The second electroforming by applying a voltage sweep with a compliance current of 200 μ A. (c) The BRS curves after the second electroforming. The inset shows the applied voltage with respect to time.

the decrease in the resistance occurred under alternating voltages as shown in Fig. 5.9. Finally, NDR took place during the voltage sweep after the last electroforming step so that the electroforming could be judged to be completed. It could be found that the number of electroforming steps decreases with increasing compliance current during the electroforming steps. However, at least two electroforming steps with the alternate polarities were necessary for the BRS activation regardless of the compliance current.

The polarity of set switching [high resistance state (HRS) \rightarrow low resistance state (LRS)] voltage and reset switching [LRS \rightarrow HRS] voltage was determined by the first voltage cycle following the last electroforming step. As shown in Figs. 5.9 and 5.11, for both cases the last electroforming occurred under the positive voltage, however, the BRS behaviors shown in Figs. 5.9(c) and 5.11(c) are different. The difference in the BRS behavior is due to the difference in the applied voltage cycle. The BRS in Fig. 5.9(c) was measured by applying a voltage cycle starting with a downwards sweep as plotted in the inset of Fig. 5.9(c) whereas the BRS in Fig. 5.11(c) by applying a voltage cycle starting with an upwards sweep. In spite of the different voltage cycles, the NDR could be observed for both cases. This might be attributed to the activation of an electrochemical reaction involved in the NDR at both TE/TiO₂ and TiO₂/BE interfaces.

According to Eq. 5.1, oxygen vacancies are created in the vicinity of the anode during the electroforming, inducing the decrease in the resistance of TiO₂. Since the voltages with the different polarities were applied to the cells for the electroforming, both interfaces are expected to have undergone the gas evolution introducing oxygen vacancies at the interfaces. The annihilation of oxygen vacancies is estimated to take place at the cathode by pushing the oxygen ions incorporated in the cathode into oxygen vacancy-enriched TiO_x. Consequently, the annihilation induces the increase in the resistance of TiO_x. It can be therefore estimated that for the case shown in Fig. 5.9(c) the oxygen vacancy annihilation at the TE/TiO₂ interface was brought about by the first downwards sweep, suggesting that the upper interface was responsible

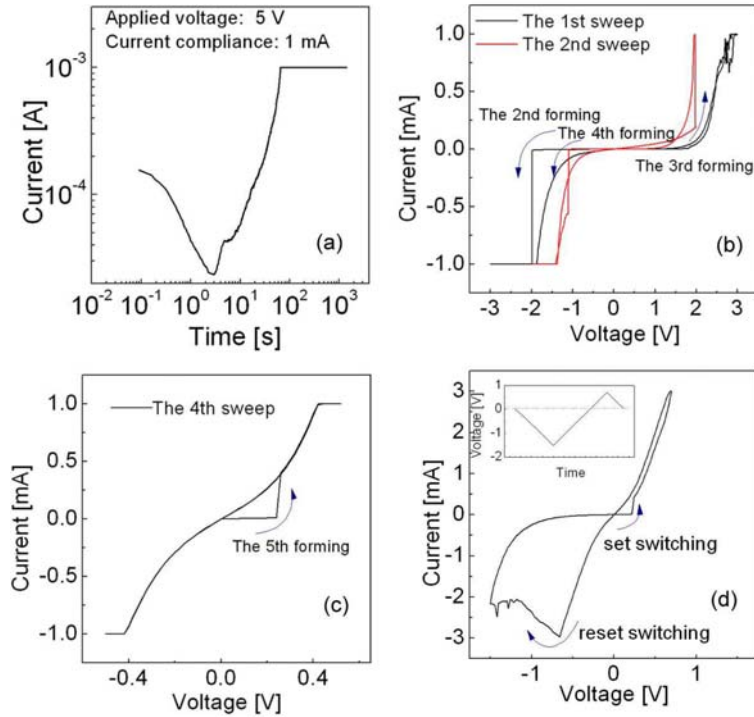


Figure 5.12: (a) Electroforming sequence of $\text{Pt}/\text{TiO}_2(55 \text{ nm})/\text{pt}$. The first electro-forming occurs under a constant positive voltage of 5 V with a compliance current of 1 mA. (b) The seconde to the forth electroformings occur under the voltage sweeps. (c) The fifth electroforming occurs. (d) the BRS curve after the fifth electroforming.

for the BRS while for the case shown in Fig. 5.11(c) the oxygen vacancy annihilation at the TiO_2/BE interface was brought about by the first upwards sweep so that the bottom interface was responsible for the BRS.

Dependence of the electroforming on the polarity of the applied voltage

The first electroforming could also occur under a positive constant voltage. Figure 5.12 shows the first electroforming of $\text{Pt}/\text{TiO}_2(55 \text{ nm})/\text{Pt}$ under a positive constant voltage and the following additional electroforming steps performed by applying voltage sweeps. The electroforming procedure was similar to those shown in Figs. 5.9 and 5.11: the alternate voltage applications with the different polarities were necessary. The gradual degradation of the resistance was observed during the first electroforming as shown in Fig. 5.12(a), compared with the negative voltage application shown in Figs. 5.9 and 5.11. This gradual degradation instead of the abrupt degradation was possibly attributed to the growth of the conduction paths, retarded by the chemical oxidation at the TE/TiO_x interface by virtue of the external oxygen. $\text{Pt}/\text{TiO}_2/\text{Pt}$ can be considered to be an open system where oxygen can be exchanged between the cell and the air through the Pt TE. In fact, it turns out that the atmosphere has

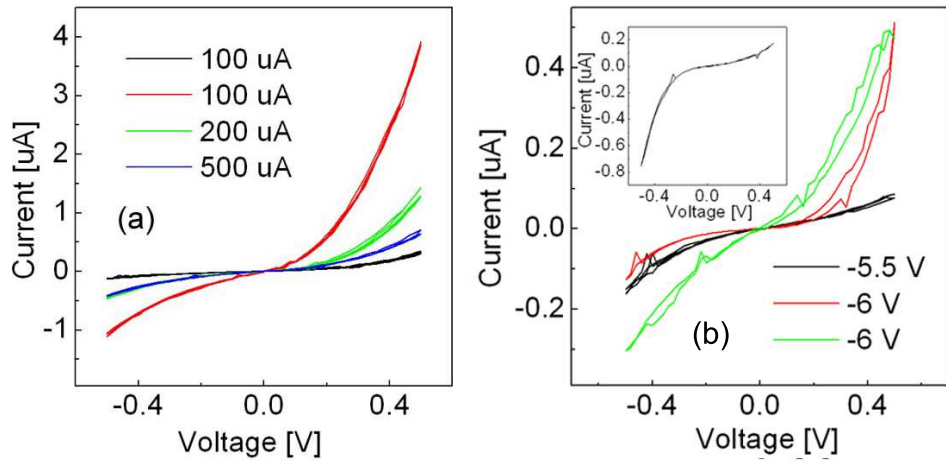


Figure 5.13: (a) I-V curves of Pt/TiO₂(55 nm)/Pt after the first electroforming with different compliance currents (100, 200, and 500 μ A) under a constant voltage of -5 V; (b) I-V curves after the electroforming under two different voltages (-5.5 and -6 V) with a compliance current of 300 μ A. The inset depicts the I-V curve after the electroforming shown in Fig. 5.12(a)

influence on electroforming behavior as will be mentioned later. During the positive voltage application to the TE the reaction in Eq. 5.1 took place pulling oxygen in TiO₂ out of the cell. At the same time the reduced TiO₂ could undergo re-oxidation by virtue of the oxygen gas in the air so that the gradual degradation could occur instead of abrupt degradation. On the other hand, in case of the first electroforming by applying a negative voltage to the TE, the re-oxidation at the TiO₂/BE can be ruled out because the lower interface is barely likely to be influenced by the air. Therefore, the abrupt decrease in the resistance could occur.

Dependence of electroforming on voltage and compliance current

I-V characteristics after the first electroforming were influenced by electroforming parameters such as voltage and compliance current. The first electroforming was performed on Pt/TiO₂(55 nm)/Pt stack switching cells with different compliance currents (100, 200, and 500 μ A) under a constant voltage of -5 V or with different constant voltages (-5 and -6 V) under a fixed compliance current of 300 μ A. After the first electroforming, the I-V behavior of each cell was determined by applying a voltage sweep. Figures 5.13(a) and (b) show the measured I-V curves from the cells electroformed with different compliance currents (100, 200, and 500 μ A) under a fixed voltage of -5 V and with different constant voltages (-5 and -6 V) under a fixed compliance current of 300 μ A, respectively. The dependence of the I-V behavior in the electroformed state on electroforming parameters showed large data scattering. Even for the cells electroformed with the same parameters the I-V curves were quite different from each other, for instance, the black and the red curves in Fig. 5.13(a) and the red and the green curves in Fig. 5.13(b). The I-V curve in the inset of Fig.

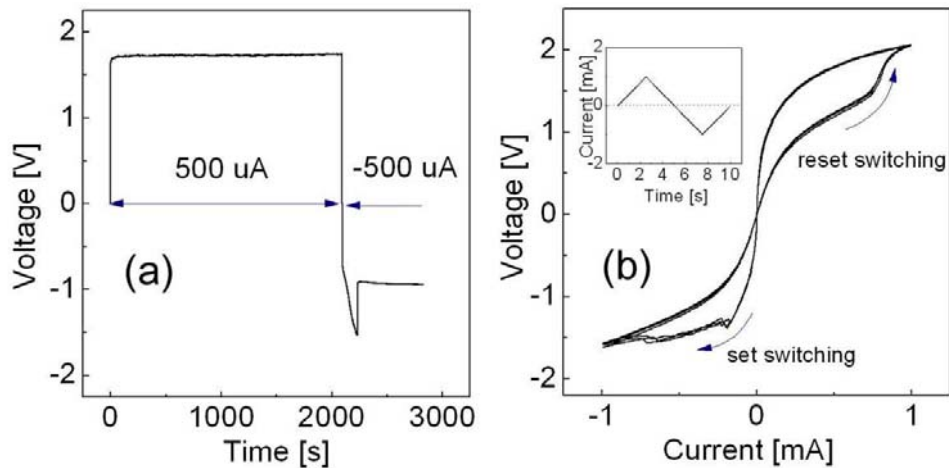


Figure 5.14: (a) Electroforming in $\text{Pt}/\text{TiO}_2(55 \text{ nm})/\text{Pt}$, performed in the air by applying two successive constant currents, $500 \mu\text{A}$ in the time domain ($0 - 2090 \text{ s}$) and $-500 \mu\text{A}$ in the time domain ($2097 - 2828 \text{ s}$). (b) BRS curves measured by applying the current sweep shown in the inset

5.13(b) was measured from the cell whose first electroforming behavior was shown in Fig. 5.12(a). Nevertheless, a rough tendency could be noticed. Comparing the I - V curves in Fig. 5.13 with that in the inset of Fig. 5.13(b) notes that the current under the same polarity as that of the electroforming voltage is lower than the current under the other polarity. During the electroforming oxygen vacancies were introduced in TiO_2 according to Eq. 5.1. Especially, they were expected to be concentrated at the anode, giving rise to the SBH reduction at the anode. Therefore, in case of the positive electroforming voltage application to the TE, the SBH at the TE/TiO_2 interface became lowered so that more electrons could flow over the lowered SBH under the negative voltage applied to the TE compared with case of the positive voltage application to the TE. Vice versa in case of the negative electroforming voltage application.

5.2.2 Electroforming with a current source

Electroforming occurred under a voltage source as well as a current source. The advantage of current-controlled electroforming is that setting compliance current is unnecessary. In case of voltage-controlled electroforming, compliance current is crucial to avoid permanent dielectric breakdown as mentioned earlier. As soon as the current reaches the compliance current during the electroforming, the voltage in a switching cell becomes out of control so that the electroforming leaves uncertainty. However, in case of the current-controlled electroforming, the voltage-current (V - I) behavior in the cell can be well evaluated during the electroforming without the uncertainty caused by the compliance current.

Figure 5.14 shows the electroforming and BRS behaviors of $\text{Pt}/\text{TiO}_2(55 \text{ nm})/\text{Pt}$

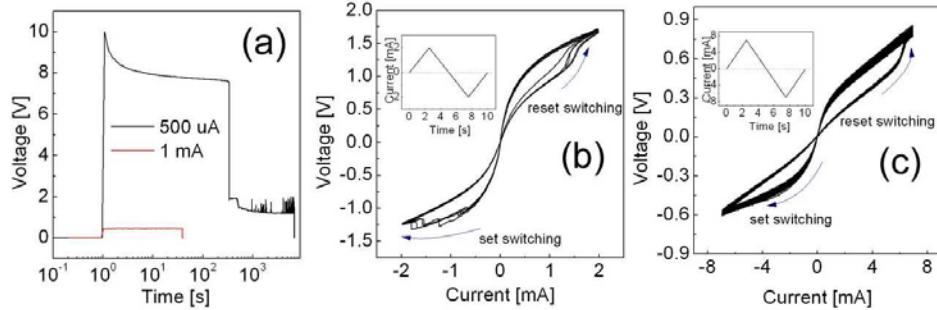


Figure 5.15: (a) Electroforming of Pt/TiO₂(55 nm)/Pt in vacuum with applying the constant currents, 500 μ A and 1 mA. (b) BRS curves of the cell electroformed by a current of 500 μ A with applying the current sweep shown in the inset. (c) BRS curves of the cell electroformed by a current of 1 mA with applying the current sweep shown in the inset.

measured using a current source in the air. The electroforming was carried out by applying two succeeding constant currents, 500 μ A in 0 – 2090 s and -500 μ A in 2097 – 2828 s. Since at least two electroforming steps with alternate polarities were needed for the voltage-controlled electroforming, the same method was applied for the current-controlled electroforming. The first electroforming took place very fast in the beginning of the current application so that its voltage-time (V - t) locus could not be observed. Therefore, the voltage during the first constant current application seems to be a constant in Fig. 5.14(a). The V - t locus of the second electroforming could be obviously observed. The sudden decrease in the voltage at 2230 s shown in Fig. 5.14(a) denotes the abrupt decrease in the resistance, implying the second electroforming occurred. After the two electroforming steps the BRS curves shown in Fig. 5.14(b) could be measured with the current sweep shown in the inset of Fig. 5.14(b). It can be noticed that no more than two electroforming steps were necessary for the current-controlled electroforming. Therefore, many electroforming steps which were often necessary for the voltage-controlled electroforming could be avoided by using the current-controlled electroforming.

Electroforming in vacuum

The gas environment surrounding a switching cell can have influence on the electroforming behavior because oxygen gas is considered to be involved in the electroforming and the oxygen gas in the air might react with TiO₂. In order to identify the effect of the air on electroforming, current-controlled electroforming was performed in a vacuum chamber whose pressure was about 3×10^{-5} Pa. Figure 5.15(a) shows V - t profiles of Pt/TiO₂(55 nm)/Pt undergoing the electroforming carried out by applying two different positive constant currents (500 μ A and 1 mA). The following BRS curves are plotted in Figs. 5.15(b) and (c). The current application for the electroforming started at 1 s. The BRS behavior in Fig. 5.15(b) is quite similar to that measured in the air shown in Fig. 5.14(b). It is interesting that the stable BRS state could be achieved without the second electroforming step. This is quite differ-

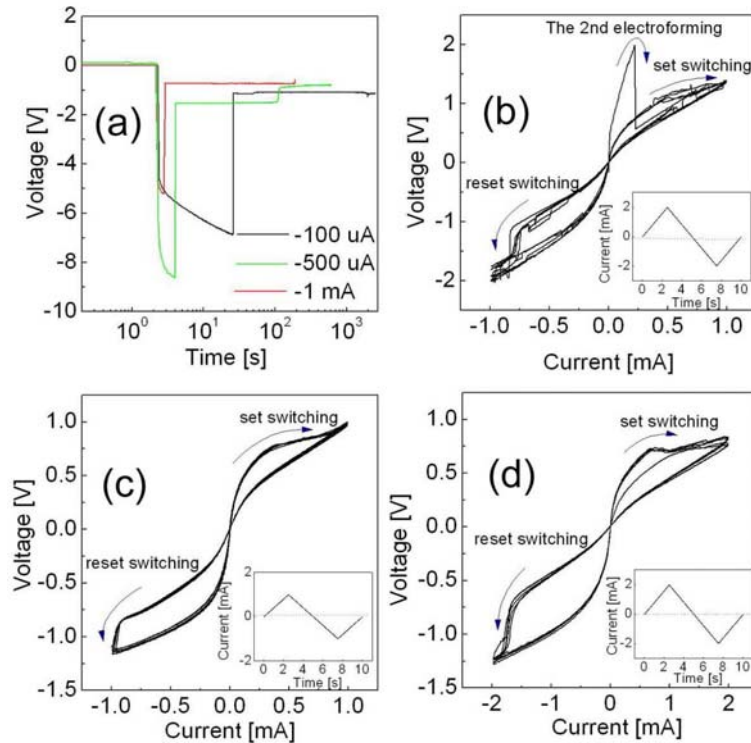


Figure 5.16: (a) Electroforming of $\text{Pt}/\text{TiO}_2(55 \text{ nm})/\text{Pt}$ in the vacuum by applying three different constant currents $-100 \mu\text{A}$, $-500 \mu\text{A}$, and -1 mA . The current application started at 2 s. (b) BRS curves of the cell electroformed with $-100 \mu\text{A}$, (c) $-500 \mu\text{A}$, and (d) -1 mA .

ent from what was observed in the electroforming in the air. The small decrease in the voltage at 490 s under a constant current of $500 \mu\text{A}$ was observed after the first abrupt decrease in the voltage at 342 s, and then the BRS could be measured without additional electroforming steps. Under a constant current of 1 mA the resistance degradation occurred very quickly in the beginning of the current application given by a unit step function with respect to time so that a current-time locus showing the degradation could not be detected. After the very quick degradation by the higher current (1 mA) the resistance became much lower than that of the cell electroformed by the lower current ($500 \mu\text{A}$) shown in Fig. 5.15(b), and thus the BRS with a lower resistance for both HRS and LRS was measured as shown in Fig. 5.15(c).

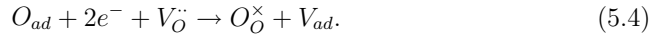
The BRS could be also activated by a single electroforming step with a negative current in vacuum, relying on the amount of the applied current. $\text{Pt}/\text{TiO}_2(55 \text{ nm})/\text{Pt}$ cells were electroformed in vacuum by applying three different constant currents ($-100 \mu\text{A}$, $-500 \mu\text{A}$, and -1 mA). The electroforming behaviors and the following BRS curves of the cells are shown in Fig. 5.16. Under a current of $-100 \mu\text{A}$ the resistance underwent one time abrupt decrease at 26 s as shown in Fig. 5.16(a). Afterwards, no additional decreases in the resistance occurred under the given current. However,

the second electroforming occurred during the upwards current sweep, finally, the BRS could be measured as shown in Fig. 5.16(b). The resistance under a current of $-500 \mu\text{A}$ underwent two times abrupt decreases, the first decrease at 4 s and the second one at 110 s. Afterwards, no additional electroforming steps were necessary for the activation of the BRS as shown in Fig. 5.16(c). This electroforming behavior is comparable to the electroforming under a current of $500 \mu\text{A}$ shown in Fig. 5.15(a). The resistance under a current of -1 mA underwent one time abrupt decrease in the resistance in the beginning of the current application at 2.8 s. However, the resistance after the single decrease was comparable to that after the two times decrease under a current of $-500 \mu\text{A}$ and no additional degradations (electroforming) were not necessary for the BRS observation as shown in Fig. 5.16(d). This is comparable to the case of the electroforming under a current of 1 mA shown in Fig. 5.15(a).

For the description of the electroforming in the air the chemical reaction of oxygen gas molecules in the air with oxygen vacancies at the TE/TiO₂ interface should be taken into account. Pt is catalyst for the decomposition of gas molecules.[69] Especially, Pt can decompose oxygen gas molecules into oxygen atoms by forming chemisorption of oxygen atoms on the surface.[69] Oxygen gas molecules can form the chemisorption states by the following reaction.



where V_{ad} and O_{ad} denote a vacant adatom site and an oxygen adatom, respectively. Then the oxygen adatoms can react with oxygen vacancies according to the following reaction.



The mechanism of the influence of the atmosphere on the electroforming can be speculated based on the chemical reactions Eqs. 5.3 and 5.4 for four different conditions of the electroforming: applying (i) a positive voltage/current and (ii) a negative voltage/current to the TE in the air and (iii) a positive voltage/current and (iv) a negative voltage/current to the TE in vacuum.

(i) Under the positive voltage/current application to the TE in the air oxygen vacancies are formed at the TE/TiO₂ interface according to the electrochemical reaction shown in Eq. 5.1, leading to the reduction of the SBH at the TE/TiO₂ interface. They drift and diffuse to the BE due to the applied electric field and the gradient of the oxygen vacancy concentration. The drift and diffusion of the oxygen vacancies result in their accumulation in the vicinity of the TiO₂/BE interface, giving rise to the SBH reduction at the TiO₂/BE interface and the growth of the oxygen-deficient phase (conduction path) from the TiO₂/BE interface, which is headed for the TE. During the growth of the conduction path from the TiO₂/BE, the electrochemical oxidation of the Ti⁽⁴⁻ⁿ⁾⁺ ions in the vicinity of the TE/TiO₂ takes place hindering the conduction path from reaching the TE. Furthermore, the chemical oxidation also takes place by virtue of the external oxygen, according to the chemical reactions in Eqs. 5.3 and 5.4. Consequently, the conduction path can not connect the BE with the TE. Therefore, the additional electroforming by applying the negative voltage/current is necessary to attract a large amount of oxygen vacancies to the

Table 5.2: Sketches of the electroforming mechanism for the BRS in the air.

TE/TiO₂ interface, leading to the formation of the complete conduction paths connecting the BE with the TE. Sketches of the electroforming mechanism for this case are depicted in Figs. (a) and (b) in Table 5.2.

(ii) Under the negative voltage/current application to the TE in the air a large

Table 5.3: Sketches of the electroforming mechanism for the BRS in vacuum.

Ambient	Positive	Negative
Vacuum	<p>+V or +I</p> <p>-V or -I</p>	<p>-V or -I</p>

number of oxygen vacancies is introduced at the TiO_2/BE interface, and thus the SBH at the interface is reduced. They drift and diffuse to the TE and are accumulated at the TE/TiO_2 interface, resulting in the growth of a conduction path from the TE/TiO_2 interface, which is headed for the BE. During the growth of the conduction path, the $\text{Ti}^{(4-n)+}$ ions in the vicinity of the TE/TiO_2 interface is electrochemically reduced due to the migration of oxygen vacancies to the TE. Simultaneously, the chemical oxidation occurs because of the external oxygen in the air, retarding the accumulation of the oxygen vacancies at the TE/TiO_2 interface and also the growth of the conduction path. This can be the reason for the longer electroforming time for the negative voltage/current application compared with the positive voltage/current application as can be noticed by comparing Figs. 5.9 and 5.11 with Fig. 5.12. A number of the oxygen vacancies accumulated at the TE/TiO_2 interface is not enough to lower the SBH at the TE/TiO_2 because of the chemical oxidation due to the external oxygen. Therefore, the additional electroforming with the positive voltage/current application is necessary for the formation of oxygen vacancies at the TE/TiO_2 interface to lead to the reduction of the SBH. Sketches of the electroforming mechanism for this case are depicted in Figs. (c) and (d) in Table 5.3.

(iii) In the electroforming performed in vacuum the chemical oxidation at the TE/TiO_2 interface is negligible. Under the positive voltage/current application to the TE, a large number of oxygen vacancies is introduced in the vicinity of the TE/TiO_2 interface. The formed oxygen vacancies drift and diffuse to the BE so that they are accumulated at the TiO_2/BE interface, resulting in the SBH reduction. A conduction path grown from the TiO_2/BE interface can reach the TE since the chemical oxidation can be ruled out. Therefore, the electroforming can be completed by the single positive voltage/current application. Figure (a) in Table 5.3 illustrates a sketch of

the electroforming mechanism for this case.

(iv) In case of the negative voltage/current application to the TE in vacuum, the oxygen vacancies formed at the TiO_2/BE interface drift and diffuse to the TE and can be accumulated at the TE/TiO_2 interface. And a conduction path grows from the TE/TiO_2 interface and reaches the BE without additional electroforming steps. Figure (b) in Table 5.3 depicts the electroforming mechanism for this case.

The non-homogeneous growth of the conduction paths is most possibly due to the non-uniform distribution of the electric field over the switching cells. The area of the conduction paths would be a few tens μm^2 as estimated from the SIMS analysis. Considering the low diffusivity and mobility of oxygen vacancies in the TiO_2 matrix, it can be estimated that the accumulation of oxygen vacancies at the cathode due to their drift and diffusion is a time-consuming phenomenon. This is well consistent with what was observed in Figs. 5.15 and 5.16, where it took more than 100 s for the second decrease in the resistance to occur.

5.3 Modeling of the conduction behavior in the electroformed TiO_2

The discussion on the electroforming in this chapter up to now indicates that the local reduction of TiO_2 is involved in the electroforming, forming the conduction paths consisting of a TiO_x phase. The area of a conduction path is believed to be a few μm according to the TOF-SIMS measurements. The distribution of oxygen vacancies in the TiO_x conduction path is expected to rely on the polarity of electroforming voltage because the reduction reaction occurs at the anode. The influence of the oxygen vacancy distribution on the electric conduction behavior can be estimated by solving the drift-diffusion equation of electrons⁴ at a given oxygen vacancy distribution. The one-dimensional current density of electrons as a function of coordinate x can be given by

$$J_e = n_e \mu_e \frac{d\epsilon_F}{dx}, \quad (5.5)$$

where n_e and μ_e denote the concentration and the mobility of free electrons, respectively. Concerning the high mobility of free electrons, the quasi-static distribution of the electrons can be assumed during the delay time of the applied stepwise voltage sweep.⁵ In heavily doped n-type semiconductor in which the Fermi energy is located above $\epsilon_c - 3k_B T$, where ϵ_c denotes the conduction band minimum, the Boltzmann statistics is no longer valid for the description of the electron distribution. Therefore,

⁴Since oxygen vacancies in TiO_2 are donors so that the electroformed TiO_2 is regarded as heavily doped n-type semiconductor. Since now only electrons are taken into account with ignoring holes.

⁵The delay time of stepwise voltage sweep was longer than 0.1 s so that the quasi-static approximation is reasonable.

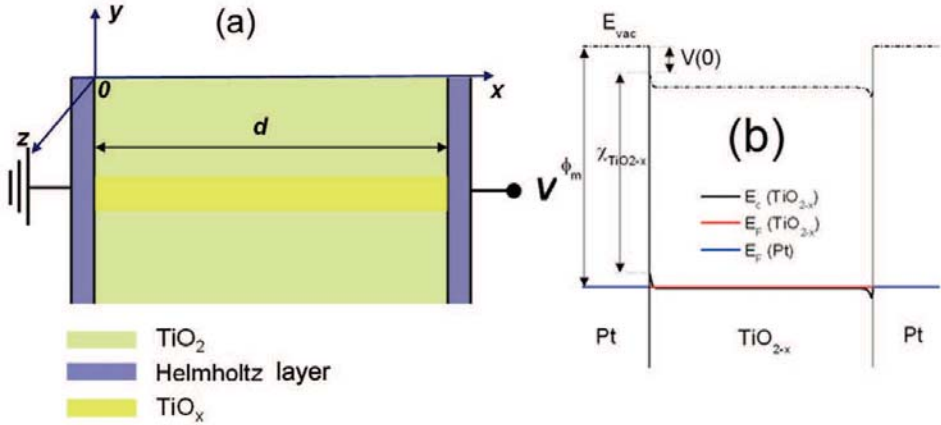


Figure 5.17: (a) Configuration of Pt/TiO₂/Pt for the calculation of current density-voltage curves. (b) Band diagram of a Pt/TiO_x/Pt junction at zero voltage.



Figure 5.18: Schematic of the Helmholtz and the double layers at a Pt/TiO₂ interface.

n_e is described using the Fermi-Dirac statistics as given by

$$n_e = \frac{\sqrt{2}m_e^{3/2}}{\hbar^3\pi^2} \int_{\epsilon_c}^{\infty} \frac{N\sqrt{\epsilon}}{1 + \exp\left(\frac{\epsilon - \epsilon_F}{k_B T}\right)} d\epsilon, \quad (5.6)$$

where m_e and \hbar denote the effective mass of an electron and the Planck constant, respectively.

The configuration of Pt/TiO₂/Pt for the calculation is shown in Fig. 5.17(a). The Helmholtz layer at the Pt/TiO₂ interfaces was taken into account for the description of the electric conduction behavior. The Helmholtz layer is supposed to be formed at a metal/electrolyte interface due to the separation of two oppositely charged layers, one is on the metal side and the other is on the electrolyte side at the interface.[49] Considering the high electron concentration in the metal, the electric field screening length is estimated to be very short and also the size of an electron must be very small compared to ions so that the charged layer on the metal side must be located

only at the interface without a remarkable electric field penetration into the metal. However, the ions working on the electric field screening in the electrolyte have a finite size, and thus the finite distance between the charged layer on the metal side and the center of the charge of the ions is supposed to be presented. In the ideal case, the distance is an ionic radius. The plane passing through the center of the ions nearest to the interface is called the Helmholtz plane and the layer between the interface and the Helmholtz plane is called the Helmholtz layer. The electric field in the electrolyte cannot be completely screened by the ions at the Helmholtz plane due to the finite size of the ions as well as a lower concentration of the ions compared to the electron concentration in the metal. The electric field is therefore additionally screened by the space charges in the vicinity of the interface. A schematic of the Helmholtz layer is depicted in Fig. 5.18.

On the assumption of no potential drop in Pt, the Schottky barrier height for the electrons transferring from the left electrode (LE) to a conduction path (TiO_x) in TiO_2 and from the right electrode (RE) to TiO_x can be expressed as $\phi_b^L = \phi_m - \chi_{\text{TiO}_x} - qV(0)$ and $\phi_b^R = \phi_m - \chi_{\text{TiO}_x} + qV_{ap} - qV(d)$, respectively. ϕ_m , χ_{TiO_x} , $V(0)$, $V(d)$, and V_{ap} denote the work function of Pt, the electron affinity of TiO_x , the electrostatic voltage at 0 and d , and an applied voltage to the RE, respectively. Therefore, the voltage drops in the left and right Helmholtz layers are $V(0)$ and $V_{ap} - V(d)$, respectively. The band diagram of the $\text{Pt}/\text{TiO}_x/\text{Pt}$ junction at 0 V is depicted in Fig. 5.17(b). In Fig. 5.17(b) it can be noticed that the Fermi energy of TiO_x is located above the conduction band minimum except for the interface regions, meaning the electron concentration is very high. Despite of the high electron concentration TiO_x is estimated to show semiconducting behavior because the difference between the Fermi energy and the conduction band minimum is just about $k_B T$.

5.3.1 Calculation of the voltage distribution in $\text{Pt}/\text{TiO}_x/\text{Pt}$

The voltage distribution in $\text{Pt}/\text{TiO}_x/\text{Pt}$ can be calculated using the Poisson equation given by

$$\frac{dE}{dx} = \frac{q\rho}{\varepsilon_r \varepsilon_0}, \quad (5.7)$$

where ε_r denotes the dielectric constant of TiO_x . By solving this equation E and V at $x = d$ can be obtained as the following equations.

$$E(d) = E(0) + \frac{q}{\varepsilon_r \varepsilon_0} \int_0^d \rho(x) dx \quad (5.8)$$

and

$$V(d) = V(0) - E(0)d - \frac{q}{\varepsilon_r \varepsilon_0} \int_0^d \int_0^x \rho(x') dx' dx. \quad (5.9)$$

On the assumption that the electric field penetration depth in Pt is very small so that the voltage drop in Pt is negligible, V_{ap} is equal to the summation of the voltage drops in the left Helmholtz layer, TiO_x , and the right Helmholtz layer (V_1, V_2, V_3). According to the continuity equation, V_1 and V_3 are $-d_1 \varepsilon_r E(0) / \varepsilon_{rH}$ and $-d_3 \varepsilon_r E(d) / \varepsilon_{rH}$, respectively. d_1, d_3 , and ε_{rH} denote the thickness of the left and right Helmholtz

layers and the dielectric constant of the Helmholtz layer, respectively. Therefore, V_{ap} can be rewritten as

$$V_{ap} = -\frac{d_1 \varepsilon_r}{\varepsilon_{rH}} E(0) - \frac{d_3 \varepsilon_r}{\varepsilon_{rH}} E(d) + V(d) - V(0). \quad (5.10)$$

Arranging Eq. 5.10 after entering Eqs. 5.9 and 5.8 into Eq. 5.10 gives $E(0)$ as expressed as

$$\begin{aligned} E(0) = & -\frac{1}{d_1 \varepsilon_r / \varepsilon_{rH} + d + d_3 \varepsilon_r / \varepsilon_{rH}} \left[V_{ap} + \frac{qd_3}{\varepsilon_{rH} \varepsilon_0} \int_0^d \rho(x') dx' \right. \\ & \left. + \frac{q}{\varepsilon_r \varepsilon_0} \int_0^d \int_0^x \rho(x') dx' dx \right]. \end{aligned} \quad (5.11)$$

Since $V(x)$ is given by

$$V(x) = V(0) - E(0)d - \frac{q}{\varepsilon_r \varepsilon_0} \int_0^x \int_0^{x'} \rho(x'') dx'' dx', \quad (5.12)$$

$V(x)$ can be obtained by entering Eq. 5.11 into Eq. 5.12.

5.3.2 Numerical calculation of the electric conduction behavior

The boundary conditions for the calculation of electron distribution are the current densities at the LE/TiO_x and TiO_x/RE interfaces (J_L and J_R). J_L is the summation of the current density from the LE to TiO_x (J_{LT}) and from TiO_x to the LE (J_{TL}), therefore, $J_L = J_{TL} - J_{LT}$. In the same way J_R can be given by $J_R = J_{RT} - J_{TR}$. J_{LT} and J_{RT} can be expressed using the Landauer-Büttiker formalism as[70]

$$J_{LT} = \frac{q\hbar}{4\pi^3 m_e} \int_{-\infty}^{\infty} \int_{-\infty}^{\infty} \int_{\sqrt{2m_e \phi_b^L} / \hbar}^{\infty} k_x f(\epsilon) dk_x dk_y dk_z \quad (5.13)$$

and

$$J_{RT} = \frac{q\hbar}{4\pi^3 m_e} \int_{-\infty}^{\infty} \int_{-\infty}^{\infty} \int_{-\infty}^{-\sqrt{2m_e \phi_b^R} / \hbar} k_x f(\epsilon) dk_x dk_y dk_z, \quad (5.14)$$

where k_x , k_y , and k_z denote the wave vectors of an electron in the directions x , y , and z , respectively. And $f(\epsilon)$ denotes the Fermi-Dirac distribution function. For a simpler calculation, the above equations can be approximately expresses as the form similar to the Richardson conduction equation. Equations 5.13 and 5.14 can be therefore described by

$$J_{LT} = qA \int_{\epsilon_c(0)}^{\infty} \frac{N'_c \sqrt{\epsilon}}{1 + \exp\left(\frac{\epsilon - \epsilon_{Fm}}{k_B T}\right)} d\epsilon \quad (5.15)$$

and

$$J_{RT} = qA \int_{\epsilon_c(d)}^{\infty} \frac{N'_c \sqrt{\epsilon}}{1 + \exp\left(\frac{\epsilon - \epsilon_{Fm} - qV_{ap}}{k_B T}\right)} d\epsilon, \quad (5.16)$$

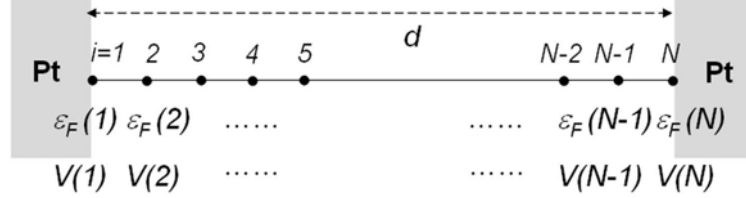


Figure 5.19: Arrangement of N nodes along x . The distance between neighboring nodes is $d/(N-1)$.

respectively. N'_c is given by $\sqrt{2}m_e^{3/2}/(\hbar^3\pi^2)$. A , $\epsilon_c(0)$, $\epsilon_c(d)$, and ϵ_{Fm} denote the velocity of the electron transfer, the conduction band edge at 0 and d , and the Fermi energy of the LE, respectively. In the same way J_{TL} and J_{TR} can be expressed as

$$J_{TL} = qv_{TL} \int_{\epsilon_c(0)}^{\infty} \frac{N'_c \sqrt{\epsilon - \epsilon_c(0)}}{1 + \exp \left[\frac{\epsilon - \epsilon_F(0)}{k_B T} \right]} d\epsilon \quad (5.17)$$

and

$$J_{TR} = qv_{TR} \int_{\epsilon_c(d)}^{\infty} \frac{N'_c \sqrt{\epsilon - \epsilon_c(d)}}{1 + \exp \left[\frac{\epsilon - \epsilon_F(d)}{k_B T} \right]} d\epsilon, \quad (5.18)$$

respectively. $\epsilon_F(0)$ and $\epsilon_F(d)$ mean the Fermi energy at 0 and d , respectively. v_{TL} (v_{TR}) means the velocity of the electron transfer from TiO_x to the LE (RE). They can be determined from a given A at zero voltage. Therefore, the boundary conditions J_L and J_R are given by

$$J_L = -qAN'_c \int_{\epsilon_c(0)}^{\infty} \frac{\sqrt{\epsilon}}{1 + \exp \left(\frac{\epsilon - \epsilon_{Fm}}{k_B T} \right)} d\epsilon + qv_{TL}N'_c \int_{\epsilon_c(0)}^{\infty} \frac{\sqrt{\epsilon - \epsilon_c(0)}}{1 + \exp \left[\frac{\epsilon - \epsilon_F(0)}{k_B T} \right]} d\epsilon \quad (5.19)$$

and

$$J_R = -qv_{TR}N'_c \int_{\epsilon_c(d)}^{\infty} \frac{\sqrt{\epsilon - \epsilon_c(d)}}{1 + \exp \left[\frac{\epsilon - \epsilon_F(d)}{k_B T} \right]} d\epsilon + qAN'_c \int_{\epsilon_c(d)}^{\infty} \frac{\sqrt{\epsilon}}{1 + \exp \left(\frac{\epsilon - \epsilon_{Fm} - qV_{ap}}{k_B T} \right)} d\epsilon, \quad (5.20)$$

respectively. ϵ_F and ϵ_c as a function of x can be obtained by solving Eq. 5.5 with the boundary conditions. Equation 5.5 cannot be analytically solved so that numerical methods should be used. For the calculation N nodes are arranged along x in TiO_x as can be seen in Fig. 5.19. The distance between neighboring nodes is $d/(N-1)$. As decreasing the distance, the calculation results become more reliable with avoiding calculation errors. In the steady state the current densities at each node [$J_e(i=1), J_e(i=2), J_e(i=3), \dots$] are equal, and thus the following equation should satisfy.

$$J_L = J_e(i=1) = J_e(i=2) = \dots = J_e(N) = J_R. \quad (5.21)$$

$\epsilon_c(i)$ can be described as $\epsilon_c(i) = \phi_b^L + \epsilon_{F(m)} - qV(i)$. Now there are $3N$ variables: $V(i)$, $\epsilon_F(i)$, and $d\epsilon_F/dx|_i$ where $i = 1, 2, \dots, N$. However, not all $3N$ variables are independent. Let us suppose that $V(i)$ where $i = 1, 2, \dots, N$ are known so that N variables are eliminated from the $3N$ variables. From the condition $J_L = J_e(i = 1)$, $d\epsilon_F/dx|_{i=1}$ can be described as a function of $\epsilon_F(i = 1)$,

$$\left. \frac{d\epsilon_F}{dx} \right|_{i=1} = f_1[\epsilon_F(i = 1)]. \quad (5.22)$$

And from the condition $J_L = J_e(i = 2)$, $d\epsilon_F/dx|_{i=2}$ can be described as

$$\left. \frac{d\epsilon_F}{dx} \right|_{i=2} = f_2[\epsilon_F(i = 1), \epsilon_F(i = 2)]. \quad (5.23)$$

On the condition that $d/(N-1)$ is small enough, $d\epsilon_F/dx|_{i=1}$ can be described as $(N-1)[\epsilon_F(i = 2) - \epsilon_F(i = 1)]/d$ so that the following equation is valid.

$$\epsilon_F(i = 2) = \epsilon_F(i = 1) + \frac{d}{N-1} \left. \frac{d\epsilon_F}{dx} \right|_{i=1}. \quad (5.24)$$

Therefore, $d\epsilon_F/dx|_{i=2}$ in Eq. 5.23 becomes a function of only $\epsilon_F(i = 1)$. In the same way, $\epsilon_F(i)$ and $d\epsilon_F/dx|_i$ at all nodes can be described as a function of only $\epsilon_F(i = 1)$. Now there are $N+1$ variables left: $V(i = 1), V(i = 2), \dots$, and $\epsilon_F(i = 1)$.

5.3.3 Algorithm of the calculation

To obtain proper voltage and Fermi energy profiles an iterative method is very helpful. Here, the Newton-Raphson method is used for the iteration.[71] The solution of a non-linear differential equation, for instance, the implicit finite difference equation, can be obtained by converting the non-linear differential equation into a linear equation. The linearized equation can be solved using a standard linear solver. However, the solution obtained from the first calculation can not be the real solution of the non-linear differential so that the calculation should be iterated unless the true solution is reached. Let us suppose that function f_i , where $i = \{1, 2, \dots, N\}$, depicted by \mathbf{f} , are functions of v_i , where $i = \{1, 2, \dots, N\}$, depicted by \mathbf{v} , and the equation which will be solved is $\mathbf{f} = 0$. First, an initial set of values $\mathbf{v}^{j=1}$ should be given to function \mathbf{f} . The second set of values $\mathbf{v}^{j=2}$ can be obtained from the following equation.

$$\mathbf{v}^{j+1} = \mathbf{v}^j - J(\mathbf{v}^j)^{-1} f(\mathbf{v}^j), \quad (5.25)$$

where

$$\mathbf{v}^j = \begin{pmatrix} v_1^j \\ v_2^j \\ \vdots \\ v_N^j \end{pmatrix}, \quad (5.26)$$

$$f(\mathbf{v}^j) = \begin{bmatrix} f_1^j(\mathbf{v}^j) \\ f_2^j(\mathbf{v}^j) \\ \vdots \\ f_N^j(\mathbf{v}^j) \end{bmatrix}, \quad (5.27)$$

and

$$J = \begin{pmatrix} \frac{\partial f_1}{\partial v_1} & \frac{\partial f_1}{\partial v_2} & \cdots & \frac{\partial f_1}{\partial v_N} \\ \frac{\partial f_2}{\partial v_1} & \frac{\partial f_2}{\partial v_2} & \cdots & \frac{\partial f_2}{\partial v_N} \\ \vdots & \vdots & \ddots & \vdots \\ \frac{\partial f_N}{\partial v_1} & \frac{\partial f_N}{\partial v_2} & \cdots & \frac{\partial f_N}{\partial v_N} \end{pmatrix}. \quad (5.28)$$

This process should be repeated until \mathbf{v}^j converges on stationary values. Then, \mathbf{v}^j are the solutions of the equation, $f_i = 0$ for all i . For this iteration initial values $\mathbf{v}^{j=1}$ should be carefully chosen, otherwise, the iteration will give non-realistic solutions.

Arbitrary voltage distribution along the nodes $[V^{j=1}(i), i = 1, 2, \dots, N]$ and $\epsilon_F^{j=1}(i = 1)$ are input as initial conditions. The $\epsilon_F^c(i = 1)$ ⁶ value is optimized at the given initial voltage distribution using the Newton-Raphson iteration. And thus $\epsilon_F^c(i)$ and $d\epsilon_F^c/dx|_i$ at all nodes can be optimized as well. The charge density $\rho^c(i), i = 1, 2, \dots, N$ can be calculated with $\epsilon_c(i)$ calculated from the initial voltage distribution and the optimized $\epsilon_F(i)$ and $d\epsilon_F/dx|_i$ using Eq. 5.6 and a given oxygen vacancy distribution. Using the Poisson equation the voltage distribution $V^c(i)$ can be calculated. The voltage distribution in continuum is given by Eq. 5.12. In a discrete system the integrations in Eq. 5.12 should be replaced by the summations of discrete functions. Using the trapezoidal rule[72] the first integral on the right side of Eq. 5.11 can be replaced by

$$\int_0^{\frac{d(n-1)}{N-1}} \rho(x') dx' \simeq \frac{d}{N-1} \left[\sum_{i=2}^{n-1} \rho(i) + \frac{1}{2} \rho(i=1) + \frac{1}{2} \rho(i=n) \right]. \quad (5.29)$$

If Eq. 5.29 is defined as $f(i = n)$, the double integral on the right side of Eq. 5.12 can be replaced by

$$\int_0^{\frac{d(n-1)}{N-1}} f(x') dx' \simeq \frac{d}{N-1} \left[\sum_{i=2}^{n-1} f(i) + \frac{1}{2} f(i=1) + \frac{1}{2} f(i=n) \right]. \quad (5.30)$$

Therefore, $V^c(i)$ can be evaluated at all nodes. A new function $S^{j=1}$ is defined as $S^{j=1}(i) = V^{j=1}(i) - V^c(i)$ meaning the difference between the input $V^{j=1}(i)$ and the calculated $V^c(i)$. Based on $S^{j=1}(i)$, a new set of $V^{j=2}(i)$ is input again and the same procedure is repeated to obtain $S^{j=2}(i)$. This iteration should continue until $S^j(i)$ becomes smaller than a tolerance (Δ), meaning the convergence on zero. The iteration procedure is summarized in Fig. 5.20.

5.3.4 Calculation results

Seven different distributions of oxygen vacancies (named A1 to A7) summarized in Table 5.5 were used for the simulation of electrical conduction behavior. A1 denotes a constant concentration of oxygen vacancies ($1.28 \times 10^{20} \text{ cm}^{-3}$). A2 to A7 denote various concentrations of oxygen vacancies near the interfaces and the same oxygen

⁶The superscript c means a value optimized using the iteration with the given voltage distribution $V^j(i)$

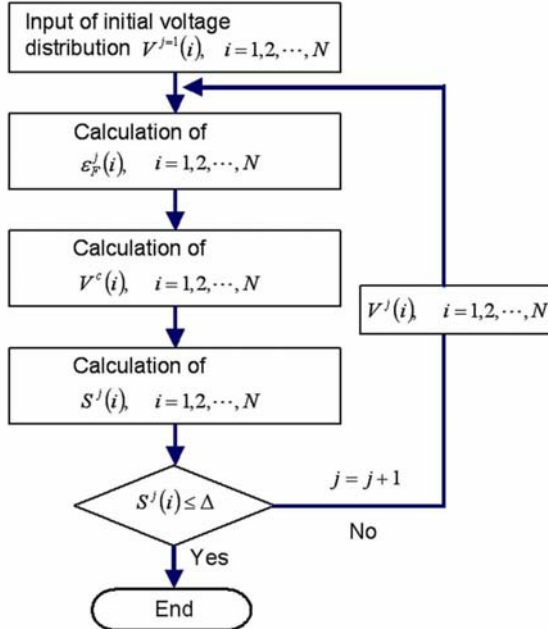


Figure 5.20: Flowchart of the calculation algorithm.

vacancy concentration ($1.28 \times 10^{20} \text{ cm}^{-3}$) in the bulk of TiO_x . For A2 to A7 the oxygen vacancy concentration was assumed to decay from the interfacial concentration to the bulk concentration along the direction to the center of TiO_x . Apart from A1 all were assumed to show the asymmetric distribution of oxygen vacancies, which is believed to be caused by electroforming as explained in the previous sections. Therefore, A2, A4, and A6 depict possible oxygen vacancy distributions for the anodic LE case for electroforming and A3, A5, and A7 for the anodic RE case.

Current density-voltage (J - V) curves were simulated with the parameters given in Table 5.4. In Table 5.4 ϕ_b is equal to $\phi_m - \chi_{\text{TiO}_x}$. And m_0 means the rest mass of an electron. The simulated J - V curves are shown in Fig. 5.21(b), which are named IV1 to IV7 for A1 to A7, respectively. IV1 is symmetric due to the symmetric A1. The others are asymmetric depending on the asymmetry of the oxygen vacancy distribution. IV2, IV4, and IV6 show a higher current density under the positive voltage than the negative voltage as can be expected. A higher oxygen vacancy concentration at the TiO_x/RE interface than the other interface causes a larger reduction of the SBH at the same interface so that more electrons can transfer from the RE to TiO_2 . The comparisons between IV3 and IV4, IV4 and IV5, IV5 and IV6, and IV6 and IV7 show that the increase in oxygen vacancy concentration at one interface have influence on not only the same interface but also the other interface. No matter which interface has a higher oxygen vacancy concentration, the SBH at both interfaces decreases with increasing an amount of oxygen vacancies in TiO_x . However, at the interface with a higher oxygen vacancy concentration the

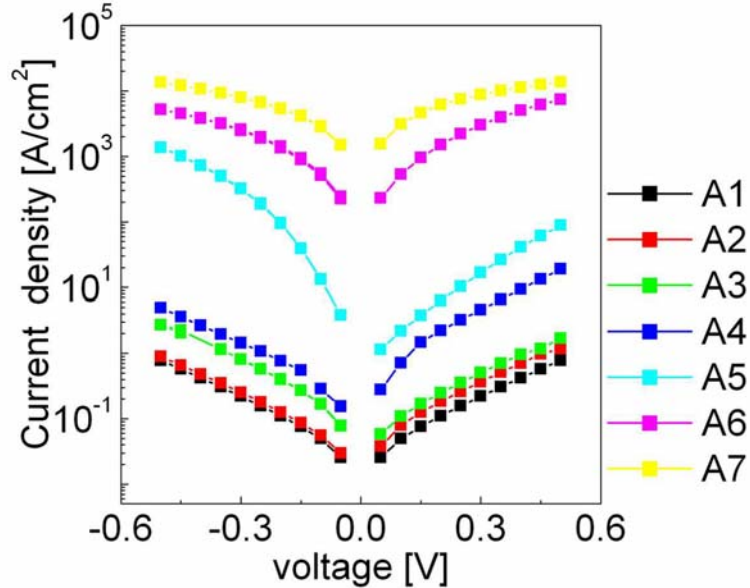


Figure 5.21: Calculated J - V curves for the oxygen vacancy distributions given in Table 5.5.

SBH undergoes relatively larger reduction so that the asymmetry of the J - V curves appears. For the same reason IV3 and IV5 show a higher current density under the negative voltage than the positive voltage.

With the extremely high oxygen vacancy concentration (A7) the J - V curve becomes almost symmetric regardless of the asymmetric oxygen vacancy distribution as shown in Fig. 5.21(b). The symmetric IV7 is in a good agreement with the symmetric I - V behavior observed in electroformed cells. As long as the Schottky barrier at two asymmetric interfaces works on current rectification J - V behavior cannot be symmetric. Figure 5.22(a) shows the SBH at the anode/ TiO_x interface for A1 to A7 with respect to the applied voltage. The SBHs for A7 are found to be negative in the whole voltage range, meaning none of the Schottky barriers can work on the current rectification (Ohmic contact) so that the symmetric J - V could be obtained. The SBH at the TiO_x /RE interface for A6 is also negative in the whole positive voltage range and below -0.25 V on the negative voltage side. Nevertheless, IV6 more or less shows asymmetry although it is not as obvious as IV3, IV4, and IV5. The asymmetry of IV6 is attributed to the electron depletion in the vicinity of the TiO_x /RE interface under the negative voltage (see Fig. 5.23). Compare with IV7, A6 has a less oxygen vacancy concentration at the TiO_x /RE interface so that the depth of the electric field penetration into TiO_x is deeper. Consequently, the electrons in the penetration depth are depleted so that the current density is lower than the positive voltage application case.

IV7 depicts a current density of about $1.4 \times 10^4 \text{ A} \cdot \text{cm}^{-2}$ at $\pm 0.5 \text{ V}$. I - V curves after the completion of electroforming showed a current of about a few mA as shown in Figs. 5.9, 5.11, and 5.12. Comparing the current values in these figures with the

Table 5.4: Parameters for the calculation

Parameter	Value
N	272
d	50 nm
ε_r	20
ε_{rH}	7[77]
d_1	2 Å
d_3	2 Å
μ_e	1 cm ² ·V ⁻¹ ·s ⁻¹
ϕ_b	0.5 eV
m_e	10 m ₀
A	6.25 cm·s ⁻¹
T	298 K

Table 5.5: Oxygen vacancy distribution

	Concentration at 0 [cm ⁻³]	middle of TiO _x	Concentration at d [cm ⁻³]
A1	1.28×10^{20}	1.28×10^{20}	1.28×10^{20}
A2	5×10^{20}	1.28×10^{20}	1.28×10^{20}
A3	5×10^{20}	1.28×10^{20}	10^{21}
A4	2×10^{21}	1.28×10^{20}	10^{21}
A5	2×10^{21}	1.28×10^{20}	5×10^{21}
A6	8×10^{21}	1.28×10^{20}	5×10^{21}
A7	8×10^{21}	1.28×10^{20}	1×10^{22}

J - V curves in Fig. 5.21 gives a few tens μm^2 sized TiO_x area that can contribute to the electrical conduction in the electroformed state. The TOF-SIMS measurements on the electroformed cell showed the bright spots whose radius was approximately a few μm , which were speculated to serve as conduction paths. The evaluated area of the conduction paths is therefore well consistent with the experimental observation.

The simulated conduction band and Fermi energy profiles for A1 to A7 at two different voltages (± 0.3 V) are shown in Fig. 5.23 with taking the Fermi energy of the LE as a reference energy 0. Figure 5.23 shows that the Fermi energy in the bulk region is above the conduction band edge for all cases. This is attributed to the high concentration of oxygen vacancies serving as donors. In Fig. 5.23 the conduction band profiles for A6 and A7 are found to show very weak electric field penetration into TiO_x. The electric field screening length is very short due to the high concentration of oxygen vacancies at the interfaces, and thus they show the weak electric field penetration.

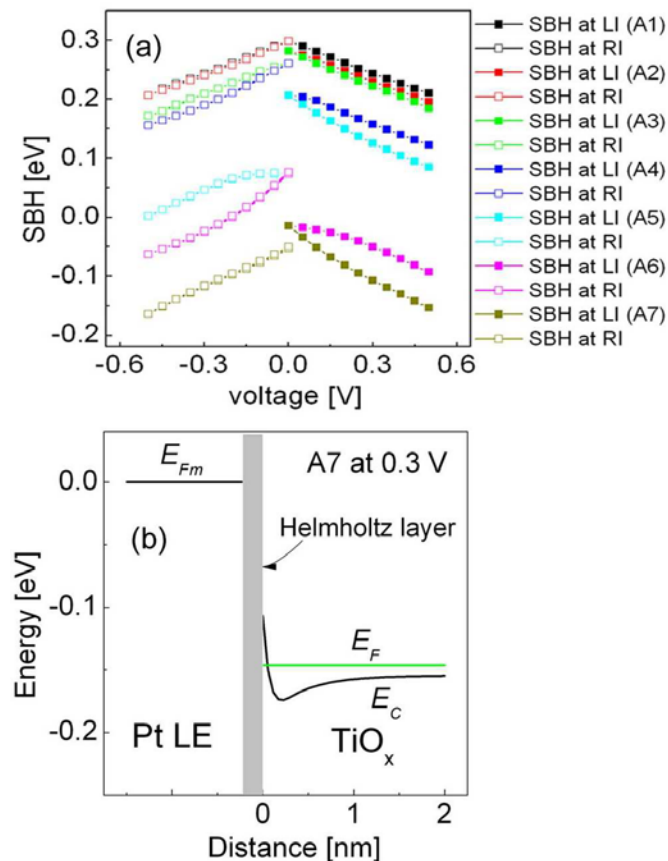


Figure 5.22: (a) SBH at the cathode/ TiO_x interface with respect to the applied voltage. The open symbols denote the SBH at TiO_x/RE and the closed symbols the SBH at LE/TiO_x . (b) Enlarged band diagram in the vicinity of the LE/TiO_x interface for A7 with applying 0.3 V to the RE.

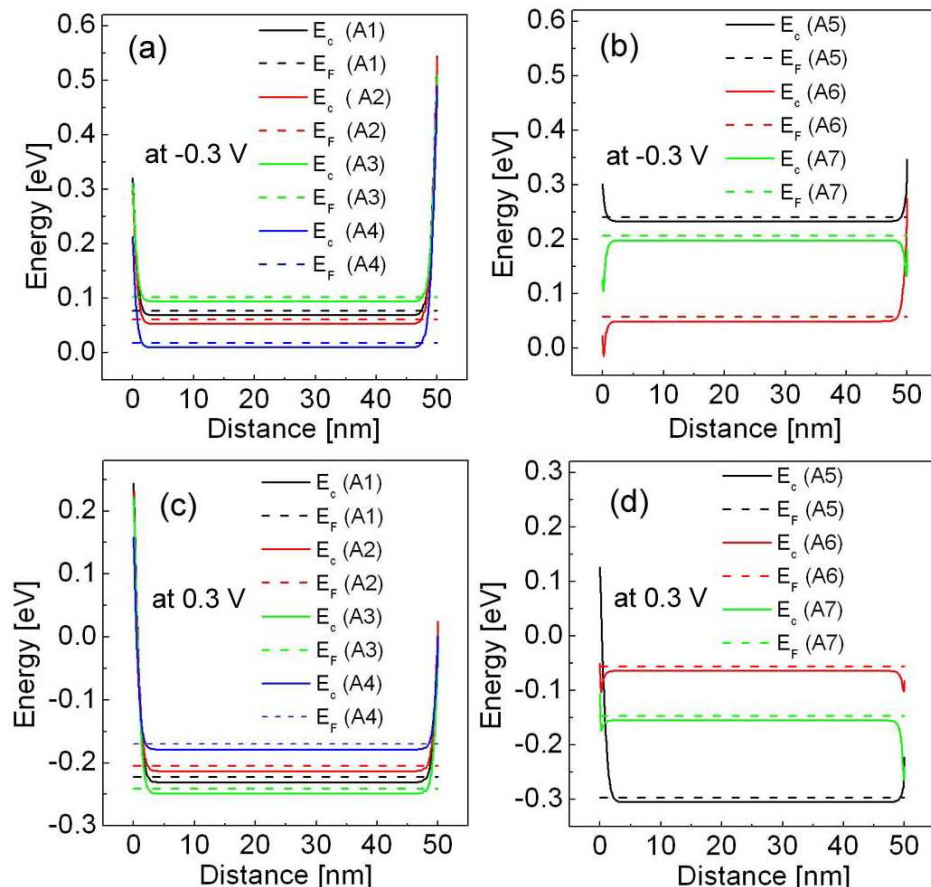


Figure 5.23: Simulated conduction band edge and Fermi energy profiles for A1 to A4 at an applied voltage of (a) -0.3 V and (c) 0.3 V and A5 to A7 at an applied voltage of (b) -0.3 V and (d) 0.3 V. The Fermi energy of the RE is taken as a reference energy 0.

Chapter 6

Unipolar resistive switching behavior

In this chapter the unipolar resistive switching behavior in Pt/TiO₂/Pt cells is presented. Similar to the bipolar resistive switching, electroforming is an initial process for the activation of the unipolar resistive switching. The unipolar resistive switching characteristics of stack switching cells as well as modified stack switching cells are introduced. Furthermore, the impedance spectra of both high and low resistance states are presented to speculate about the mechanism of the unipolar resistive switching.

6.1 Electroforming for unipolar resistive switching

Electroforming serves as an initial process for the unipolar resistive switching (URS) measurements in Pt/TiO₂/Pt. The electroforming can be performed using a voltage or a current source. In this chapter only the electroforming by voltage sweep will be dealt with because it is the simplest method to bring about the electroforming. The compliance current during the voltage sweep plays an important role in the activation of the URS. It is found that the electroforming with the compliance current in a particular window can activate the URS. However, the window is difficult to evaluate precisely because of the large fluctuation of the window. If the compliance current is lower than the lower limit of the window, the bipolar resistive switching (BRS) will be activated rather than the URS. If it is higher than the upper limit, TiO₂ will undergo permanent dielectric breakdown so that no switching will be observed. In case of 27 nm thick TiO₂ the lower and upper limits are about 1 mA and 10 mA, respectively.

Electroforming and URS measurements were performed on Pt/TiO₂(27 nm)/Pt stack switching cells using an Agilent B1500A semiconductor device analyzer. The current-voltage (*I*-*V*) curve undergoing the electroforming is shown in Fig. 6.1(a). The voltage sweep rate and the compliance current were 0.6 V/s and 7 mA, respectively. The abrupt jump of the current reaching the compliance current occurred at a voltage of 4.7 V. This voltage was regarded as the electroforming voltage. By the electroforming the pristine resistance state was immediately switched to the low resis-

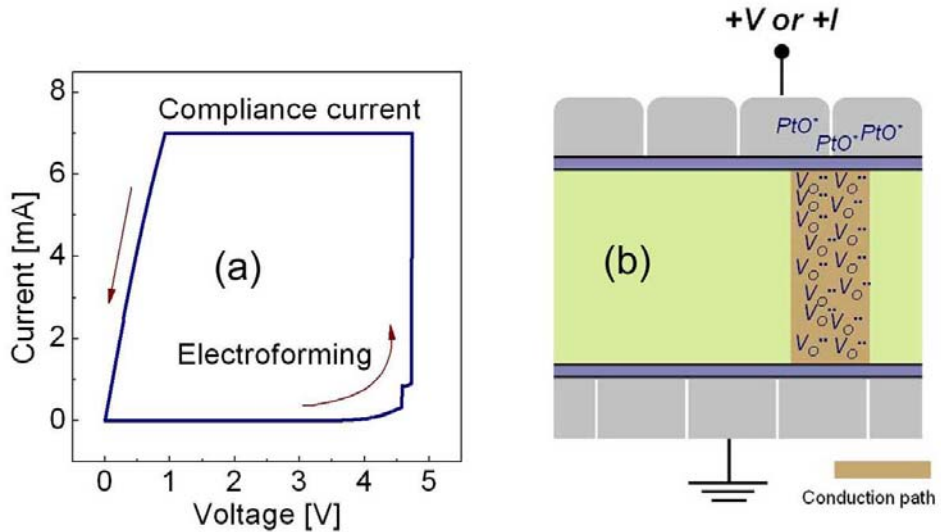


Figure 6.1: (a) Electroforming of a Pt/TiO₂(27 nm)/Pt stack switching cell by applying a voltage sweep. (b) Sketch of the distribution of oxygen vacancies in the electroformed Pt/TiO₂/Pt.

tance state (LRS) of the URS. The distribution of oxygen vacancies is sketched in Fig. 6.1(b). Ohmic contact is expected to be formed at both top electrode (TE)/TiO_x and TiO_x/bottom electrode (BE) interfaces. As mentioned in Chapter 5, a large amount of oxygen vacancies at the interfaces influences the Schottky barrier height (SBH). Very high concentration of oxygen vacancies ($> 10^{22} \text{ cm}^{-3}$) at the interfaces can eliminate the SBH, giving rise to the formation of the Ohmic contact.

6.2 Unipolar resistive switching characteristics

The URS behavior does not depend on the polarity of the applied voltage. Both set and reset switchings can be achieved under both positive and negative voltages. Furthermore, the polarity of the previous switching voltage does not have influence on the present switching behavior voltage. The absolute value of the applied voltage and the current therefore plays an important role in the URS so that the URS is also called nonpolar resistive switching. URS parameters such as the set and reset switching voltages, the reset current, and the resistances in the HRS and the LRS show quite large fluctuation with respect to a switching cycle number. The fluctuation can cause to misread the resistance state of memory cells, retarding the application of the URS of TiO₂ to resistive random access memory (RRAM) devices. Recently, literatures have reported the enhancement of URS stability achieved by modifying the structure of switching cells and optimizing the conditions for the switching film growth.[5, 51] The enhancement of the switching voltage stability in TiO₂ could be achieved by current-controlled set switching instead of voltage-controlled. High reset switching current also retards the application of the URS of TiO₂ to integrated

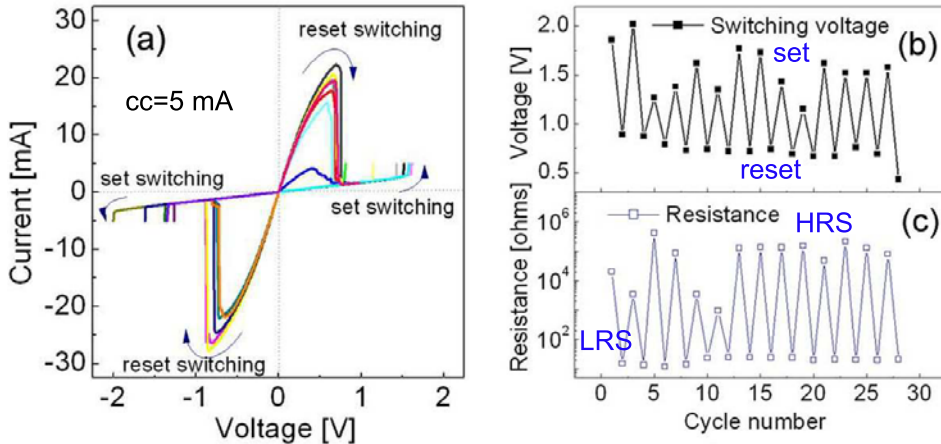


Figure 6.2: (a) URS curves of a Pt/TiO₂(27 nm)/Pt stack switching cell with a 100 μ m radius circular-shaped TE. The measurements were performed by applying voltage sweep. CC denotes the compliance current. (b) The switching voltage and (c) the resistance at a read-out voltage of 0.1 V with respect to a cycle number.

memory devices. In fact, the reset switching current of TiO₂ has been found to be higher than a few mA. As increasing the density of integrated circuits, the amount of current able to flow through the channel of a metal-oxide-semiconductor field effect transistor (MOSFET) decreases due to the decrease in the channel area so that the high density integrated circuits cannot meet such a high reset switching current. Therefore, it is a critical issue to lower the reset current of the URS behavior. A lower reset switching current (< 10 mA) could be observed in modified stack switching cells compared to stack switching cells. This might be attributed to the confined formation of conduction paths in the modified stack switching cells due to the geometry of the cells.

6.2.1 Unipolar resistive switching in stack switching cells

The URS of a Pt/TiO₂(27 nm)/Pt stack switching cell was measured by applying voltage sweeps with setting compliance current. The compliance current for the set switching was 5 mA. The diameter of the circular-shaped top electrode (TE) was 100 μ m. The measured URS curves are shown in Fig. 6.2(a). The figure shows the typical URS behavior of TiO₂ as have been reported in many literatures.[2, 3] The LRS was suddenly switched to the HRS at the reset switching voltage regardless of the polarity of the voltage. The HRS could be maintained as long as the applied voltage was less than the set switching voltage so that the resistance read-out could be performed at a voltage below the set switching voltage. By applying the set switching voltage the HRS could be switched back to the LRS. At the set switching voltage the current suddenly jumped reaching the compliance current also regardless of the polarity of the voltage.

The set and the reset switching voltages with respect to a cycle number are shown

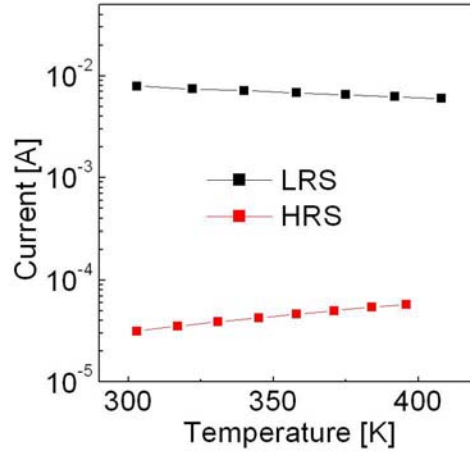


Figure 6.3: current versus temperature relations in the LRS and the HRS. The current was measured at a voltage of 0.1 V.

in Fig. 6.2(b). The voltage of both set switching and reset switching shows quite large fluctuation with respect to cycle numbers. The fluctuation must be prevented for the URS application to RRAM devices, otherwise, the devices cannot properly write and erase the information in the switching cells. The resistance of both states, HRS and LRS, with respect to a cycle number is plotted in Fig. 6.2(c). The resistance was evaluated at a read-out voltage of 0.1 V. The resistance of the HRS shows a large fluctuation compared to that of the LRS.

As shown in Fig. 6.2(a), at the reset switching voltage the resistance of the LRS suddenly increases to a more or less random resistance, showing a negative differential resistance (NDR) phenomenon. The increase in the resistance during the reset switching determines the resistance of the following HRS. Namely, if the increase in the resistance is high, the resistance of the following HRS will be high, leading to the large ratio of the HRS to the LRS.

The mechanism of the URS can be estimated based on the fuse and antifuse of metallic conduction paths.[2, 52] In fact, it was found that the LRS of the URS in TiO_2 shows metallic conduction behavior, which could be identified by measuring the resistance at various temperatures. The measured current-temperature relations for both LRS and HRS are shown Fig. 6.3. The resistance state was fixed while the current was measured at the temperatures. The resistance read-out voltage was 0.1 V. The LRS data points show the increase in the resistance with increasing temperature, suggesting metallic conduction behavior. As mentioned earlier, the electroforming is regarded to lead to the formation of the conduction paths consisting of many oxygen vacancies. It can be therefore speculated that the conduction paths in the LRS are composed of $\text{TiO}_{2-n/2}$ for approximately $n > 1.5$, which is a metallic phase.

The conduction of the HRS shows thermally activated behavior as shown in Fig. 6.3. The activation energy of the conduction was about a few tens meV. The conduction paths might be considered to be locally ruptured during the reset switching.

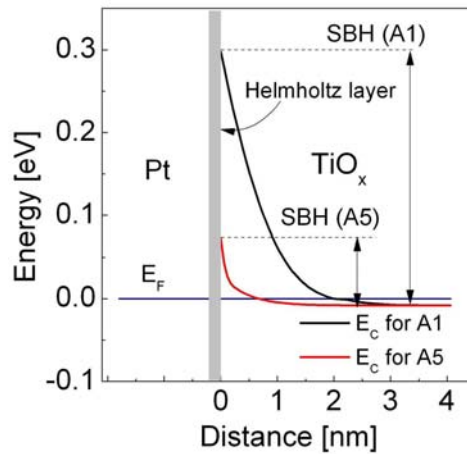


Figure 6.4: Conduction band minimum profiles in the vicinity of the Pt/TiO_x interface for A1 and A5 in Table 5.5 The SBHs for A1 and A5 are indicated.

The ruptured part consists of an insulating phase where the current is thermally activated. The resistance of the HRS is governed by the ruptured conduction paths so that the overall conduction in the HRS shows the thermal activation. The conduction behavior in the HRS with the small activation energy can be possibly explained by the following two mechanisms.

- Electron hopping along localized shallow energy states introduced by oxygen vacancies in the band gap.
- Electron conduction over the Schottky barrier height (SBH) at the TiO₂/cathode interface lowered by the presence of many oxygen vacancies at the interface, due to heavy self-doping.

According to first principle calculations of the localized energy states due to oxygen vacancies in TiO₂, shallow energy states are formed below the bottom edge of the conduction band ($\sim 0.2\text{eV}$).^[62] This is consistent with the UV photoelectron spectroscopy (UPS) analysis on reduced TiO₂.^[53] Electrons can be therefore expected to migrate from the virtual cathode to the anode by hopping along the shallow energy states. However, if the energy states of oxygen vacancies are comparably shallow, band conduction is more favorable than the electron hopping because the oxygen vacancies are able to be fully ionized. If a large amount of space charges (here, oxygen vacancies) is present in TiO₂, a large voltage will be applied in the Helmholtz layer at the Pt/TiO₂ interfaces. The voltage drop in the Helmholtz layer can reduce the SBH at the interfaces to be a few tens eV. The band diagrams of Pt/TiO_x/Pt with two different distributions of oxygen vacancies, A1 and A5 in Table 5.5, are illustrated in Fig. 6.4. A5 denotes a higher concentration of oxygen vacancies in the vicinity the Pt/TiO_x interface compared with A1. It is found that the SBH for A5 is lower than that for A1, proving the SBH reduction depending on the oxygen

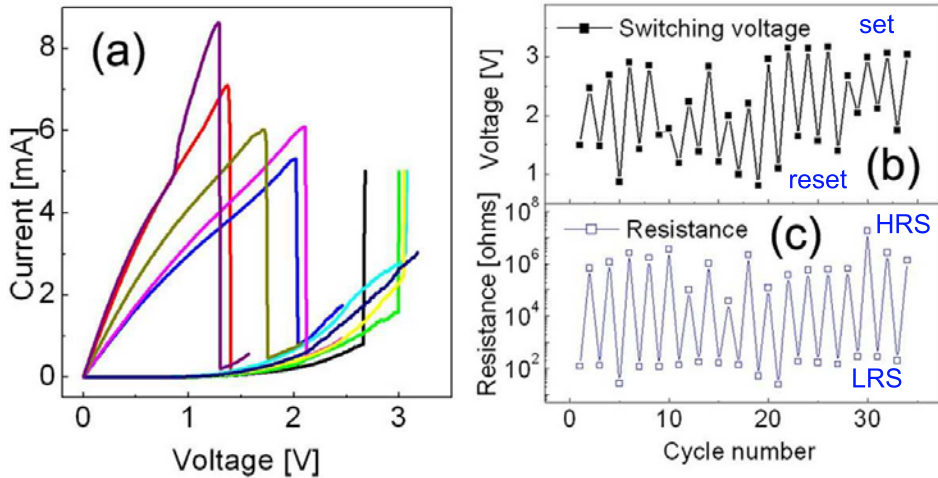


Figure 6.5: (a) URS curves of a Pt/TiO₂(27 nm)/Pt stack switching cell with a 150 μ m radius circular-shaped TE. The measurements were performed by applying voltage sweep. (b) The switching voltage and (c) the resistance at a read-out voltage of 0.1 V with respect to cycle numbers.

vacancy concentration at the Pt/TiO_x interface. This mechanism is more probable than the hopping mechanism because the latter mechanism regards band conduction as a conduction mechanism and also takes into account fully ionized oxygen vacancies that are probably involved in the URS.

The URS measurements were carried out on a Pt/TiO₂(27 nm)/Pt stack switching cell with a different radius circular-shaped TE (150 μ m). The compliance current for the set switching was set to be 7 mA. URS switching curves of the sample are shown in Fig. 6.5(a). The switching curves look similar to those of the smaller switching cell shown in Fig. 6.2. The reset current of the larger switching cell in Fig. 6.5 is lower than that of the smaller cell. However, in the statistics it was found that the fluctuation of the URS behavior including the reset current and the switching voltage in the larger cell was larger than the smaller cell so that no clear area dependence of the URS could be found from the measurement results. The switching voltage and the resistance with respect to a cycle number are shown in Figs. 6.5(b) and (c), respectively.

As mentioned earlier, at a set switching voltage current jumps so that it reaches compliance current. When the current stays at the compliance current, the applied current to a switching cell can be hardly evaluated using the two terminal measurement method. Even though the voltage can be evaluated using the four terminal method, the voltage is no longer a controllable parameter so that it is better to avoid the current at the compliance. By applying a current sweep instead of a voltage sweep set switching can be achieved without setting compliance current so that the uncertainty of set switching can be eliminated. Voltage-control for reset switching still deserves to be applied because compliance current plays no role in the reset switching. Figure 6.6 shows the comparison between voltage-controlled

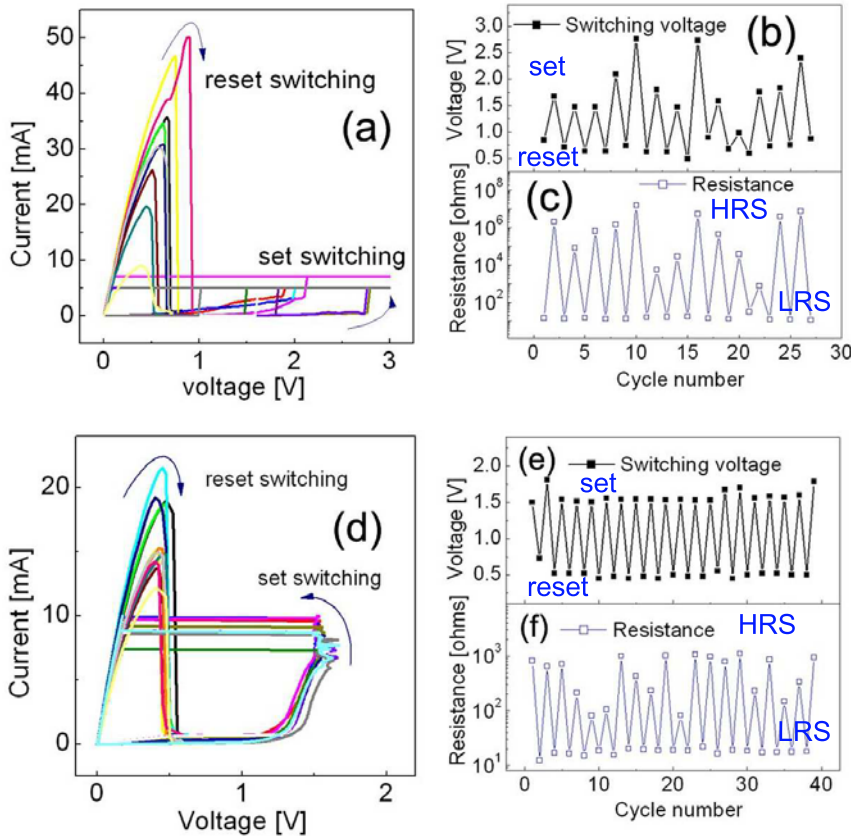


Figure 6.6: (a) URS curves of a Pt/TiO₂(27 nm)/Pt stack switching cell with a 100 μ m radius circular-shaped TE. The reset and set switchings were performed by controlling a voltage. (b) The switching voltage and (c) the resistance of the URS shown in Fig. (a) with respect to a cycle number. (d) URS curves of the same cell whose set and reset switching curves were performed by controlling current and voltage, respectively. (e) The switching voltage and (f) the resistance of the URS shown in Fig. (d) with respect to a cycle number.

and current-controlled set switching cases. The measurements were carried out on the same switching cell. The voltage-controlled set switching case was prior to the current-controlled switching case. The HRS resistance was evaluated at a read-out current of 100 μ A and the LRS at a read-out voltage of 0.1 V. In Fig. 6.6(e) it can be noticed that the current-controlled set switching case shows a more stable URS behavior with a smaller fluctuation of the set and reset switching voltages. The fluctuation of the LRS resistance could be also improved by the current-controlled set switching. However, the HRS resistance still showed a quite large fluctuation as shown in Fig. 6.6(f). The enhancement of the URS stability might be attributed to confined recovery of the conduction paths, once ruptured by the reset switching, during the current-controlled set switching. In the current-controlled set switching,

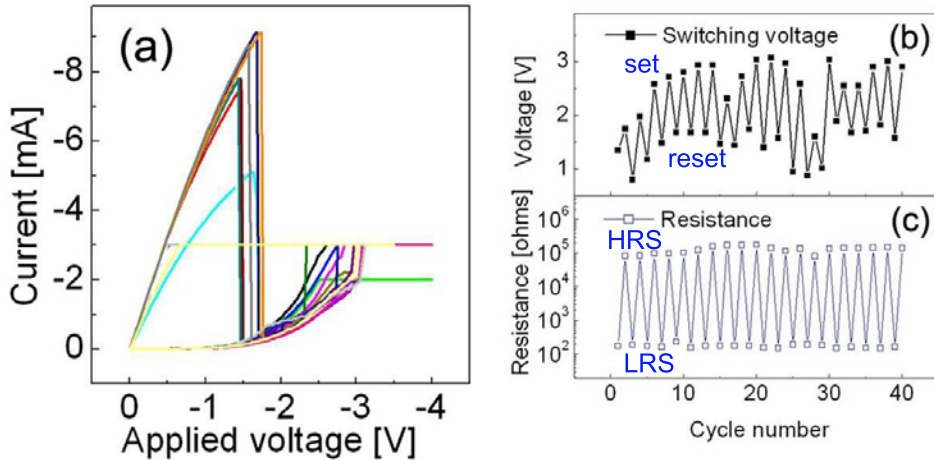


Figure 6.7: (a) URS curves of a Pt(10 nm)/TiO₂(27 nm)/Pt(10 nm) modified stack switching cell. (b) The switching voltage and (c) the resistance at a read-out voltage of 0.1 V with respect to cycle numbers.

the applied current kept increasing up to the set maximum current even after the set switching occurred so that the input parameter (current) was all the time under control. However, in the voltage-controlled set switching, the input parameter (voltage) became out of control at the set switching voltage as soon as the current reached the compliance current. The recovery of the ruptured conduction paths is therefore believed to have occurred in a more or less random way without virtue of the controlled voltage. Therefore, the fluctuation of the LRS resistance after the voltage-controlled set switching is speculated to be attributed to the random recovery.

6.2.2 Unipolar resistive switching in modified stack switching cells

URS measurements were carried out on a modified stack switching cell with 10 nm thick TE and BE and 27 nm thick TiO₂ by applying a voltage sweep. The same switching cell, whose scanning electron microscope image after electroforming was shown in Fig. 5.4(a) in Chapter 5, was used for the URS measurements. The compliance current for the set switching was set to be 3 mA. The measured URS curves are shown in Fig. 6.7(a). The switching voltage and the resistance with respect to a cycle number are shown in Figs. 6.7(b) and (c), respectively. It can be noticed that the reset current is lower than that shown in Fig. 6.2(a) and also the resistance in both HRS and LRS with respect to a cycle number is less fluctuating compare to the stack switching cells. One can estimate that the less reset current is due to a smaller switching cell size than the cell area of the stack cells. Since the reset current does not seem to be proportional to the cell area as has been reported,[54] the less reset current is unlikely to be caused by only the small area effect. A simple electrostatic calculation shows that the highest electric field is applied at the

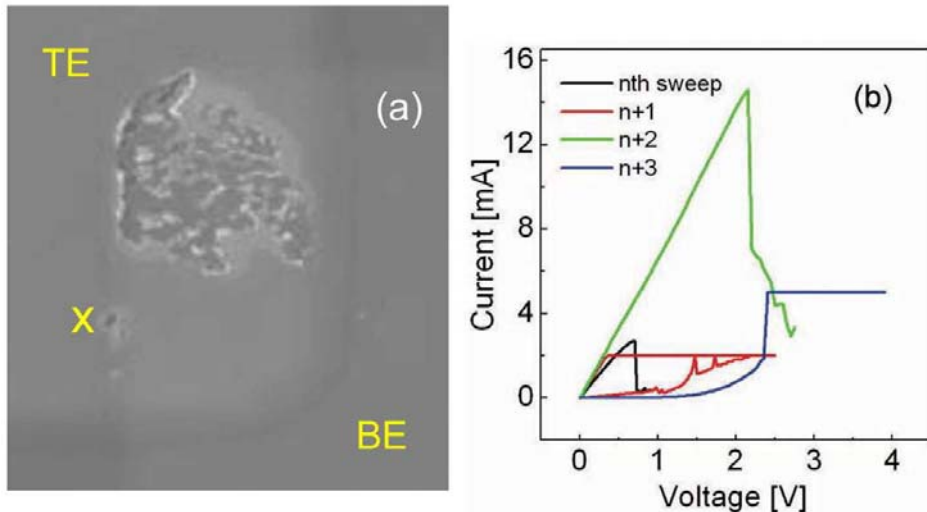


Figure 6.8: (a) SEM image of a modified stack switching cell. (b) URS curves of the same switching cell

corner of the BE under the applied voltage. In fact, it could be observed that the damage on the surface of a modified stack switching cell initiated at the corner during electroforming as mentioned in Chapter 5. The location of conduction paths could be therefore confined at the corner due to the highly nonhomogeneous electric field distribution so that the URS could be achieved by the recovery and rupture of the confined conduction paths, leading to the enhancement of the resistance stability as a function of a cycle number.

Very interesting correlation between URS and a simultaneous change in the surface of the switching cell could be observed in the modified stack switching cell. Most damage on the surface near the BE corner shown in Fig. 6.8 resulted from the electroforming. However, the damaged indicated by yellow \times in Fig. 6.8(a) was formed during the $(n + 1)$ th sweep for the set switching shown in Fig. 6.8(b). After this set switching accompanied with the damage, the reset current for the following reset switching ($(n + 2)$ th sweep) increased more than 5 times and the resistance decreased. The new damage is believed to have been caused by the formation of new conduction paths. As mentioned earlier, the metallic conduction paths can be considered to consist of $\text{TiO}_{2-n/2}$ for about $n > 1.5$. The formation of the new conduction paths is expected to give rise to oxygen gas evolution near the paths at the anode. Therefore, the oxygen gas evolution and the Joule heating due to the degradation of the local resistance might cause the damage indicated in Fig. 6.8(b). Consequently, the newly formed conduction paths decreased the resistance of the cell and more current was needed to rupture the additional conduction paths.

6.2.3 Impedance spectroscopy

Impedance spectroscopy is a very useful method to define the arrangements of electrical components in dielectric films, including resistance, inductance, and capacitance as well as a dielectric dispersion in a frequency domain.[38, 67] Therefore, impedance spectroscopy of TiO₂ in the three different resistance states, pristine state (PS), HRS, and LRS was performed to provide information on the URS mechanism.

Sample test (ST) capacitors consisting of Pt/TiO₂(27 nm)/Pt and short-circuit standard (SCS) capacitors excluding the TiO₂ thin film were fabricated and the impedance in the frequency domain (100 Hz - 10 MHz) for the three different resistive states was investigated. In order to obtain the intrinsic impedance, one has to calibrate the measured impedance spectra of the ST by removing the parasitic impedance mainly due to electrodes and wiring, which can be measured from the SCS capacitors. For further insight into the URS mechanism, the impedance spectra were simulated using finite element analysis (FEA) for two switching mechanisms, the filament model and the homogeneous model.[68]

The impedance spectra of the ST and SCS capacitors in the frequency domain (100 Hz - 10 MHz) were measured at zero dc bias with a voltage oscillation amplitude of 50 mV using an HP4194A impedance analyzer. It is a proper assumption to regard the electrode impedance, Z_s , due to the resistive and inductive components of the electrode, as being in series with the intrinsic TiO₂ impedance, Z_c . Therefore, the impedance of ST, Z_{ST} , is given by $Z_{ST} = Z_s + Z_c$. Because SCS has no TiO₂ layer (characterized by Z_c), $Z_{SCS} = Z_s$. Hence, Z_c is simply expressed by $Z_c = Z_{ST} - Z_{SCS}$. For the analysis of the impedance spectra, it is much simpler to describe them in terms of admittance, $Y_c = Z_c^{-1}$; which is therefore used in this chapter. A proper equivalent circuit of the filament model is an element with parallel connection of a capacitance and ac and dc conductance. The equivalent circuit of the homogeneous model is different, namely a series connection of at least two such elements representing a conducting homogeneous bulk and a less conducting, but switchable thin region covering the whole capacitor area homogeneously, e.g. interface regions (for illustration see Fig. 6.10). The equivalent circuit of the filament model can be expressed as

$$Y_c = i2\pi\omega C(\omega) + 1/R_L, \quad (6.1)$$

where

$$C(\omega) = C'(\omega) - iC''(\omega) = [1 + \chi'(\omega) - i\chi''(\omega)]\varepsilon_0 A/t, \quad (6.2)$$

where ω , R_L , ε_0 , and t denote the frequency, the resistance due to dc leakage current in TiO₂, the permittivity of vacuum, and the area and the thickness of TiO₂, respectively. C' , C'' , χ' , and χ'' are the real and imaginary parts of the complex capacitance and susceptibility, respectively. C'' , attributed to dielectric damping, makes the ac conductance distinguishable from the dc conductance due to leakage current. Therefore, the real and imaginary parts of the admittance [$Re(Y_c)$ and $Im(Y_c)$] can be described as

$$Re(Y_c) = 2\pi\omega\chi''(\omega)\varepsilon_0 A/t + 1/R_L \quad (6.3)$$

and

$$Im(Y_c) = 2\pi\omega[1 + \chi'(\omega)]\varepsilon_0 A/t. \quad (6.4)$$

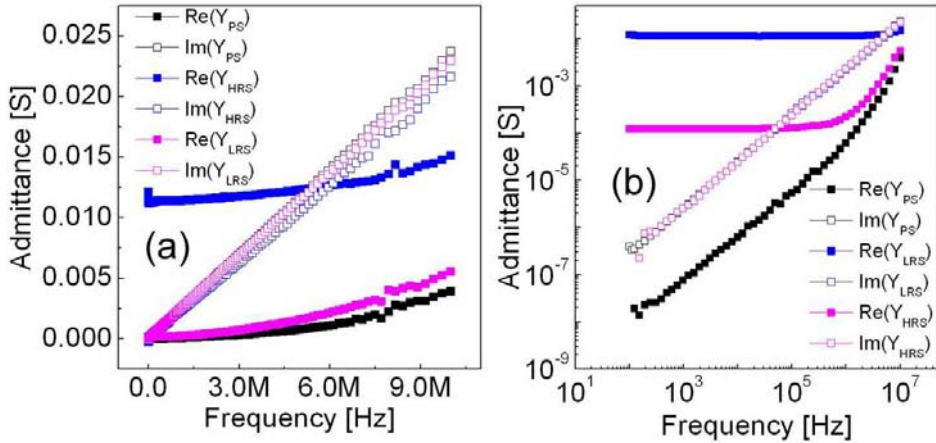


Figure 6.9: Frequency dependence of the real (closed symbols) and imaginary (open symbols) parts of the intrinsic admittance (Y_c) of TiO_2 at the various resistance states, pristine state (subscript PS), HRS (subscript HRS) and LRS (subscript LRS) on (a) linear and (b) log scales.

Figures 6.9(a) and (b) show the real and imaginary parts of the calibrated intrinsic admittance of TiO_2 (in PS, HRS, and LRS, respectively) on linear and log scales, respectively. For the case of PS, R_L^{-1} can be neglected because the contribution of the dc conductance to the admittance seems to be negligible. In Fig. 6.9(b) the real and imaginary parts of the complex admittance in PS, $Re(Y_{PS})$ and $Im(Y_{PS})$, show a power-law behavior up to about 2 MHz. They satisfy the Curie-von Schweidler relaxation law where both χ' and χ'' are given by a power-law, ω^{n-1} , with n slightly less than unity.[47, 48] Therefore, their ratio becomes constant as given by the following equation.

$$\frac{\chi''(\omega)}{1 + \chi'(\omega)} \simeq \frac{\chi''(\omega)}{\chi'(\omega)} = \cot\left(\frac{n\pi}{2}\right). \quad (6.5)$$

The exponent n is found to be 0.975, for which a dielectric dispersion in the given frequency domain is very weak. Therefore, both C' and C'' can be regarded as constants in the given domain. Furthermore, Figure 6.9 shows that the different resistance states have negligible influence on $Im(Y_c)$, the capacitance C' is almost constant regardless of the resistive states.

It is also found that $Re(Y_c)$ of the HRS is almost constant until the ac conductance becomes dominant, which is consistent with the assumption of a parallel connection between the ac and dc conductance satisfying Eq. 6.1. For the case of the LRS the dc conductance is high enough to hide the ac conductance completely in the whole frequency domain. These observations can serve as critical clues to identify a mechanism of the resistive switching, e.g. either a homogeneous model or the filament model.

For a comparison between the impedance spectra obtained from the two suggested mechanisms, numerical calculations of the impedance spectra for the 27 nm

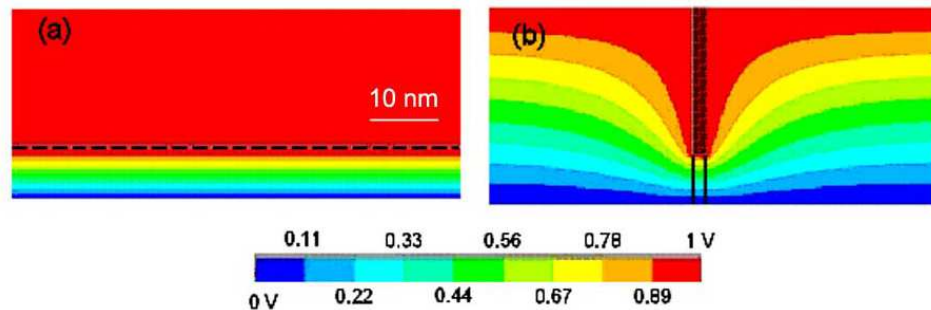


Figure 6.10: Voltage distribution (application of 1 V to the TE) in TiO_2 in the HRS for (a) the homogeneous model and (b) the filament model obtained by FEA

thick film were performed using FEA with three different distributions of the charge carriers (electrons) in the dielectric film. (i) First, a very low and uniform carrier density in the dielectric film corresponding to PS. (ii) Second, uniformly distributed carriers in conducting and insulating regions, which are separated by a virtual cathode, corresponding to the homogeneous model with interface regions. (iii) Last, a highly localized high density of carriers in a filament.

The numerically calculated voltage distributions in the HRS for the cases (ii) and (iii) are shown in Figs. 6.10(a) and (b). The voltage distribution of the case (i) is omitted as a separate figure because the result is obvious and identical to that at the left and right edges in Fig. 6.10(b). The dashed line of Fig. 6.10(a) designates the virtual cathode dividing the dielectric into a conducting (upper) and insulating (lower) region. The hatched area in Fig. 6.10(b) designates a ruptured, highly conducting filament.

For the FEA calculation of the homogeneous model shown in Fig. 6.10(a), the thickness of the conducting and insulating phases in the HRS are assumed to be 20 nm and 7 nm, respectively. Using the resistances in the LRS and the HRS in Fig. 6.9, 83 Ω and 8300 Ω , respectively, and the corresponding capacitor area of 0.015 mm^2 , the resistivities of the conducting and insulating regions are $4.6 \times 10^3 \Omega\cdot\text{cm}$ and $1.8 \times 10^6 \Omega\cdot\text{cm}$, respectively. For the FEA calculation of the filament model shown in Fig. 6.10(b) the width of the conducting filament is set to 2 nm. In the HRS the filament is assumed to be destroyed on a length of 7 nm so that only 20 nm still have a high conductivity. Obtaining the resistance of a highly conducting filament from conductive atomic force microscope measurements, the resistivity of the 2 nm wide filament is calculated to be $5.2 \times 10^{-3} \Omega\cdot\text{cm}$. To fit the resistance in the LRS in Fig. 6.9, about 5200 filaments must be present, resulting in a density of $3.45 \times 10^7 \text{ cm}^{-2}$. Fitting the HRS with also this density gives the resistivity of the broken filament part, which is $1.93 \Omega\cdot\text{cm}$. The resistivity of the insulating phase is $6.63 \times 10^9 \Omega\cdot\text{cm}$ calculated from the resistance of the PS- TiO_2 . It should be pointed out that these filament resistivities are only order of magnitude estimations because the accurate areal density and the dimensions of filaments are still ambiguous, leaving many open questions. In the present chapter, the conductivity distribution is not taken into account since the distribution would not influence the simulation results.

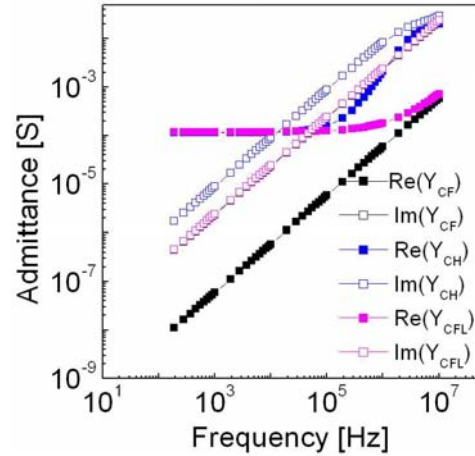


Figure 6.11: Numerically calculated impedance spectra described in terms of the real (closed symbols) and imaginary (open symbols) part of the complex admittance (Y) of PS excluding a good conducting phase (Y_{CF}), the homogeneous model (Y_{CH}), and the filament model (Y_{CFL}), respectively.

The conduction behavior attributed to localized conduction paths hardly affects the bulk dielectric behavior of TiO_2 (no effect on $Im(Y_c)$) as well as the frequency dispersion of $Re(Y_c)$.

The impedance spectra for all three cases were calculated with the parameters mentioned above and are shown in Figs. 6.11(a) and (b). It can be noted that the calculations for the homogeneous model, case (ii), give rise to great changes of the complex admittance, which is in disagreement with the experimental impedance spectra. On the other hand, the impedance spectra of the filament model are in much better agreement with the experimental data.

As shown in Fig. 6.9, the imaginary part of the complex admittance is barely dependent on the resistance state. The whole area of the conduction paths is very small compared with the total area of the switching cell so that the contribution of the conduction paths to the imaginary part of the complex admittance is not prominent. In fact, the estimated area of the conduction paths in a switching cell with a pad-size of $7850 \mu\text{m}^2$ is a few tens μm^2 as discussed in Chapter 5. Therefore, the influence of the migration of oxygen vacancies believed to take place during the URS on the capacitance of the macroscopic pad could not be identified.

Chapter 7

Bipolar resistive switching behavior

In this chapter the bipolar resistive switching (BRS) characteristics of Pt/TiO₂/Pt switching cells are presented. The BRS behavior in Pt/TiO₂/Pt was partly explained in Chapter 5. Here, the effect of the thickness of TiO₂, pad-size, and measurement ambient on the BRS behavior is investigated. The observed BRS characteristics are interpreted based on the evidences obtained from the electroforming investigation. Finally, the mechanism of the BRS is suggested in terms of redox reactions involving oxygen ions and oxygen vacancies at the Pt/TiO₂ interfaces. The suggested mechanism is proven to be able to explain the BRS behavior by simulating hysteretic current-voltage behavior. The simulation is performed using the finite difference method.

7.1 Voltage-controlled BRS measurements

Voltage-controlled BRS measurements were performed on electroformed Pt/TiO₂/Pt stack switching cells by applying a voltage sweep to the top electrode (TE). The switching cells with various thicknesses of TiO₂ were prepared to identify the TiO₂ thickness dependence. The BRS measurements on the switching cells with two different cell sizes were also carried out to identify the pad-size dependence. Not only the cell geometry dependence but also the applied voltage sweep dependence was investigated.

7.1.1 Polarity dependence of the BRS

In the BRS of Pt/TiO₂/Pt, the polarity of the set and the reset switching voltages is determined by the first voltage cycle. As-electroformed TiO₂ shows negative differential resistance (NDR) during the first voltage sweep regardless of the voltage polarity. Figure 7.1 shows the comparison between the BRS curves measured by applying a voltage sweep starting with the different voltage polarities. The BRS in Fig. 7.1(a) was measured by applying the voltage cycle shown in the inset of Fig. 7.1(a), where the first sweep polarity was positive. The BRS showed the set and the reset switchings under the negative and the positive voltages, respectively. The BRS

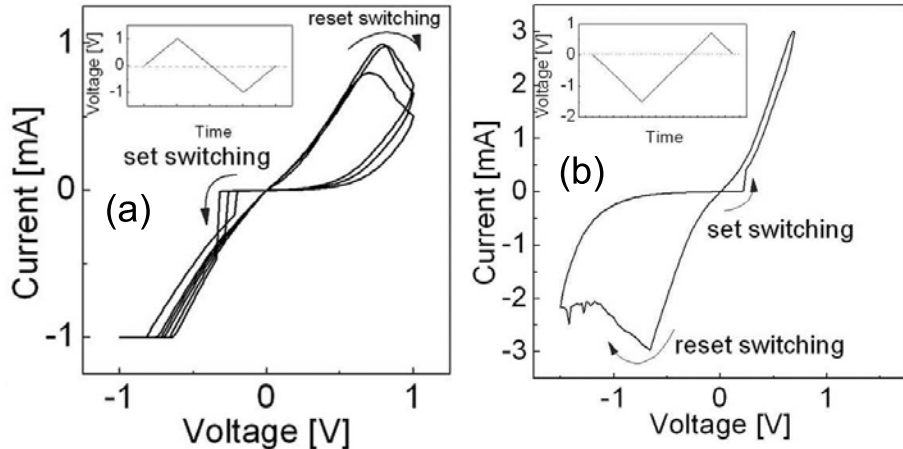


Figure 7.1: Dependence of the BRS behavior on the applied voltage cycle. The insets depict the applied voltage cycle.

in Fig. 7.1(b) was obtained by applying the voltage cycle in the inset of Fig. 7.1(b), where the first sweep polarity was negative. The set and the reset switchings were found to occur under the positive and the negative voltages, respectively, which were the opposite way compared to Fig. 7.1(a). It can be speculated that one of the two interfaces of as-electroformed Pt/TiO₂/Pt can be activated depending on the first voltage polarity and after the activation the activated interface is responsible for the BRS.¹

From these observations it can be guessed that the set switching is governed by the reverse of the electrochemical reaction leading to the set switching. If an electrochemical reaction occurs under one voltage polarity, the reverse of the reaction is likely to occur under the other polarity. Of course, the reversal of the reaction relies on the equilibrium potential (Nernst potential). If the Nernst potential of the reaction is not zero, the reverse reaction can occur even under the same polarity. Nevertheless, the speculation based on the electrochemical reaction is meaningful in the sense that the applied voltage is able to switch the direction of the reaction.

As dealt with in Chapter 5, electroforming is considered to involve the oxygen vacancy formation reaction. The oxygen vacancies introduced by the electroforming at the interfaces reduce the Schottky barrier height (SBH) so that they have influence on the current-voltage (*I*-*V*) behavior. The formation (annihilation) of oxygen vacancies can take place during the set (reset) switchings, giving rise to the decrease (increase) in the SBH. For the observation of the BRS in Pt/TiO₂/Pt both interfaces are considered to have to be involved in the electroforming. Namely, the oxygen vacancy-induced decrease in the SBH at both interfaces is needed for the activation of the BRS. If one interface is intact, the intact interface will play a dominant role in the current through the switching cell so that the variation of the SBH at the

¹Activated interface means an interface at which the oxygen-related electrochemical reaction takes place.

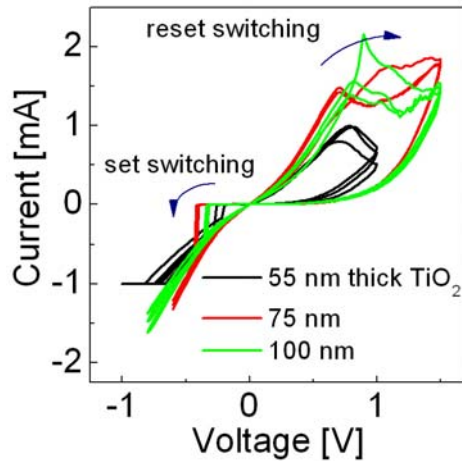


Figure 7.2: TiO_2 thickness dependence of the BRS behavior in $\text{Pt}/\text{TiO}_2/\text{Pt}$ stack switching cells.

other interface is regarded not to remarkably affect the current. If both interfaces are available for the reaction in the as-electroformed state, the following BRS will be in charge of one of the two interfaces relying on the polarity of the first voltage sweep. The BRS in Fig. 7.1(a) is believed to be induced by the interface between TiO_2 and the bottom electrode (BE). Under the first positive voltage sweep some oxygen vacancies at the TiO_2/BE (cathode) interface are annihilated giving rise to the decrease in the SBH at the same interface while additional oxygen vacancies are introduced at the other interface resulting in the further decrease in the SBH. Therefore, the TiO_2/BE interface is in charge of the NDR in Fig. 7.1(a) as well as the following set switching. In case of the first negative voltage sweep, the SBH at the TiO_2/BE interface decreases due to the annihilation of oxygen vacancies at the interface so that the TE/TiO_2 interface is in charge of the NDR as well as the following set switching in Fig. 7.1(b).

TiO_2 thickness dependence of the BRS

To check the TiO_2 thickness dependence of the BRS behavior $\text{Pt}/\text{TiO}_2/\text{Pt}$ stack switching cells with three different TiO_2 thicknesses (50, 75, 100 nm) were prepared. Their BRS behavior was measured by applying a voltage sweep to the TE, starting with positive voltage. Measured BRS curves are shown in Fig. 7.2. It can be noticed that the set and the reset switching voltages are hardly dependent on the thickness of TiO_2 , implying the BRS is given not by a function of the applied electric field, but of the applied voltage. In fact, the applied voltage to TiO_2 with a large amount of space charges ($> 10^{20} \text{ cm}^{-3}$), termed TiO_x , is well screened by the space charges and the electrons within a quite short screening length so that the voltage is applied only in the vicinity of the interfaces. Therefore, under the same applied voltage the voltage distributions in TiO_x with the different thicknesses are similar to each other.

According to the oxygen vacancy-involved electrochemical reaction, the electro-

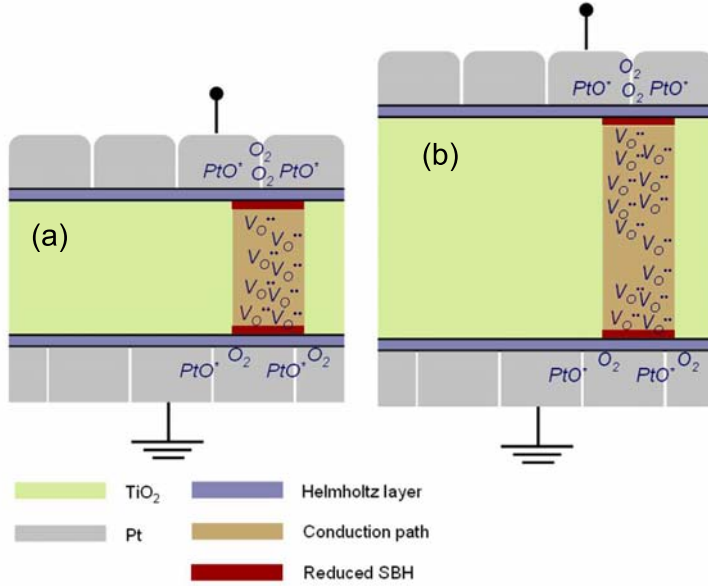


Figure 7.3: Sketches of electroformed Pt/TiO₂/Pt switching cells with different TiO₂ thicknesses.

chemical reaction at the TiO_x/BE interface might be in charge of the BRS behavior in Fig. 7.2. The variation of the SBH at the TiO_x/BE interface determines the resistance state of the switching cells.

7.1.2 Pad-size dependence of the BRS

The BRS measurements were performed on Pt/TiO₂(75 nm)/Pt stack switching cells with two different pad-sizes², 7880 and 49100 μm^2 , whose results are depicted in Fig. 7.4. In Fig. 7.4(a) it can be found that the *I-V* curves in the high resistance state (HRS) of the two different switching cells are almost identical to each other under the whole negative voltage and the positive voltage below 0.6 V. However, the low resistance state (LRS) of the cells are quite different, the larger cell has the higher current than the smaller cell at the same voltage. The current in the LRS might be scaled by the the pad-size. As shown in Fig. 7.4(b), the current densities in the LRS of both cells are quite alike apart from the reset switching region (> 0.66 V) suggesting that the LRS current might be scaled by the cell area. This is not consistent with many literatures reporting the non-scalable resistance of HRS and LRS in different switching systems.[2, 7, 21, 22] However, switching cells with more various pad-sizes should be examined on the pad-size dependence to identify the scalability of the resistance of the LRS.

²As shown in Fig. 2.3, five different pad-sizes were available. However, the pads apart from the smallest one (7880 μm^2) and the second smallest one (49100 μm^2) were shorted in the as-fabricated state.

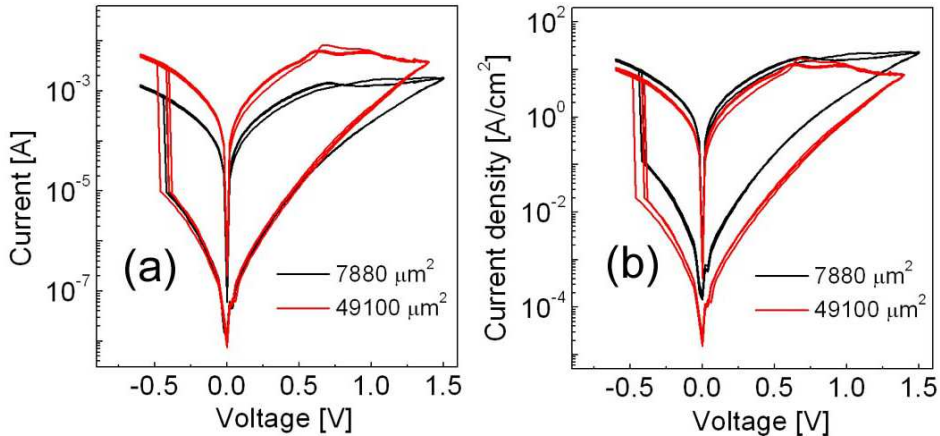


Figure 7.4: BRS curves of Pt/TiO₂(75 nm)/Pt stack switching cells with two different cell areas ($7880 \mu\text{m}^2$ and $49100 \mu\text{m}^2$) plotted on (a) current vs. voltage (b) current density vs. voltage planes.

From the HRS current it can be speculated that the HRS is attributed to be the conduction paths barely undergoing changes in their resistances during the set and the reset switchings, whose number is hardly scaled by the pad-size, and thus numbers of the constant conduction paths in the two different samples are similar. In case of the LRS, the current might be attributed to the additional conduction paths whose areal density is constant in the cells with the different pad-sizes so that the number of the conduction paths in the LRS might be scaled by the area. The resistance of these conduction paths is varied by the set and the reset switchings. The constant and the variable conduction paths are believed to be in parallel connections embedded in the TiO₂ matrix. Therefore, although the resistance of the variable conduction paths increases during the reset switching to be higher than that of the constant conduction paths, the overall resistance of the switching cell is mainly determined by the constant conduction paths so that the HRS does not depend on the pad-size. The schematic of the conduction path distribution in cells with different pad-sizes is depicted in Fig. 7.5.

7.1.3 Abnormal BRS behavior

In case of the voltage-controlled BRS measurements, a voltage sweep range should be properly set for the activation of the electrochemical reaction at only one interface of Pt/TiO₂/Pt. In fact, the formation and the annihilation of oxygen vacancies can take place at both interfaces because the electroforming provides both interfaces with the proper circumstance for the activation of the reaction by introducing a large amount of oxygen vacancies. If the reaction is activated at both interfaces at a certain voltage, one reaction takes place at one interface and the reverse reaction simultaneously takes place at the other interface so that both interfaces can contribute to the changes in the resistance. Therefore, both reset-like and set-like changes in the resistance occur

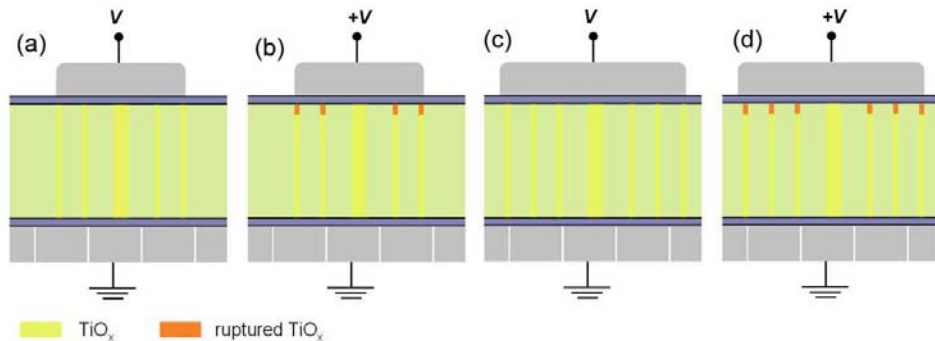


Figure 7.5: Schematic of TiO_x conduction path distribution in the cell with the smaller pad-size in (a) the LRS and (b) the HRS and with the larger pad-size in (c) the LRS and (c) the HRS. The thicker conduction path in the middle of a cell denotes a constant conduction path.

under both voltage polarities, therefore, obvious BRS curves cannot be observed.

Figure 7.6 shows examples of the contribution of both interfaces to the changes in the resistance. The measurements were performed on a Pt/ TiO_2 (55 nm)/Pt stack switching cell by applying continuous four voltage cycles. In Fig. 7.6(a) the resistance first increases at *A* (reset switching) and decreases at *B* (set switching). However, the resistance again increases at *C* showing a reset-like resistance change. The negative maximum of the applied voltage should be between *B* and *C* for stable BRS measurements because as long as the reset-like resistance change at *C* does not occur stable BRS behavior can be measured. The *I*-*V* curve of the second cycle is shown in Fig. 7.6(b) where it is hard to define the resistance state of the hysteretic *I*-*V* curve. First the subtle decrease in the resistance occurs at *D* and the increase in the resistance follows at *E*. On the negative voltage side, the subtle decrease in the resistance occurs at *F* and the increase in the resistance at *G* follows. The *I*-*V* curve of the third cycle was measured by applying a voltage in a wider voltage range ($|V| \leq 1.5$) as shown in Fig. 7.6(c). A more obvious reset-like resistance change takes place at *H* due to the increase in the applied positive maximum voltage and the set-like resistance change at *I* follows the reset-like change. Compared to the subtle set-like change at *F*, the change at *I* is very obvious so that it can be guessed that the change at *I* is attributed to the large resistance increase at *H*. A more obvious reset-like resistance change occurs at *J* also due to the increase in the applied negative maximum voltage. In Fig. 7.6(d) the set-like resistance change at *K* following the change at *J* is found to be obvious as the clear set-like change at *I* follows the clear reset-like change at *H*. Therefore, it can be estimated that the set-like resistance changes at *I* and *K* are the counter changes of the reset-like resistance changes at *H* and *J*, respectively.

The abnormal resistance switching behavior shown in Fig. 7.6 can be explained by taking into account the contribution of both Pt/ TiO_x interfaces to the resistance switching. As shown in Fig. 7.7(a), the switching cell was assumed to consist of two resistors, one at the LE/ TiO_x and the other at the TiO_x /RE (R_1 and R_2). The

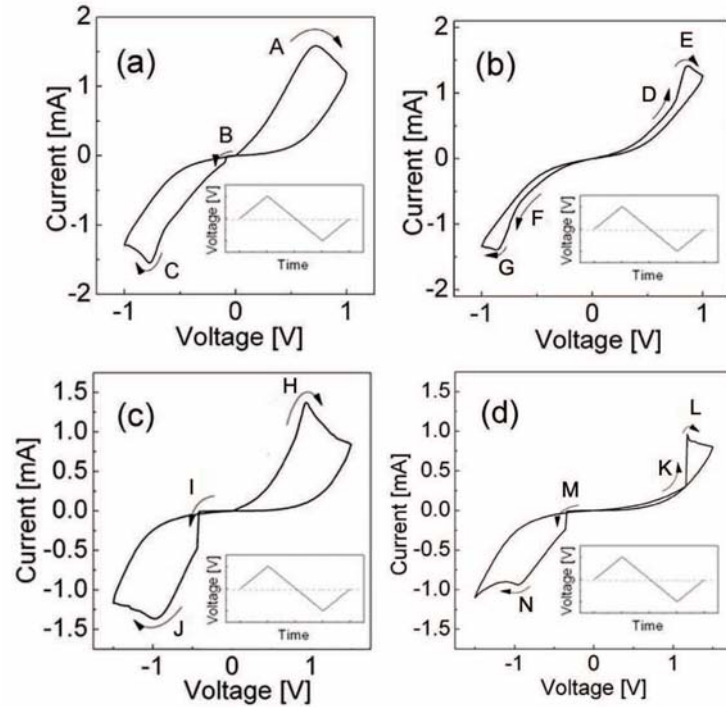


Figure 7.6: I - V curves with four continuous voltage sweeps depicted in the insets.

I - V behavior of this switching cell was simulated. R_1 was assumed to give the I - V behavior shown in Fig. 7.7(a), which is given by a function of the difference in the voltage between at d_1 and 0. This I - V curve is arbitrary so that the voltage and the current in Fig. 7.7(a) would be different from the reality. Since the reaction at the RE/TiO_x interface is the other way than the TiO_x/LE interface reaction, the I - V hysteresis of R_2 is to be antisymmetric to that of R_1 . The voltages in Figs. 7.7(b) and (c) are $V(d_1)$ and $V_{ap} - V(d_1 + d_2)$, respectively. The resistance in TiO_x was assumed to be much smaller than R_1 and R_2 so that no voltage drop in TiO_x was taken into account. The simulation was performed for four different initial resistance states of R_1 and R_2 , (a) LRS (R_1) and LRS (R_2), (b) LRS (R_1) and HRS (R_2), (c) HRS (R_1) and LRS (R_2), (d) and HRS (R_1) and HRS (R_2). The simulation results of the four initial states (a)-(d) are shown in Figs. 7.8(a) to (d), respectively. They are summarized as the following.

- (a) During the first positive voltage sweep R_1 underwent the reset switching while R_2 stayed in the LRS. During the negative voltage sweep R_1 and R_2 underwent the set and the reset switchings, respectively. Therefore, the final states of R_1 and R_2 are the LRS and the HRS, respectively.

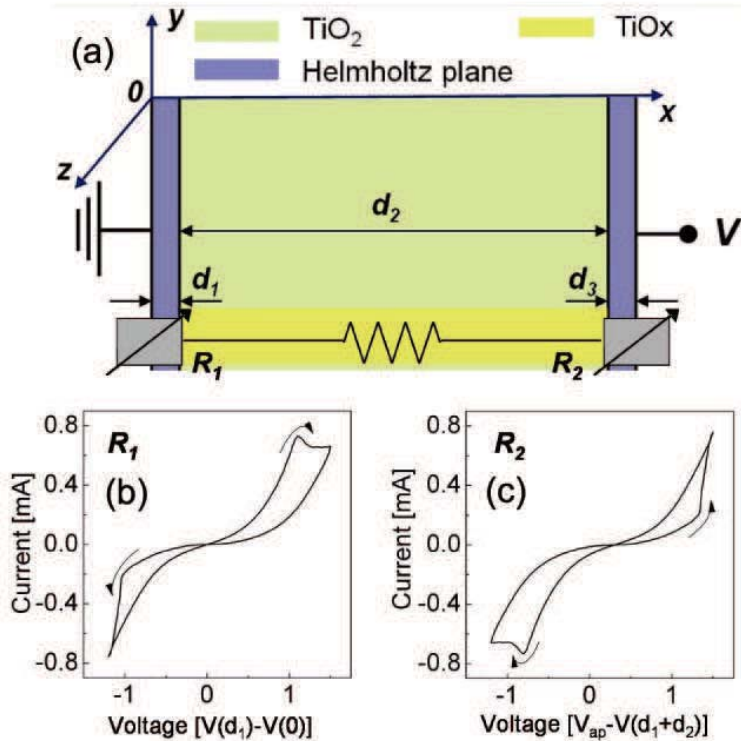


Figure 7.7: (a) Schematic of a Pt/TiO₂/Pt switching cell whose resistance consists of two resistance at two interfaces (R_1 and R_2). The I - V curve assumed to occur at the interface (b) between the left electrode and TiO₂ and (c) between TiO₂ and the right electrode.

(b) During the first positive voltage sweep R_1 and R_2 were switched to the HRS and the LRS, respectively. Then, R_1 and R_2 were switched back to the LRS and the HRS, respectively, during the negative voltage sweep. Therefore, the final states of R_1 and R_2 are the LRS and the HRS, respectively, which are identical to the initial states.

(c) During the first positive voltage sweep both R_1 and R_2 stayed in the initial states, the HRS and the LRS, respectively. Then, R_1 and R_2 underwent the set and the reset switchings, respectively, during the negative voltage sweep. Therefore, the final states of R_1 and R_2 are the LRS and the HRS, respectively.

(d) During the first positive voltage sweep R_2 underwent the set switching while R_1 stayed in the HRS. Then, R_1 and R_2 underwent the set and the reset switchings, respectively, during the negative voltage sweep. Therefore, the final states of R_1 and R_2 are the LRS and the HRS, respectively.

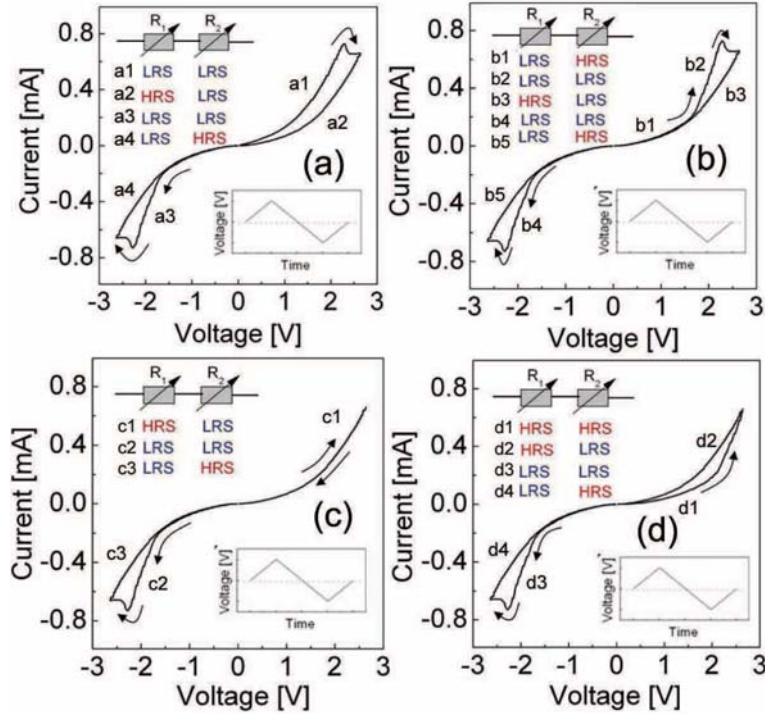


Figure 7.8: Simulated I - V curves for four different initial states of R_1 and R_2 , (a) LRS (R_1) and LRS (R_2), (b) LRS (R_1) and HRS (R_2), (c) HRS (R_1) and LRS (R_2), and (d) HRS (R_1) and HRS (R_2). The insets depict the applied voltage cycle.

By the simulation results the resistance state of R_1 and R_2 in Fig. 7.7 at different voltages can be judged. As mentioned earlier, the I - V curves in Fig. 7.8 were simulated using the arbitrary BRS I - V behavior of R_1 , therefore, they cannot be exactly identical to the experimental data shown in Fig. 7.6. Nevertheless, the tendency of the resistive switching of R_1 and R_2 in Fig. 7.6 can be roughly estimated. The results of the speculation are shown in Fig. 7.9. At A , both R_1 and R_2 are considered to be in the LRS. The resistance change at A is attributed to the reset switching of R_1 . R_2 keeps the LRS because no reset switching of R_2 can take place under the positive voltage. Therefore, the state of R_1 (R_2) at $A2$ is the HRS (LRS). At B the set switching of R_1 occurs so that the state of R_1 (R_2) at $A3$ is the LRS (LRS). At C the reset switching of R_2 occurs while R_1 keeps the LRS because no reset switching of R_1 can occur under the negative voltage so that the state of R_1 (R_2) at $A4$ is the LRS (HRS). The resistance states of R_1 and R_2 at $A1$ to $A4$ are depicted in the inset of Fig. 7.9(a). The I - V curve in Fig. 7.9(a) is comparable to the simulated I - V curve in Fig. 7.8(a).

The initial state of R_1 and R_2 of the second cycle is identical to the last state of the first cycle so that they are the LRS and the HRS, respectively. In the second cycle, R_1 and R_2 undergo a reset-like resistance change at E and a quite subtle set-like change at D , respectively. And under the negative voltage R_1 and R_2 undergo a

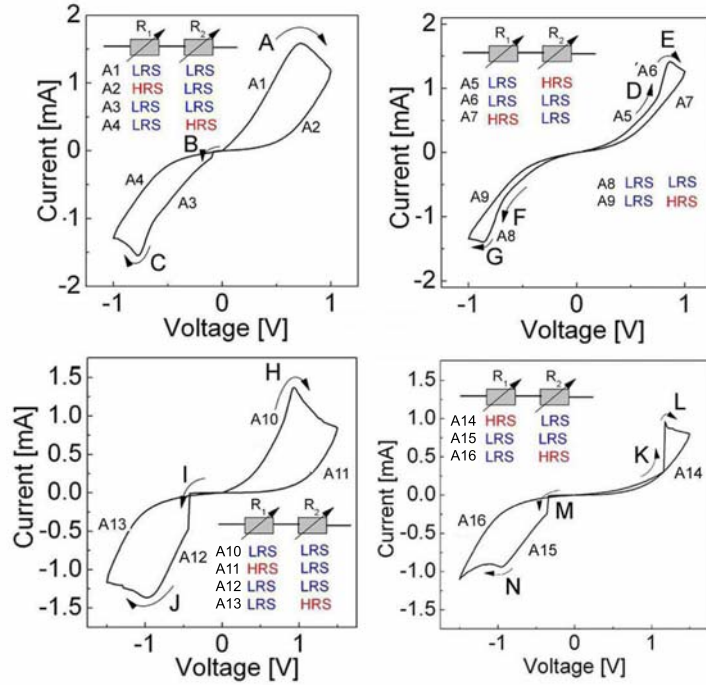


Figure 7.9: Speculated resistance states of R_1 and R_2 of the I - V curves shown in Fig. 7.6. The insets depict the resistance states of R_1 and R_2 at various voltages

subtle set-like change at F and a reset-like change at G , respectively. The I - V curve in Fig. 7.9(b) is comparable to the simulated I - V curve in Fig. 7.8(b).

The initial R_1 and R_2 of the third cycle have in-between resistance states because they did not undergo obvious resistive switching in the second cycle. At H , R_1 undergoes a reset-like resistance change and R_2 a set-like change so that the state of R_1 (R_2) at $A11$ is the HRS (LRS). At I , a set-like change happens to R_1 giving R_1 the LRS and at J , a reset-like change happens to R_2 while R_1 keeps the LRS so that R_1 (R_2) at $A13$ is in the LRS (HRS). The I - V curve in Fig. 7.9(c) is identical to that in Fig. 7.9(a) apart from the initial I - V curve, which is due to the difference of the initial R_1 and R_2 state from those in Fig. 7.9(a).

The initial R_1 and R_2 in the fourth cycle have the LRS and the HRS, respectively. At K R_2 undergoes a set-like change and immediately at L R_1 undergoes a reset-like change, giving R_1 and R_2 the HRS and the LRS, respectively. A set-like change happens to R_1 at M and a reset-like change happens to R_2 at N so that at $A16$ R_1 (R_2) is in the LRS (HRS). From the above discussion on the abnormal BRS behavior the suggested speculation is found to be able to explain the experimental data properly, which involves the contribution of both interfaces to the resistance changes.

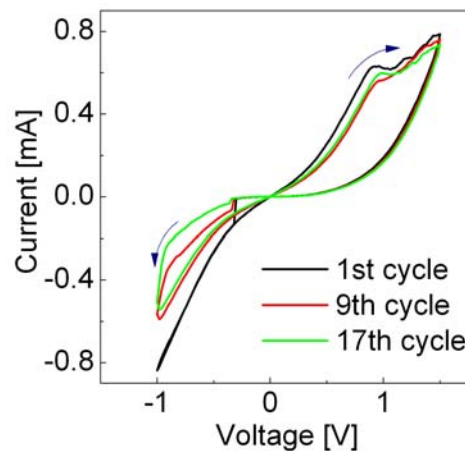


Figure 7.10: BRS curves measured with 17 cycles.

BRS fatigue

As increasing a cycle number, a fatigue of BRS can be observed. Figure 7.10 shows BRS curves measured with 17 cycles. In the first cycle the set switching is quite abrupt at -0.3 V and the reset switching gently starts at about 0.9 V. However, with increasing the cycle number the abrupt set switching becomes less obvious while the gentle set switching at about -1 V becomes more obvious so that the HRS becomes in charge of the gentle set switching. It can be also noticed that the resistance of the LRS decreases with increasing the cycle number. The decrease in the LRS resistance is due to a less decrease in the resistance at the set switching than the set switching in the previous cycle.

7.2 Current-controlled BRS measurements

The current-controlled BRS behavior of Pt/TiO₂/Pt stack switching cells was measured by applying a current sweep. Figure 7.11(a) shows the measured BRS behavior of a Pt/TiO₂(55 nm)/Pt stack switching cell in the air. In Fig. 7.11(a) the reset and the set switchings take place under the positive and the negative current, respectively. The polarity of the set and the reset switching currents is controllable by varying the polarity of the first current sweep after the electroforming, which is similar to the voltage-controlled BRS case. When the first current cycle starting with a negative current sweep is applied to an as-electroformed switching cell, the BRS shows the reset and the set switching under the negative and the positive current, respectively. When the first current cycle starting with a positive current, the set and the reset switching currents are the other way around.

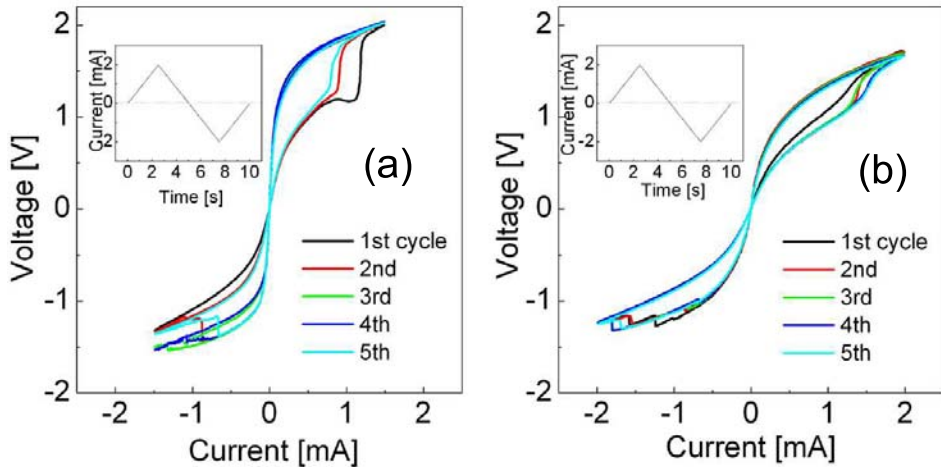


Figure 7.11: Current-controlled BRS behavior of a Pt/TiO₂(55 nm)/Pt stack switching cell measured in (a) the air and (b) vacuum. The inset depicts the applied current cycle.

7.2.1 BRS measurements in vacuum

Current-controlled BRS measurements were performed on a Pt/TiO₂(55 nm)/Pt stack switching cell in a vacuum chamber whose pressure was about 3×10^{-5} Pa. The measured BRS behavior is shown in Fig. 7.11(b). Compared to Fig. 7.11(a), the BRS behavior in vacuum was found to be barely different from that in the air. However, in the statistics it can be noticed that a more stable BRS behavior is observed in vacuum than in the air. Indeed, the measurements in the air once in a while showed unstable BRS behavior, for instance, the abnormal BRS behavior introduced in a previous section. Apart from the enhanced stability the measured BRS behavior in vacuum showed no differences from the BRS in the air.

BRS measurements with elevated oxygen pressure

The external oxygen in the atmosphere perhaps has influence on the BRS because oxygen is believed to be involved in the BRS mechanism. To identify the external oxygen dependence of the BRS, the BRS measurements with different oxygen pressure deserve to be conducted. Current-controlled BRS measurements were performed in a chamber with changing oxygen pressure. Two different BRS modes were activated in vacuum, one shows reset and the set switchings under the applied positive current and the negative current, respectively, (mode A) and the other shows the opposite way to mode A (mode B). As explained in Section 7.1.1, mode A and mode B could be obtained by applying two opposite current cycles to as-electroformed switching cells. Then, pure oxygen gas was injected into the chamber, increasing the pressure. After the pressure became stabilized, the BRS was measured at different pressures.

Figure 7.12 shows that the switching cell formed into mode A stayed in the

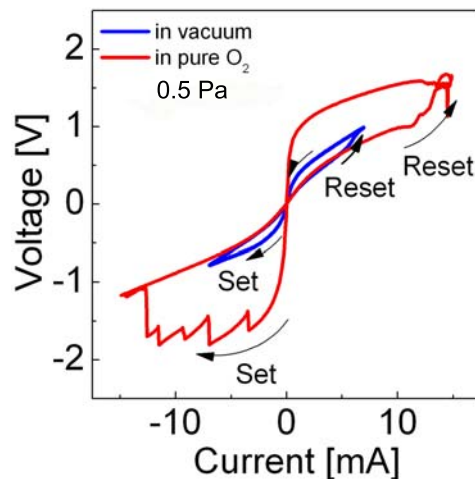


Figure 7.12: Effect of oxygen ambient on a switching curve showing reset and set switching behaviors under positive current and negative current, respectively, in vacuum. The BRS curve in a pressure of 0.5 Pa was measured about 10 min after the BRS measurement in vacuum (blue curve).

same mode when changing the ambient from vacuum to 0.5 Pa pure oxygen gas. However, the ratio of the HRS to the LRS became considerably larger as shown in Fig. 7.12. Many discrete variations of the resistance during the set switching could be also observed at a pressure of 0.5 Pa. Figure 7.13 shows the changes in the BRS curves, initially formed into mode B in vacuum, with increasing oxygen pressure. First, the initial switching curve was measured in vacuum at a pressure of about 3×10^{-5} Pa (see Fig. 7.13(a)). Second, the pressure was increased to 5×10^{-2} Pa by injecting pure oxygen gas, and then a switching measurement with 5 cycles was carried out. The results are shown in Fig. 7.13(b). Third, after some waiting time (~ 180 s) at zero applied voltage another switching measurement with 5 cycles in the same atmosphere was performed. The results are shown in Fig. 7.13(c). Finally, two additional measurements with 5 cycles each were carried out in the oxygen atmosphere at a higher pressure (0.5 Pa). The results are plotted in Figs. 7.13(d) and (e), respectively. Mode B underwent the transition to mode A as the oxygen pressure increased. Therefore, it might be concluded that mode A is the more stable switching mode in a pure oxygen ambient at pressures higher than 0.5 Pa.

Considering the formation and the annihilation reactions of oxygen vacancies at the Pt/TiO₂ interfaces, mode A can be speculated to be controlled by the TiO₂/BE interface. The annihilation and formation of oxygen vacancies at the TiO₂/BE interface are supposed to take place under the applied positive current and the negative current, respectively. Mode B can be speculated to be controlled by the TE/TiO₂ interface only since the formation and annihilation reactions of oxygen vacancies are expected to take place under the applied negative current and the positive current, respectively. However, by increasing oxygen pressure the formation and annihilation of oxygen vacancies at one specific interface, probably the TiO₂/BE interface, might

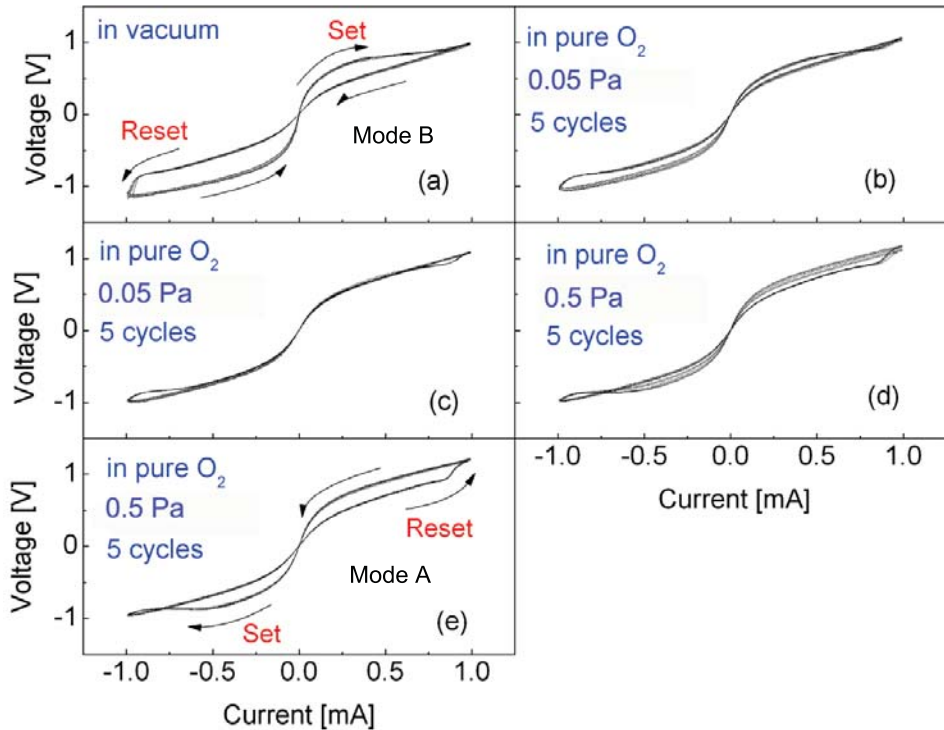


Figure 7.13: Effect of elevated oxygen pressure on a switching curve showing reset and set switching behaviors under negative current and positive current, respectively, in vacuum. The figure shows the transition from mode B to mode A.

become relatively prominent so that the initially different switching modes became the same. The interface changed by the external oxygen ambient is most probably the one at the TE/TiO₂ because it is much easier to be influenced by the ambient atmosphere compared to the TiO₂/BE interface. Therefore, it is guessed that the TE/TiO₂ interface became dull in the applied current range by the external oxygen ambient so that it could be no longer involved in the BRS though the mechanism has to be elaborated in more detail.

7.3 Electrical conduction behavior in the HRS and the LRS

The *I*-*V* characteristics of the HRS and the LRS serve as important clues for the investigation of the BRS mechanism. In this section the conduction behavior of Pt/TiO₂/Pt in a voltage and a time domains is presented.

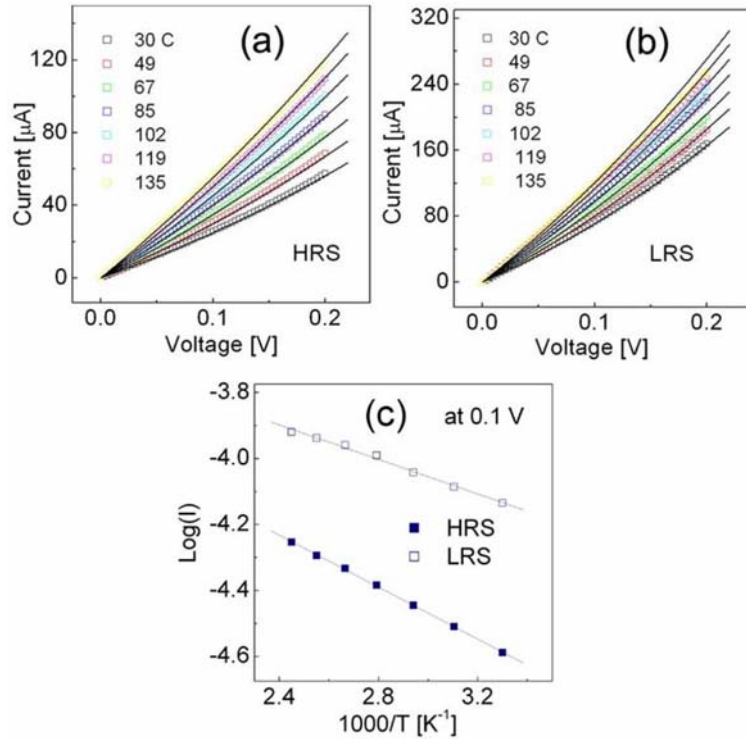


Figure 7.14: I - V behavior at various temperatures in (a) the HRS and (b) the LRS. The solid lines are simulated I - V curves. (c) Temperature dependence of the currents at 0.1 V. The open and full squares denote the HRS and LRS, respectively.

7.3.1 Current-voltage characteristics at various temperatures

The I - V curves in the HRS and the LRS of a Pt/TiO₂(27 nm)/Pt stack switching cell were determined at various temperatures. The maximum of the applied voltage was 0.2 V low enough to prevent any changes in the resistance states of TiO₂. To confirm the temperature dependence of the I - V behavior in the two different states, the changes in the resistance state leading to I - V hysteresis must be avoided.

The I - V curves at various temperatures in the HRS and the LRS are plotted in Figs. 7.14(a) and (b), respectively. And figure 7.14(c) shows the temperature dependence of the currents measured at 0.1 V in the Arrhenius plot, suggesting thermally activated conduction behavior in both HRS and LRS with activation energies of 78.8 meV and 53.7 meV at 0.1 V, respectively. The higher activation energy in the HRS

Table 7.1: Parameters for the I - V curve fitting shown in Fig. 7.14

	$A[A \cdot V^{-1}]$	$E_A[meV]$	$\alpha[eV \cdot V^{-1}]$
HRS	0.0055	83.8	0.0308
LRS	0.00561	58	0.0403

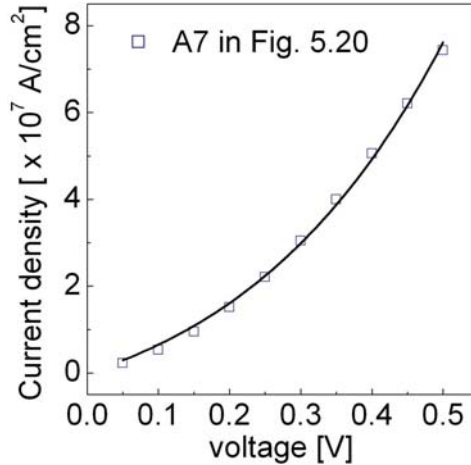


Figure 7.15: Fitting of I - V curve (A7) shown in Fig. 5.21 in Chapter 5 using the conduction equation given by Eq. 7.1

than the LRS is attributed to the higher energy barrier height, probably SBH, in the HRS. The higher SBH consequently leads to the lower current distinguishing the HRS from the LRS. The I - V curves could be nicely fitted using the following equation.

$$I = A V_{ap} \exp \left(\frac{-E_A + \alpha V_{ap}}{k_B T} \right), \quad (7.1)$$

where A , E_A , V_{ap} , and α denote a pre-exponential factor, an activation energy, an applied voltage, and a phenomenological voltage coefficient, respectively. The fitting parameters, A , E_A , and α for both HRS and LRS are shown in Table 7.1. By using the Taylor expansion Eq. 7.1 in a low voltage range can be rewritten by

$$I = A \left(1 - \frac{E_A}{k_B T} \right) V_{ap} + \frac{\alpha A}{k_B T} V_{ap}^2. \quad (7.2)$$

That is, Eq. 7.1 can be expressed as a form of $I = aV + bV^2$ in a low voltage regime. This form has been often used to fit the I - V curves in the BRS of Cr-doped SrZrO₃.^[7, 8] Lee *et al.* have assumed that the linear and the quadratic terms in $I = aV + bV^2$ stand for the Ohmic conduction and the space-charge-limited conduction, respectively, implying that two different conduction behaviors simultaneously take place.^[8] However, this assumption is unlikely to be realistic because the physics behind this assumption has been barely clarified, furthermore, the assumption can not explain the temperature dependence of the I - V behavior. According to Eq. 7.2, the linear and the quadratic terms are nothing but the results of the Taylor expansion of Eq. 7.1 so that they do not stand for the two different conduction mechanisms.

The SBH reduction mechanism suggested in Chapter 5 is likely to explain the I - V behavior properly. As can be seen in Fig. 7.15, the simulated current density-voltage (J - V) curve using the SBH reduction mechanism can well satisfy the I - V form given by Eq. 7.1. A pre-exponential factor of $6.5 \times 10^8 A \cdot V^{-1} \cdot m^{-2}$ was used for the J - V

7.3. ELECTRICAL CONDUCTION BEHAVIOR IN THE HRS AND THE LRS

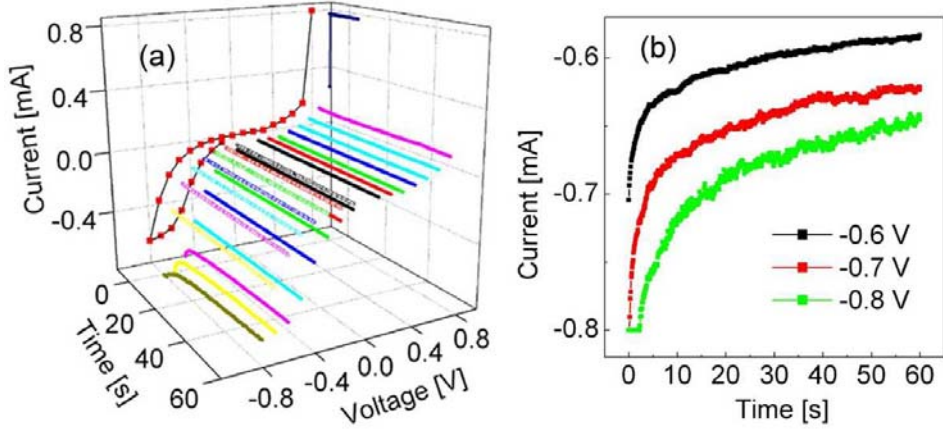


Figure 7.16: (a) I - t curves under applied constant voltages in the range ($|V| \leq 0.8$) in the time domain ($0 - 60$ s). The BRS curve in the current versus voltage plane is measured with a delay time of 60 s. The I - t curves in the LRS under the positive voltage are omitted for a better view of the I - V - t curves. (b) I - t curves in the reset switching region in the left figure.

curve fitting because the pre-exponential factor is equal to A divided by the total area of the conduction paths. E_A and α were set to be 65 meV and $0.055 \text{ eV} \cdot \text{V}^{-1}$, respectively.

Concerning other conduction mechanisms, Greene *et al.* and Dearnaley *et al.* have regarded chains consisting of cations and anion vacancies as the conduction paths of switching materials.[60, 61] They have considered that electrons are transferred along the conduction chains by quantum mechanical tunneling or electron hopping.[60, 61] However, these electron transfer mechanisms are unlikely to explain the electric conduction behavior in the HRS and the LRS of TiO_2 . In the electron tunneling mechanism, the tunneling current must show very weak temperature dependence because the tunneling coefficient is nearly independent of temperature. The I - V behaviors in both HRS and LRS in TiO_2 show thermally activated behavior with an activation energy of a few tens of meV so that the electron tunneling can hardly explain the conduction behavior. According to the electron hopping mechanism, electron hopping is expected to be observed in the insulator whose localized energy states are formed at the deep level in the band gap. Localized energy states in TiO_2 can be introduced by oxygen vacancies or Ti interstitials. However, it has been found that the oxygen vacancies or the Ti interstitials introduce very shallow energy states from the conduction band edge so that these defects can be easily ionized even at room temperature. Therefore, band conduction must be favorable rather than electron hopping.

7.3.2 Current-time characteristics at various constant voltages

Current-voltage-time (I - V - t) curves were measured by applying various constant voltages to a Pt/TiO₂(27 nm)/Pt stack switching cell. The applied constant voltages were in the range ($|V| \leq 0.8$) and the current was measured in the time domain (0 – 60 s). The results are plotted in Fig. 7.16. In Fig. 7.16 the I - t behavior in the reset switching region is obviously distinguished from that in the non-switching region. The I - t curves in the reset switching region show quite strong dispersive behavior, the decrease in the current with respect to time, while those in the non-switching region show very weak dispersive behavior. The I - t dispersion in the set switching region could be barely observed because the set switching time was so short that only the abrupt current jump at the beginning of the voltage application could be noticed.

The dispersive I - t behavior implies that the system is in a non-steady state. The dispersion can be interpreted based on the sluggish migration and the reaction of oxygen vacancies. The oxygen vacancy-induced SBH variation involves the oxygen diffusion in Pt and oxygen vacancy diffusion in TiO_x. Considering the low diffusivity of the oxygen ions and the oxygen vacancies, it can be expected that it will take a while for the system to reach the steady state so that the I - t dispersion is a matter of course. However, the electrons are expected to be in a quasi-static state at every moment, staying in the local equilibrium in the time domain. The electrons can very fast react to the variation of the electrostatic potential, which is attributed to the ion migration, so that they can very soon reach the local equilibrium. No dispersion in the non-switching region implies that no SBH variation takes place in the non-switching region.

7.4 Transition to unipolar resistive switching characteristics

Increasing compliance current gives rise to the transition from BRS to unipolar resistive switching (URS) as demonstrated in Fig. 7.17. First, the BRS was activated in a Pt/TiO₂(27 nm)/Pt stack switching cell by applying a voltage. The BRS could be observed with a compliance current of 1 mA. Afterwards, several continuous voltage sweeps from +3 V to -3 V (R → L) and back to +3 V (L → R) were applied with setting a compliance current of 3 mA. Finally, the transition resulted in a linear I-V behavior corresponding to the LRS of the URS. After this transition, stable URS behavior was observed. However, the reverse transition could be hardly observed. The HRS of the URS was very easily switched to the LRS of the URS even with a low compliance current instead of being changed to the BRS mode. Therefore, it can be concluded that once the URS mode is activated, the reverse transition, i.e. from the URS to the BRS, is hardly observable.

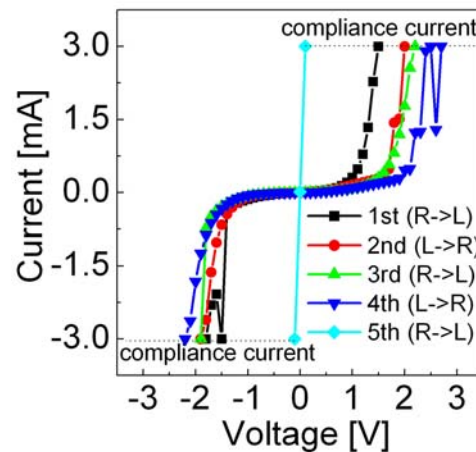


Figure 7.17: Transition from BRS to URS by applying voltage sweeps with a current compliance of 3 mA. $R \rightarrow L$ and $L \rightarrow R$ indicate the voltage sweeps from +3 V to -3 V and from -3 V to +3 V, respectively.

7.5 Modeling of the BRS behavior

By the experimental observations introduced in the previous sections, the BRS in $\text{Pt}/\text{TiO}_2/\text{Pt}$ can be judged to be attributed to the oxygen-involved electrochemical reaction occurring at the Pt/TiO_x interfaces. The electrochemical reaction leads to the formation and annihilation of oxygen vacancies at the interfaces. By taking into account the role of the Helmholtz layer in the electrochemical reaction, a reaction rate constant k can be given by a function of the applied voltage so that the flux of the oxygen ions/vacancies, taking part in the reaction, as a function of the applied voltage can be determined. Regarding the $\text{Pt}/\text{TiO}_x/\text{Pt}$ junction as a one-dimensional system, the distribution of the oxygen vacancies in TiO_x and its variation with respect to time can be obtained by solving the time-dependent one-dimensional drift-diffusion equation of the oxygen vacancies and the electrons using the finite difference method. The determined flux of the oxygen ions at the two interfaces, given by a form of the Butler-Volmer equation, and the flux of the electrons transferring through the interfaces serve as the boundary conditions of the time-dependent drift-diffusion equations. As a solution of the drift-diffusion equations, the I - V curve of the $\text{Pt}/\text{TiO}_x/\text{Pt}$ junction can be obtained.

7.5.1 Electrochemical reaction through the Helmholtz layer

The Helmholtz layer is supposed to be formed at the Pt/TiO_x interfaces due to the separation of two oppositely charged layers, one is on the Pt side and the other is on the TiO_x side at the interface.[49] In Chapter 5 electroforming was found to give rise to the incorporation of oxygen ions into the Pt electrode in $\text{Pt}/\text{TiO}_2/\text{Pt}$ switching cells. It is known that the oxygen ions in metal are negatively charged rather than neutral[73] so that they can participate in the voltage-controlled electrochemical

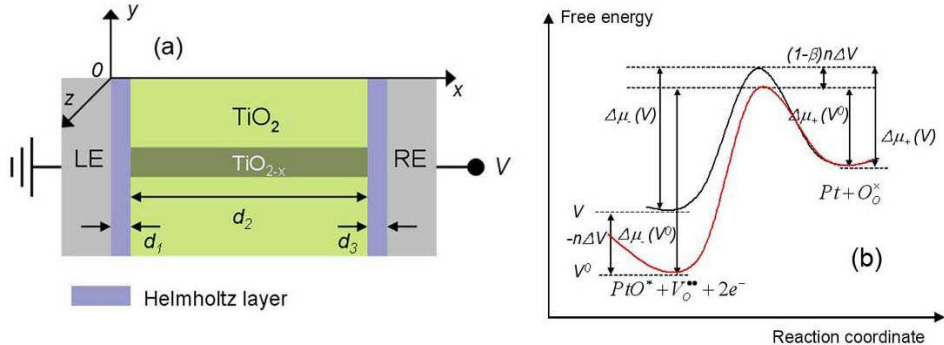
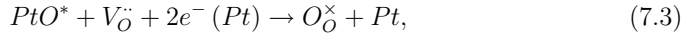


Figure 7.18: (a) Configuration of a Pt/TiO₂/Pt switching cell. (b) A free energy diagram of Eq. 7.3 with respect to the reaction coordinate.

reaction of the formation and annihilation of oxygen vacancies at Pt/TiO_x interface. In this study the oxygen ions are assumed to have a charge of -2 in Pt. The oxygen vacancy annihilation reaction can be given by



where PtO^* denotes a chemisorbed oxygen at grain boundaries of Pt and $e^- (Pt)$ means a free electron in Pt. The reverse of Eq. 7.3 indicates the oxygen vacancy formation reaction.

Figure 7.18(a) depicts the configuration of a Pt/TiO₂/Pt switching cell. The reaction in Eq. 7.3 will be dealt with at the two interfaces between the left electrode (LE) and TiO_x and between TiO_x and the right electrode (RE). The free energy diagram of the reaction is depicted in Fig. 7.18(b). The meaning of the symbols in Fig. 7.18(b) is given in Table 7.2. An amount of the electric energy of ions at a Pt/TiO_x interface relies on the applied voltage. Since the cations and the anions are separated by the Helmholtz layer, the whole electric energy of all ions is not constant so that the applied voltage can vary the energy barrier for the reaction of the oxygen vacancy annihilation depicted in Fig. 7.18(b).

The sum of the free energy of the right side of Eq. 7.3 as well as the energy barrier height varies relying on the applied voltage as shown in Fig. 7.18(b), leading to the reaction rate constant of the forward and the reverse reactions (k_- and k_+) of Eq. 7.3. The formation free energy per O_O^x of Eq. 7.3 is expressed as

$$\Delta\mu = \Delta\mu^0 + k_B T \ln \frac{\bar{c}_{O_O^x} \bar{c}_{Pt}}{\bar{c}_{PtO^*} \bar{c}_V \bar{c}_e^2}, \quad (7.4)$$

where

$$\Delta\mu^0 = \mu_{O_O^x}^0 + \mu_{Pt} - \mu_{PtO^*}^0 - \mu_V^0 - 2\mu_e^0 = \Delta h - T\Delta s. \quad (7.5)$$

μ_i^0 , where $i \in \{O_O^x, Pt, PtO^*, V, e\}$ denotes the standard chemical potentials of O_O^x , Pt, PtO^{*}, $V_O^{\cdot\cdot}$, and an electron, respectively, \bar{c}_i , where $i \in \{O_O^x, Pt, PtO^*, V, e\}$ is the ratio of concentration c_i to the concentration in the standard state³ c_i^0 , c_i/c_i^0 . c_{PtO^*}

³The standard state means a pure state

can be replaced by $c_{O^{2-}}$ because one chemisorbed oxygen ion per one Pt atom is assumed in Eq. 7.3 and \bar{c}_{Pt} and \bar{c}_e are almost unity. $c_{O_O^X}^0$ is equal to c_V^0 . Therefore, the ratio $\bar{c}_{O_O^X} \bar{c}_{Pt} / \bar{c}_{PtO^*} \bar{c}_V \bar{c}_e^2$ can be rewritten by

$$\frac{\bar{c}_{O_O^X} \bar{c}_{Pt}}{\bar{c}_{PtO^*} \bar{c}_V \bar{c}_e^2} = \frac{c_{PtO^*}^0 (c_{O_O^X}^0 - c_V)}{c_{PtO^*} c_V}. \quad (7.6)$$

Consequently, the Nernst potential V_n of Eq. 7.3 is given by

$$V_n = \frac{1}{n} (\Delta h - T \Delta s + k_B T \ln c_{PtO^*}^0) + \frac{k_B T}{n} \ln \frac{c_{O_O^X}^0 - c_V}{c_{PtO^*} c_V}. \quad (7.7)$$

Concerning the kinetics of Eq. 7.3, the variation of the energy barrier height depicted in Fig. 7.18(b) relying on the applied voltage can be explained by the following. The energy barrier per O for the reverse reaction of Eq. 7.3 with a voltage of $V(d_1)$ is written by $\mu_+ [V(d_1)]$. The difference in the energy barrier height for the reverse reaction at two different voltages at d_1 , $V(d_1)$ and $V^0(d_1)$, can be expressed as

$$\Delta \mu_+ [V(d_1)] - \Delta \mu_+ [V^0(d_1)] = -(1 - \beta) n \Delta V, \quad (7.8)$$

where ΔV is equal to $V(d_1) - V^0(d_1)$. In the same way, the difference in the energy barrier height for the forward reaction at two different voltages at d_1 , $V(x = d_1)$ and $V^0(x = d_1)$, can be expressed as

$$\Delta \mu_- [V(d_1)] - \Delta \mu_- [V^0(d_1)] = \beta n \Delta V. \quad (7.9)$$

Therefore, the flux equation of O undergoing the forward and the reverse reactions at the LE/TiO_x interface (J_{-L}^O and J_{+L}^O) can be described by

$$J_{-L}^O = k_- c_{PtO^*} c_V \exp \left(\frac{-\beta n \Delta V}{k_B T} \right), \quad (7.10)$$

and

$$J_{+L}^O = k_+ c_{O_O^X} \exp \left[\frac{(1 - \beta) n \Delta V}{k_B T} \right], \quad (7.11)$$

respectively. c_e does not depend on the applied voltage so that c_e is included in k_- in Eq. 7.10. The overall flux equation of O (J_L^O) is the summation of Eq. 7.10 and 7.11.

$$J_L^O = k_- c_{PtO^*} c_V \exp \left(\frac{-\beta n \Delta V}{k_B T} \right) - k_+ c_{O_O^X} \exp \left[\frac{(1 - \beta) n \Delta V}{k_B T} \right]. \quad (7.12)$$

By taking $V^0(d_1)$ as a reference voltage 0 and using k_-^0 and k_+^0 , the forward and the reverse reaction rate constants at the reference voltage V^0 , Eq. 7.12 can be rewritten by

$$J_L^O = k_-^0 c_{PtO^*} c_V \exp \left[\frac{-\beta n V(d_1)}{k_B T} \right] - k_+^0 c_{O_O^X} \exp \left[\frac{(1 - \beta) n V(d_1)}{k_B T} \right]. \quad (7.13)$$

In equilibrium, J_{-L}^O is equal to J_{+L}^O so that the net flux J_L^O is zero. The voltage at d_1 in equilibrium is defined as the Nernst potential V_n . V_n can be therefore given by

$$V_n = \frac{k_B T}{n} \ln \frac{k_+^0}{k_-^0} + \frac{k_B T}{n} \ln \frac{c_{O_2^{\times}}}{c_{PtO^*} c_V}. \quad (7.14)$$

Comparing Eq. 7.14 with Eq. 7.7 gives the ratio k_+^0/k_-^0 as

$$\frac{k_+^0}{k_-^0} = c_{PtO^*}^0 \exp \left(\frac{-\Delta s}{k_B} \right) \exp \left(\frac{\Delta h}{k_B T} \right). \quad (7.15)$$

The flux equation of the forward/reverse reaction at V_n , J^0 can be obtained by entering Eq. 7.15 into Eq. 7.13, giving the equation,⁴

$$J^0 = k_-^0 \left(\frac{k_+^0}{k_-^0} \right)^\beta \frac{c_{O_2^{\times}}^\beta}{(c_{PtO^*} c_V)^{\beta-1}}. \quad (7.16)$$

Therefore, the net flux equation of O can be written by a form of the Butler-Volmer equation,

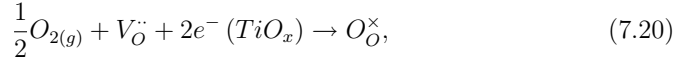
$$J_L^O = J^0 \left\{ 1 - \exp \left\{ \frac{n[V(d_1) + V_n]}{k_B T} \right\} \right\} \exp \left\{ \frac{-\beta n[V(d_1) - V_n]}{k_B T} \right\}. \quad (7.17)$$

For the right Helmholtz layer at the TiO_2/RE interface oxygen ion flux equation J_R^O can be derived using the same derivation procedure as used for the J_L^O derivation. J_R^O is given by

$$J_R^O = J^0 \left\{ 1 - \exp \left\{ -\frac{n[V_{ap} - V(d_1 + d_2) - V_n]}{k_B T} \right\} \right\} \exp \left\{ \frac{\beta n[V_{ap} - V(d_1 + d_2) - V_n]}{k_B T} \right\}. \quad (7.18)$$

Eqs. 7.17 and 7.18 will serve as the boundary conditions for the calculation of the time-dependent distribution of oxygen vacancies.

Concerning the formation free energy of Eq. 7.3, the reaction can be divided into three reactions.



and



The above reactions occur at a Pt/TiO_x interface so that the free electrons in Pt should be distinguished from those in TiO_x due to the difference of the work functions of Pt and TiO_x . The first principle study on the oxygen chemisorption on Pt surface has shown that the formation energy of the oxygen chemisorption per oxygen atom is -1.57 eV.[69] Therefore, the change in the energy of Eq. 7.19 is considered to be 1.57

⁴As mentioned earlier, J_{-L}^O is equal to J_{+L}^O at V_n

⁵One oxygen atom per Pt atom is assumed to form chemisorption.

eV. The free energy change of Eq. 7.20 in TiO_2 has been frequently evaluated by measuring the conductivity change with respect to temperature.[40–43] Balachandran *et al.* have evaluated the energy change of Eq. 7.20 in non-stoichiometric TiO_{2-x} , which is about -2.1 eV.[42] The change in the energy of Eq. 7.21 can be determined from the work function difference between Pt and TiO_x . As shown in Fig. 5.23 in Chapter 5, the electroformed TiO_2 is believed to have the Fermi energy slightly above the conduction band minimum. Therefore, the work function difference is approximately $\phi_m - \chi_{\text{TiO}_x}$, where ϕ_m and χ_{TiO_x} are the work function of Pt and the electron affinity of TiO_x . The change in the energy of Eq. 7.21 is $\chi_{\text{TiO}_x} - \phi_m$.⁶ χ_{TiO_x} is an unknown value so that it was assumed to be 0.5 eV in Chapter 5. With the assumed energy change of Eq. 7.21 the formation energy of Eq. 7.3 (h) can be determined to be about 0.47 eV. However, in the BRS simulation a formation energy of 0.75 eV will be used for a better simulation result. The dependence of the BRS on the formation energy will be explained later.

7.5.2 Drift-diffusion of oxygen vacancies and electrons in TiO_x

TiO_x is believed to be n-type semiconductor because the electroforming is expected to introduce a large amount of oxygen vacancies in TiO_x , serving as donors. Electrons and oxygen vacancies are therefore regarded as the majority charged particles in TiO_x . The one-dimensional time-dependent distribution of the oxygen vacancies and the electrons can be determined by solving the one-dimensional drift-diffusion equation, given by

$$J_{DD}^i = z_i c_i \mu_i E - D_i \frac{\partial c_i}{\partial x}, i \in \{e, V\}, \quad (7.22)$$

where z_i , μ_i , and D_i mean the ionization number, the mobility, and the diffusivity of particle i , respectively. Eq. 7.22 describes the flux of charged particle i due to drift and diffusion, whose driving forces are the internal electric field E and the concentration gradient, respectively. The first and the second terms on the right side of Eq. 7.22 denote the drift and the diffusion contributions, respectively. Fick's 2nd law is expressed as

$$\frac{\partial c_i}{\partial t} = -\frac{\partial J_{DD}^i}{\partial x}. \quad (7.23)$$

Entering Eq. 7.22 into Eq. 7.23 gives the following equation.

$$\frac{\partial c_i}{\partial t} = -z_i c_i \mu_i \frac{\partial E}{\partial x} - z_i \mu_i E \frac{\partial c_i}{\partial x} + D_i \frac{\partial^2 c_i}{\partial x^2}, \quad (7.24)$$

where D_i is not regarded as a function of coordinate x . E can be obtained by solving the Poisson equation. In order to obtain the solution of the Poisson equation, the time-dependent distribution of both electrons and oxygen vacancies must be defined first. It turns out that to solve Eq. 7.24 is hardly possible using an analytical calculation because of the presence of E . If E is constant in TiO_x , Eq. 7.24 can be analytically solved, giving the error function.[72] However, E cannot be constant because of the space charges in TiO_x so that the finite difference method will be

⁶In Chapter 5 $\phi_m - \chi_{\text{TiO}_x}$ was defined as ϕ_b

Table 7.2: List of symbols

Symbol	Description
$\mu_{O_O^X}$	Chemical potential of O^{2-} at an oxygen site in TiO_x
μ_O	Chemical potential of O^{2-} in Pt
μ_V	Chemical potential of V_O^{\cdot}
$c_{O_O^X}$	Concentration of O_O^X
c_{PtO^*}	Concentration of PtO^*
c_V	Concentration of V_O^{\cdot}
$\mu_{O_O^X}^0$	Chemical potential of O^{2-} at an oxygen site in the standard state
$\mu_{PtO^*}^0$	Chemical potential of PtO^* in the standard state
μ_V^0	Chemical potential of V_O^{\cdot} in the standard state
$c_{O_O^X}^0$	Concentration of O_O^X in the standard state
$c_{PtO^*}^0$	Concentration of PtO^* in the standard state
c_V^0	Concentration of V_O^{\cdot} in the standard state
$\bar{c}_{O_O^X}$	Ratio of the concentration of O_O^X to that in the standard state
\bar{c}_{PtO^*}	Ratio of the concentration of PtO^* to that in the standard state
\bar{c}_V	Ratio of the concentration of V_O^{\cdot} to that in the standard state
V^0	Reference voltage at $x = d_1$
h	Enthalpy per particle
s	Entropy per particle
$\Delta\mu_-(V)$	Energy barrier for a forward reaction at a given voltage V
$\Delta\mu_+(V)$	Energy barrier for a reverse reaction at a given voltage V
β	Asymmetry factor
V_n	Nernst potential of a reaction
n	Ionization number of O^{2-}
k_-	Reaction rate of a forward reaction at a give voltage V
k_+	Reaction rate of a reverse reaction at a give voltage V
k_-^0	Reaction rate of a forward reaction at a reference voltage V^0
k_+^0	Reaction rate of a reverse reaction at a reference voltage V^0

applied to the calculation of the time-dependent distribution of the electrons and the oxygen vacancies, which will be explained in the next section.

Proper boundary conditions are necessary to solve Eq. 7.24. For the calculation of the oxygen vacancy distribution the flux of the oxygen vacancies at the LE/ TiO_x and the TiO_x /RE interfaces (J_L^V and J_R^V) serve as the boundary conditions. Since J^V is equal to $-J^O$, the negative of Eqs. 7.17 and 7.18 can be taken as the boundary conditions. For the calculation of the electron distribution the electronic current densities at the LE/ TiO_x and the TiO_x /RE interfaces (J_L^e and J_R^e) are used as the boundary conditions. Concerning J_L^e , the electron transfers, LE \rightarrow TiO_x and $TiO_x \rightarrow$ LE, contribute to J_{LT}^e and J_{TL}^e , respectively. J_{LT}^e can be expressed in terms of the Shottky barrier height (SBH) at the LE/ TiO_x (ϕ_b^L) using the Landauer-Büttiker formalism[70] as

$$J_{LT}^e = \frac{q\hbar}{4\pi^3 m_e} \int_{-\infty}^{\infty} \int_{-\infty}^{\infty} \int_{\sqrt{2m_e\phi_b^L}/\hbar}^{\infty} k_x f(\epsilon) dk_x dk_y dk_z, \quad (7.25)$$

where m_e , k_x , k_y , and k_z denote the effective mass of an electron, the wave vectors of an electron in the directions x , y , and z , respectively. And $f(\epsilon)$ denotes the Fermi-Dirac distribution function. The following equation can be substituted for Eq. 7.25 for a simper calculation.

$$J_{LT}^e = qA \int_{\epsilon_c(d_1)}^{\infty} \frac{N'_c \sqrt{\epsilon}}{1 + \exp\left(\frac{\epsilon - \epsilon_{Fm}}{k_B T}\right)} d\epsilon, \quad (7.26)$$

where N'_c is given by $\sqrt{2m_e^{3/2}} / (\hbar^3 \pi^2)$. A , $\epsilon_c(d_1)$, $\epsilon_c(d)$, and ϵ_{Fm} denote the velocity of the electron transfer, the conduction band edge at d_1 , and the Fermi energy of the LE, respectively. The detail of Eqs. 7.25 and 7.26 was explained in Chapter 5. In a similar way, J_{TL}^e is given by a function similar to Eq. 7.26.

$$J_{TL}^e = qv_{TL} \int_{\epsilon_c(d_1)}^{\infty} \frac{N'_c \sqrt{\epsilon - \epsilon_c(d_1)}}{1 + \exp\left[\frac{\epsilon - \epsilon_F(d_1)}{k_B T}\right]} d\epsilon, \quad (7.27)$$

where $\epsilon_F(d_1)$ and v_{TL} mean the Fermi energy at d_1 and the velocity of the electron transfer $\text{TiO}_x \rightarrow \text{LE}$, respectively. By putting together Eqs. 7.26 and 7.27 J_L^e can be written by

$$J_L^e = -qAN'_c \int_{\epsilon_c(d_1)}^{\infty} \frac{\sqrt{\epsilon}}{1 + \exp\left(\frac{\epsilon - \epsilon_{Fm}}{k_B T}\right)} d\epsilon + qv_{TL}N'_c \int_{\epsilon_c(d_1)}^{\infty} \frac{\sqrt{\epsilon - \epsilon_c(d_1)}}{1 + \exp\left[\frac{\epsilon - \epsilon_F(d_1)}{k_B T}\right]} d\epsilon. \quad (7.28)$$

Concerning J_R^e , the electron transfers, $\text{RE} \rightarrow \text{TiO}_x$ and $\text{TiO}_x \rightarrow \text{RE}$, contribute to J_{RT}^e and J_{TR}^e , respectively. Using the same procedure used for the derivation of J_L^e , J_R^e can be obtained as

$$J_R^e = -qv_{TR}N'_c \int_{\epsilon_c(d_1+d_2)}^{\infty} \frac{\sqrt{\epsilon - \epsilon_c(d_1+d_2)}}{1 + \exp\left[\frac{\epsilon - \epsilon_F(d_1+d_2)}{k_B T}\right]} d\epsilon + qAN'_c \int_{\epsilon_c(d_1+d_2)}^{\infty} \frac{\sqrt{\epsilon}}{1 + \exp\left(\frac{\epsilon - \epsilon_{Fm} - qV_{ap}}{k_B T}\right)} d\epsilon, \quad (7.29)$$

where v_{TR} means the velocity of the electron transfer $\text{TiO}_x \rightarrow \text{RE}$. $\epsilon_c(d_1+d_2)$ and $\epsilon_F(d_1+d_2)$ denote the conduction band edge and the Fermi energy at $d_1 + d_2$, respectively.

7.5.3 Finite difference method for the calculation

There are three available finite difference methods (FDMs), the explicit, the implicit, and the Crank-Nicolson methods. In the explicit method the information at time t is obtained from that at time $t - \Delta t$. Using the explicit method Fick's 2nd law in one dimension, $\partial c / \partial t = -\partial J / \partial x$ can be described as

$$\frac{c_{t,x}^i - c_{t-\Delta t,x}^i}{\Delta t} = \frac{D_i}{(\Delta x)^2} (c_{t-\Delta t,x+\Delta x}^i - 2c_{t-\Delta t,x}^i + c_{t-\Delta t,x-\Delta x}^i), \quad (7.30)$$

where $c_{t,x}^i$ denotes the concentration of particle i at time t and spatial point x (t, x) and D_i denotes the diffusivity of particle i . If all c^i along the coordinate x at time

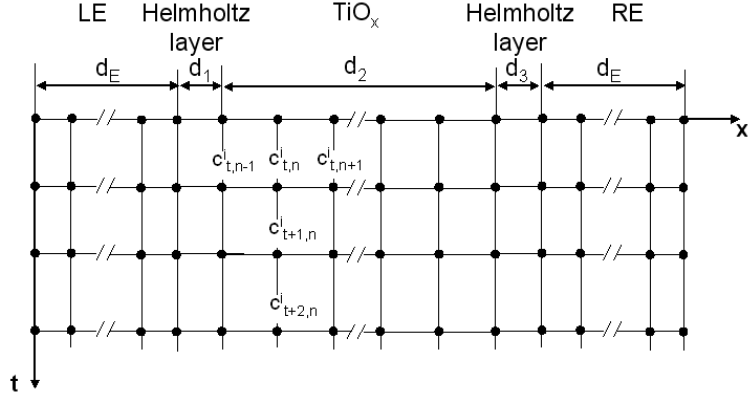


Figure 7.19: Configuration of the nodes of Pt/TiO_x/Pt in two dimensions, time t and coordinate x .

$t - \Delta t$ are known, c^i at time t can be calculated. For the explicit method to be stable and convergent D_i , Δt , and Δx should satisfy the condition, $D_i \Delta t / (\Delta x)^2 \leq 1/2$. In the implicit method, c^i at time t is obtained from c^i at time $t - \Delta t$ as well as t itself. In this method, Fick's 2nd law can be described as

$$\frac{c_{t,x}^i - c_{t-\Delta t,x}^i}{\Delta t} = \frac{D_i}{(\Delta x)^2} (c_{t,x+\Delta x}^i - 2c_{t,x}^i + c_{t,x-\Delta x}^i). \quad (7.31)$$

Since c^i at t is determined by c^i at $t - \Delta t$ as well as t , an iterative method is needed to obtain c^i at t . The implicit method is therefore more complicated than the explicit method. This method is always convergent regardless of Δt and Δx . However, the errors are linear over Δt and quadratic over Δx .^[74] In the Crank-Nicolson method, the concentrations at t and $t - \Delta t$ equally contribute to the determination of c^i at t . Fick's 2nd law can be described using the Crank-Nicolson method as

$$\frac{c_{t,x}^i - c_{t-\Delta t,x}^i}{\Delta t} = \frac{D_i}{2(\Delta x)^2} [(c_{t,x+\Delta x}^i - 2c_{t,x}^i + c_{t,x-\Delta x}^i) + (c_{t-\Delta x+\Delta x}^i - 2c_{t-\Delta t,x}^i + c_{t-\Delta t,x-\Delta x}^i)]. \quad (7.32)$$

This method is always convergent and the errors are quadratic over Δt and of the fourth degree over Δx .^[74]

The explicit FDM was chosen for the calculation of the drift-diffusion of the oxygen vacancies and the electrons in TiO_x and the formation and the annihilation reactions of the oxygen vacancies at the Helmholtz layer.

Calculation of the voltage and the electron distributions at a given time

The configuration of the nodes in Pt/TiO_x/Pt is depicted in Fig. 7.19. Along the spatial coordinate x N_E nodes are assigned to the LE, N_2 nodes TiO_x, and also N_E nodes the RE. d_E , d_1 , d_2 , and d_3 are the thicknesses of the LE/RE, the left Helmholtz layer, TiO_x, and the right Helmholtz layer, respectively. Therefore, the distance between neighboring nodes in the LE/RE is $d_E / (N_E - 1)$ and that in TiO_x

is $d_2/(N_2 - 1)$. Along time axis t N_t nodes are located with a distance between neighboring nodes of Δt . Let us start dealing with the drift-diffusion of the oxygen ions in the LE. Using the configuration of the nodes, Fick's 2nd law of the oxygen ions can be described as

$$\frac{c_{t+1,n}^{O(L)} - c_{t,n}^{O(L)}}{\Delta t} = \frac{N_1 - 1}{d_E} \left(J_{t,n-1/2}^{O(L)} - J_{t,n+1/2}^{O(L)} \right), \quad (7.33)$$

where $c_{t,n}^{O(L)}$ denotes the concentration of the oxygen ions at node (t, n) in the LE. Since an electric field is barely present in metal, the drift of the oxygen ions in the electrode can be ignored so that the the oxygen ion flux equations due to only their diffusion at nodes $(t, n - 1/2)$ and $(t, n + 1/2)$ can be expressed as

$$J_{t,n-1/2}^{O(L)} = -\frac{D_O N_E}{d_E} \left(c_{t,n}^{O(L)} - c_{t,n-1}^{O(L)} \right) \quad (7.34)$$

and

$$J_{t,n+1/2}^{O(L)} = -\frac{D_O N_E}{d_E} \left(c_{t,n+1}^{O(L)} - c_{t,n}^{O(L)} \right), \quad (7.35)$$

respectively. Entering Eqs. 7.34 and 7.35 into Eq. 7.33 leads to the following equation,

$$c_{t+1,n}^{O(L)} = c_{t,n}^{O(L)} + \frac{D_O (N_E - 1)^2 \Delta t}{d_E^2} \left(c_{t,n+1}^{O(L)} - 2c_{t,n}^{O(L)} + c_{t,n-1}^{O(L)} \right). \quad (7.36)$$

Using Eq. 7.36 $c_{t+1,n}^{O(L)}$ can be determined from $c_{t,n-1}^{O(L)}$, $c_{t,n}^{O(L)}$, and $c_{t,n+1}^{O(L)}$. The net oxygen ion flux at the left end of the LE is assumed to be zero, implying the oxygen ions coming into and out of the LE are in equilibrium. Therefore, $J_{t,1/2}^{O(L)} = 0$ serves as the boundary condition at the left end of the LE.⁷ The other boundary condition at $N_E + 1/2$ can be obtained from the net flux of the oxygen ions at the left Helmholtz layer given by Eq. 7.12. Therefore, $J_{t,N_E+1/2}^{O(L)}$ can be expressed as

$$J_{t,N_E+1/2}^{O(L)} = k_-^0 c_{t,N_E}^{O(L)} c_{t,1}^V \exp \left(-\frac{\beta n V_{t,1}}{k_B T} \right) - k_+^0 \left(c_{O_O}^0 - c_{t,1}^V \right) \exp \left[\frac{(1 - \beta) n V_{t,1}}{k_B T} \right]. \quad (7.37)$$

The voltage at the node N_E of the LE is taken as a ground. Considering the short electric field screening length in metal, it is a reasonable assumption to ignore the voltage drop in the LE. $V_{t,1}$ denotes the voltage at node $(t, 1)$, which is at the interface between the left Helmholtz layer and TiO_x . $V_{t,1}$ will be determined from the iteration for the electron distribution calculation in TiO_x . From the discrete diffusion equation and the boundary conditions, that have been dealt with up to now, the oxygen distribution in the LE on each time step can be obtained with a proper initial condition.

The oxygen ion distribution in the RE and its flux at the left and the right ends are obtained using a similar derivation procedure the that used to derive them in the

⁷In fact, $J_{t,1/2}^O$ cannot be defined because $c_{t,0}^O$ does not exist. However, by adding the phantom node at $n = 0$, $J_{t,1/2}^O$ becomes reasonable.

LE. However, the boundary conditions in the RE at the left and the right ends are the other way than those of the LE because the left end of the RE makes an interface with TiO_x . The net flux at the right end of the RE is regarded as zero, $J_{t,N_E+1/2}^{O(L)} = 0$, meaning the oxygen ions coming into and out of the RE are in equilibrium. The boundary condition at the left end of the RE is given by

$$\begin{aligned} J_{t,1/2}^{O(R)} = & -k_-^0 c_{t,1}^{O(R)} c_{t,N_2}^V \exp \left[-\frac{\beta n (V_{ap} - V_{t,N_2})}{k_B T} \right] \\ & + k_+^0 \left(c_{O_O}^0 - c_{t,N_2}^V \right) \exp \left[\frac{(1-\beta) n (V_{ap} - V_{t,N_2})}{k_B T} \right]. \end{aligned} \quad (7.38)$$

The oxygen ion distribution in the RE is obtained using Eq. 7.36 with these boundary conditions.

The calculation of the oxygen vacancy and the electron distributions in TiO_x is more complicated because both drift and diffusion of the oxygen vacancies and the electrons must be taken into account. The discrete drift-diffusion equation of particle i where $i \in \{e, V\}$ at nodes $(t, n+1/2)$ and $(t, n-1/2)$ can be expressed as

$$J_{t,n+1/2}^i = -\frac{1}{2d_2} z_i \mu_i (c_{t,n+1}^i + c_{t,n}^i) (N_2 - 1) (V_{t,n+1} - V_{t,n}) - \frac{N_2 - 1}{d_2} D_i (c_{t,n+1}^i - c_{t,n}^i) \quad (7.39)$$

and

$$J_{t,n-1/2}^i = -\frac{1}{2d_2} z_i \mu_i (c_{t,n}^i + c_{t,n-1}^i) (N_2 - 1) (V_{t,n} - V_{t,n-1}) - \frac{N_2 - 1}{d_2} D_i (c_{t,n}^i - c_{t,n-1}^i), \quad (7.40)$$

respectively. By entering Eqs. 7.39 and 7.40 into Fick's 2nd law given by Eq. 7.30, the equation of $c_{t+1,n}^i$ as a function of c^i and V at nodes $(t, n-1)$, (t, n) , and $(t, n+1)$ can be obtained. V at each node can be evaluated by solving the Poisson equation, which needs space charge density at every node. Therefore, first $c_{t,n}^e$ and $c_{t,n}^V$ should be evaluated at all nodes n at time t . The response of the electrons to the variation of the internal electric field must be very fast compared to the oxygen vacancies, which is attributed to the higher mobility of the electrons. Very small Δt (~ 1 ps) must be used to evaluate the time-dependent behavior of the electrons because their very high mobility and diffusivity. However, the drift-diffusion of the oxygen vacancies is very sluggish compared to the electrons so that its time-constant would be higher than a few hundreds μs relying on the mobility and the diffusivity of the oxygen vacancies. Using Δt (~ 1 ps) is not an efficient method because a huge amount of data points in the time axis are necessary to be produced to calculate the time-dependent drift-diffusion of the oxygen vacancies with such a small Δt . For a more efficient calculation, a quasi-static calculation was used for the evaluation of the electron distribution. In fact, the quasi-static calculation is reasonable because the electrons will reach the steady state at every discrete moment of oxygen vacancy migration, that is, while the electron redistribution occurs, the oxygen vacancies are almost stationary so that the electron redistribution does not affect the migration of the oxygen vacancies. From the discussion up to now the concentration of the oxygen vacancies and the electrons can be defined at all nodes n at time t , and thus the voltage at all nodes n can be evaluated.

In the continuum theory, the voltage distribution in TiO_x as a function of coordinate x shown in Fig. 7.18(a) is given by

$$V(x) = V(d_1) - E(d_1) d - \frac{q}{\varepsilon_r \varepsilon_0} \int_{d_1}^x \int_{d_1}^{x'} \rho(x'') dx'' dx', \quad (7.41)$$

where

$$\begin{aligned} E(d_1) = & -\frac{1}{d_1 \varepsilon_r / \varepsilon_{rH} + d_2 + d_3 \varepsilon_r / \varepsilon_{rH}} \left[V_{ap} + \frac{qd_3}{\varepsilon_{rH} \varepsilon_0} \int_{d_1}^{d_1+d_2} \rho(x') dx' \right. \\ & \left. + \frac{q}{\varepsilon_r \varepsilon_0} \int_{d_1}^{d_1+d_2} \int_{d_1}^x \rho(x') dx' dx \right]. \end{aligned} \quad (7.42)$$

ε_r and ε_{rH} denote the dielectric constant of TiO_x and the Helmholtz layer, respectively. Space charge density ρ is defined as $\rho(x) = 2c^V(x) - c^e(x)$. The derivation of Eqs. 7.41 and 7.42 was shown in Chapter 5. In the FDM, the integration of ρ over x , the second term in the bracket of the right side of Eq. 7.42 can be rewritten using the trapezoidal rule[72] by

$$\int_{d_1}^{d_1+\frac{d_2(n-1)}{N_2-1}} \rho(x') dx' \simeq \frac{d_2}{N_2-1} \left[\sum_{i=2}^{n-1} \rho(i) + \frac{1}{2} \rho(i=1) + \frac{1}{2} \rho(i=n) \right]. \quad (7.43)$$

By defining Eq. 7.43 as $f(i=n)$ the double integral on the right side of Eq. 7.41 can be replaced by

$$\int_{d_1}^{d_1+\frac{d_2(n-1)}{N_2-1}} f(x') dx' \simeq \frac{d_2}{N_2-1} \left[\sum_{i=2}^{n-1} f(i) + \frac{1}{2} f(i=1) + \frac{1}{2} f(i=n) \right]. \quad (7.44)$$

In the same way, the double integral in Eq. 7.42 can be replaced by

$$\int_{d_1}^{d_1+d_2} f(x') dx' \simeq \frac{d_2}{N_2-1} \left[\sum_{i=2}^{N_2-1} f(i) + \frac{1}{2} f(i=1) + \frac{1}{2} f(i=N_2) \right]. \quad (7.45)$$

Therefore, the voltage at all nodes at time t at the given distribution of space charges ρ can be evaluated.

The electron distribution in the steady state with given oxygen vacancy distribution $c_{t,n}^{VO}$ can be determined using the Newton-Raphson iteration. Arbitrary voltage distribution along nodes n at time t ($V_{t,n}^{j=1}, n = 1, 2, \dots, N_2$) is input as the initial condition of the iteration. $\epsilon_F^{j=1}(t, 1)$ is first optimized using the first iteration, giving $\epsilon_F^c(t, 1)$.⁸ As explained in Chapter 5, if $\epsilon_F^c(t, 1)$ is known, $\epsilon_F^c(t, n)$ and $d\epsilon_F^c/dx|_{t,n}$ at all nodes n at time t are evaluated so that all those values can be optimized. From the given $V_{t,n}^{j=1}$ and the optimized $\epsilon_F^c(t, n)$ the concentration of the electrons at node n is evaluated, therefore, $\rho_{t,n}^c$ can be obtained. Using Eqs. 7.41, 7.42, 7.43, 7.44, and 7.45, the voltage distribution $V_{t,n}^c$ ⁹ with the space charge distribution $\rho_{t,n}^c$

⁸The superscript c of $\epsilon_F^c(t, 1)$ means the optimized value at given $V_{t,n}^j$, where $n=1, 2, \dots, N_2$. Since $V_{t,n}^j$ will be also optimized using the second iteration, $\epsilon_F^c(t, 1)$ is not the final $\epsilon_F(t, 1)$ value.

⁹The superscript c means the same as that of $\epsilon_F^c(t, 1)$

Table 7.3: List of symbols

Symbol	Description
$c_{t,n}^O$	Oxygen concentration at node n and time t
$c_{t,n}^V$	Oxygen vacancy concentration at node n and time t
D_O	Diffusivity of an oxygen ion in Pt
D_V	Diffusivity of an oxygen vacancy in TiO_x
d_E	Thickness of Pt
d_1	Thickness of the Helmholtz layer at the LE/ TiO_x interface
d_2	Thickness of TiO_2
d_3	Thickness of the Helmholtz layer at the TiO_x /RE interface
N_E	Number of the nodes in Pt
N_2	Number of the nodes in TiO_2
N_t	Number of the nodes in time dimension
Δt	Time interval

can be evaluated. Function $S^{j=1}$ is defined as $S^{j=1}(i) = V_{t,n}^{j=1} - V_{t,n}^c$ meaning the difference between the input $V_{t,n}^{j=1}$ and the calculated $V_{t,n}^c$. Using the iteration a new set of $V_{t,n}^{j=2}$ obtained from $S^{j=1}$ is input again and the same procedure is repeated. This iteration will continue until $S_{t,n}^j$ at all nodes n becomes smaller than a tolerance (Δ), meaning the convergence on zero. From this procedure the voltage and the electron distributions with given $c_{t,n}^V$ and the boundary conditions, J_L^e and J_R^e , can be obtained.

Calculation of the oxygen vacancy distribution with respect to time

The calculation procedure of the oxygen vacancies along time nodes t given by the following.

- Determination of the oxygen ion distribution in the LE and the RE at time t .
- Determination of $V_{t,n}$ and $\epsilon_F(t, n)$ at all nodes n in TiO_x with $c_{t,n}^V$.
- Determination of $c_{t,n}^e$ at all nodes n in TiO_x from the determined $V_{t,n}$ and $\epsilon_F(t, n)$.
- Determination of the oxygen vacancy flux equations at the interfaces ($J_{t,1/2}^V$ and $J_{t,N_E+1/2}^V$): $J_{t,1/2}^V$ is determined from $c_{t,1}^V$, c_{t,N_E}^O of the LE, and $V_{t,1}$ and $J_{t,N_E+1/2}^V$ is determined from c_{t,N_E}^V , $c_{t,1}^O$ of the RE, and V_{t,N_E} .
- Determination of $c_{t+1,n}^V$ at all nodes n in TiO_x .

7.5.4 Calculation results

As discussed in Chapter 5, one of the two interfaces of Pt/ TiO_2 /Pt should be involved in the BRS to observe the stable BRS behavior. The LE/ TiO_x interface was taken as the active interface for the electrochemical reaction, whereas the other interface was

Table 7.4: Parameters for the BRS calculation

Parameter	Value	Parameter	Value
D_O	$10^{-15} \text{ cm}^2\text{s}^{-1}$ [75]	β	0.45
D_V	$10^{-18} \text{ cm}^2\text{s}^{-1}$	n	-2
d_E	70 nm	h	0.75 eV
d_1	2 Å	s	1.2 meV/K
d_2	50 nm	$c_{O^{2-}}^0$	10^{23} cm^{-3}
d_3	2 Å	ϵ_r	20
N_E	199	ϵ_{rH}	7[77]
N_2	272	ϕ_b	0.5 eV
N_t	5	m_e	10 m ₀
Δt	20 ms	A	$6.25 \text{ cm}\cdot\text{s}^{-1}$
k_{-}^0 at d_1	$10^{-36} \text{ cm}^4\cdot\text{s}^{-1}$	T	298 K
k_{-}^0 at $d_1 + d_2$	$10^{-62} \text{ cm}^4\cdot\text{s}^{-1}$		

considered to be inactive with a low rate constant of the electrochemical reaction. This mainly leads to the change in the oxygen vacancy concentration at the LE/TiO_x interface. The parameters used for the calculation of J - V curves are given in Table 7.4. The Helmholtz layer is believed to be similar to the interfacial dipole layer in semiconductor physics.[76] ϵ_{rH} was assumed to be 7 as Black *et al.* suggested in their paper.[77] The diffusivity of the oxygen vacancies in reduced TiO_x was set to be $10^{-18} \text{ cm}^2\text{s}^{-1}$. As a matter of fact, the diffusivity at room temperature has been barely reported. The diffusivity used for this calculation was guessed from that measured at high temperature (> 1000 °C).[78] The initial oxygen vacancy distribution is shown in Fig. 7.20, where the concentrations at d_1 and $d_1 + d_2$ are 2.35×10^{21} and $5.28 \times 10^{21} \text{ cm}^{-3}$, respectively.

Calculated J - V hysteresis with two cycles is plotted in Fig. 7.21(a). The applied voltage cycle is depicted in the inset. The delay time of each voltage step was 0.1 s. Since the formation and the annihilation of oxygen vacancies at the LE/TiO₂ occur with applying a negative and a positive voltage, respectively, to the RE, thus set and reset switching occurs under negative and positive voltage, respectively as shown in Fig. 7.21(a). The set switching in Fig. 7.21(a) is not very obvious because a gentle decrease in resistance rather than an abrupt decrease takes place during the set switching. The variation of the oxygen vacancy concentration at the LE/TiO₂ interface is shown in Fig. 7.21(b). An increase in the oxygen vacancy concentration during the set switching leads to the reduction of the SBH at the same interface so that current increases with increasing oxygen vacancy concentration. Reset switching occurs under positive voltage as shown in Fig. 7.21(a). The oxygen vacancy concentration at the LE/TiO_x interface decreases in the reset switching voltage region, giving rise to an increase in the SBH. Therefore, the hysteretic J - V behavior can be observed in the reset switching voltage region.

In Fig. 7.21(b) it can be noticed that oxygen vacancy concentration as a function of the applied voltage in the second cycle is not completely identical to that in the first cycle, thus the BRS curves in the first and the second cycles show a slight difference as shown in Fig. 7.21(a). The difference of the oxygen vacancy concentration relying

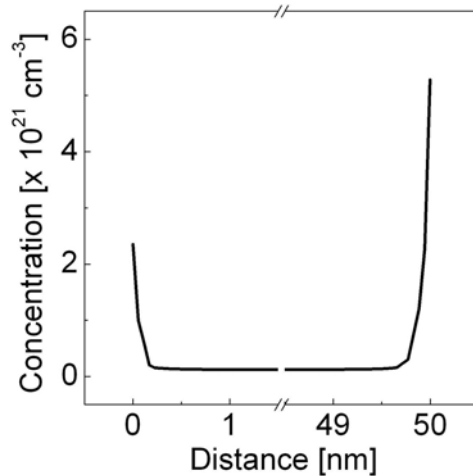


Figure 7.20: Initial distribution of the oxygen vacancies in TiO_x between the LE and the RE.

on the cycle number is due to the variation of the Nernst potential V_n of the oxygen vacancy formation and the annihilation reactions (Eq. 7.3). As given by Eq. 7.14, V_n is a function of the concentration of the oxygen vacancies in TiO_x and the oxygen ions in the LE. V_n indicates equilibrium voltage, that is, when the applied voltage V (d_1) in the Helmholtz layer is equal to V_n , the system reaches equilibrium so that no further changes in the concentration of the ionic species take place. As V (d_1) is further from V_n in the positive (negative) direction, the oxygen vacancy annihilation (formation) reaction, the forward (reverse) of Eq. 7.3, becomes more accelerated. Therefore, the oxygen vacancy and the oxygen ion concentrations and V_n have influence on each other and they show variation in each voltage cycle so that the non-closed loop of the oxygen vacancy concentration with respect to the applied voltage shown in Fig. 7.21(b) was obtained.

The variation of the oxygen vacancy and the oxygen ion concentrations with respect to a cycle number might be the reason for the BRS fatigue shown in Fig. 7.10. In Fig. 7.10 the resistance of the LRS increases with increasing a cycle number, which is comparable to the increase in the resistance of the LRS in the second cycle compared with the first cycle as can be seen in Fig. 7.21(a). The increase in the LRS resistance in Fig. 7.21(a) is attributed to the decrease in the oxygen vacancy concentration of the LRS as can be identified in Fig. 7.21(b). Therefore, the decrease in the oxygen vacancy concentration in the LRS can be regarded as the reason for the fatigue of the BRS.

The SBH at the interface between the cathode and TiO_x with respect to the applied voltage is shown in Fig. 7.22(a). The open symbols on the negative voltage side indicate the SBH at the $\text{TiO}_x/\text{RE}(\text{cathode})$ interface and the closed ones on the positive voltage side indicate the SBH at the LE(cathode)/ TiO_x interface. The hysteretic SBH variation shown in Fig. 7.22(a) plays an essential role in the BRS. Compared with the SBH at the TiO_x/RE interface in the second downward sweep

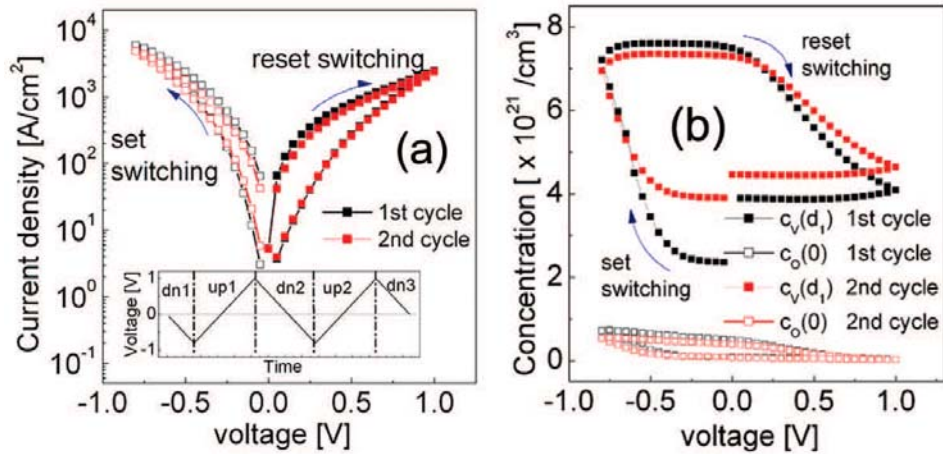


Figure 7.21: (a) Simulated J - V curve with the applied voltage cycle shown in the inset and a voltage delay time of 0.1 s. The open and the closed symbols mean negative and positive currents, respectively. (b) Variation of the oxygen vacancy concentration at d_1 and the oxygen ion concentration at $x = d$ with respect to the applied voltage.

(dn2), the decrease in the SBH in the the second upward sweep (up2) can be identified on the negative voltage side of Fig. 7.22(a). This decrease causes a decrease in resistance (set switching). Under the positive voltage in up2 another hysteretic SBH behavior at the LE/TiO_x interface can be observed. Compared with the SBH under the positive voltage in up1, that in the third downward sweep (dn3) is found to undergo reduction in up2. And this reduction of the SBH thus causes an increase in resistance (reset switching). Figure 7.22(a) also shows very asymmetric SBH in the HRS while the SBH in the LRS is more or less symmetric. The asymmetric SBH in the HRS causes an asymmetric J - V curve in the HRS shown in Fig. 7.21(a).

The conduction band and the Fermi energy profiles at $\pm 0.5V$ in the two cycles are plotted in Fig. 7.22(b). The conduction band edge profiles are flat apart from the interface regions regardless of the applied voltage and the resistance state. This is attributed to the good electric field screening within a short screening length by a large amount of the oxygen vacancies in the vicinity of the interfaces so that almost no voltage is applied in the bulk of TiO_x. Regardless of the applied voltage the Fermi energy is located above the conduction band edge except for that in the vicinity of the two interfaces, meaning the bulk of TiO_x has the much higher conductivity so that the BRS is controlled by the interfaces. This implication is consistent with the generic model suggested by Rozenberg *et al.* [79] The distribution of the electrons in TiO_x with respect to the applied voltage is shown in Fig. 7.23. The decrease in the electron concentration in the vicinity of the RE after the positive maximum voltage (1 V) can be confirmed with being compared with the concentration before 1 V. The electron concentration in the bulk of TiO_x is a constant without depending on the resistance state as well as the applied voltage. However, the variation of the electron distribution, induced by the set switching, is not obvious so that it cannot be seen

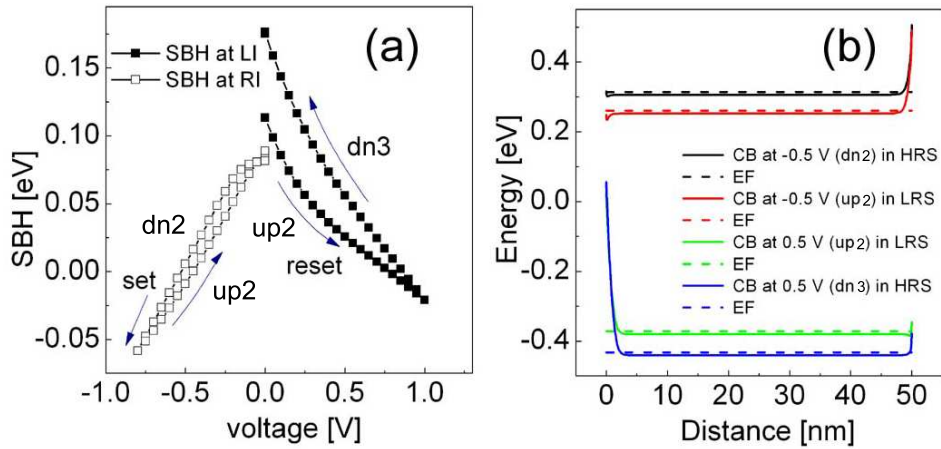


Figure 7.22: (a) Variation of the SBH at the interface between the cathode and TiO_x with respect to the applied voltage in the second cycle. LI and RI mean the LE/ TiO_2 and the TiO_x /RE interfaces, respectively. (b) Simulated profiles of the conduction band edge and the Fermi energy at -0.5 V during the second downward sweep (dn2), -0.5 V and 0.5 V during the second upward sweep (up2), and 0.5 V during the third downward sweep (dn3) in the second cycle. The Fermi energy of the LE is taken as a reference energy.

in Fig. 7.23.

The time-dependent variation of the current density under two different constant voltages (0.7 and 0.8 V) is plotted in Fig. 7.24(a). The parameters given in Table 7.4 were used for the calculation of the current density-time ($J-t$) behavior. These voltages belong to the reset switching regime so that J decreases with respect to time. The $J-t$ behavior shown in Fig. 7.24(a) is consistent with the measured $I-t$ behavior, undergoing the reset switching as shown in Fig. 7.16.

The time-dependent variation of the concentration of the oxygen vacancies in the vicinity of the LE/ TiO_x interface at 0.7 V is plotted in Fig. 7.24(b). Since at 0.7 V the reset switching, that is, the annihilation of the oxygen vacancies, takes place, a number of the oxygen vacancies decrease with respect to time. Figures 7.24(c) and (d) depict the variations of the electron concentration and the conduction band minimum profile, respectively, with respect to time at 0.7 V.

$J-V$ curves calculated using two different formation energies h (0.75 and 0.9 eV) and the corresponding concentrations of the oxygen vacancies at the LE/ TiO_x interface are plotted in Figs. 7.25(a) and (b), respectively. The applied voltage cycle is depicted in the inset of Fig. 7.25(a). The formation energy h determines the set voltage and the reset voltage. As shown in Fig. 7.25, the higher formation energy shifts the set and the reset voltage regimes to higher voltages. The voltage regimes where the vacancy concentration increases and decreases are regarded as the set and the reset regimes, respectively. Therefore, the higher formation energy leads to the set switching even under the positive voltage as shown in the increase in the vacancy concentration in the voltage range ($0 \text{ V} < V_{ap} < 0.25 \text{ V}$) during the downwards

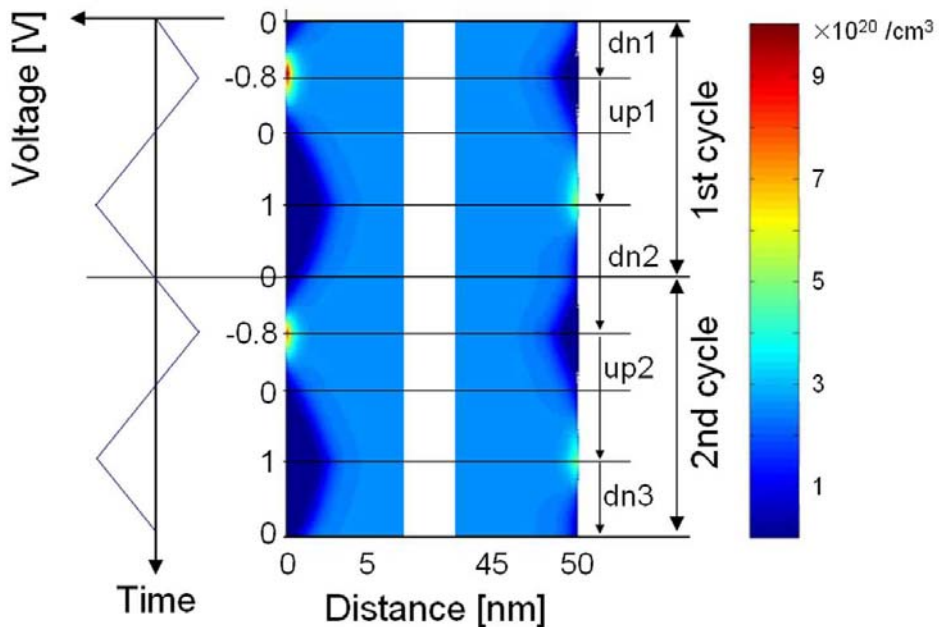


Figure 7.23: Electron distribution in TiO_x between the LE and the RE with respect to the applied voltage to the RE.

sweep dn2. On the other hand, if the formation energy is much smaller than 0.75 eV, the reset switching voltage shifts to the negative voltage so that the reset switching occurs even under the negative voltage. For instance, the theoretical formation energy (0.47 eV) gives rise to the BRS behavior where both set and reset switchings take place under the negative voltage, and thus the BRS behavior is not consistent with the BRS measured experimentally.

The relation between the formation energy energy and the switching voltage can be explained by the applied voltage in the Helmholtz layer. The formation energy under the applied voltage h' is given by a function of the voltage at the right end of the Helmholtz layer, $h' = h - 2V(d_1)$. Due to the high concentration of the oxygen vacancies at the LE/ TiO_x interface, a high negative electric field is applied in the Helmholtz layer even at 0 V, and thus $V(d_1)$ is positive at 0 V. In case of a formation energy of 0.9 eV, the forward reaction (annihilation of the oxygen vacancies) is retarded by the high formation energy so that the reverse reaction (formation of the oxygen vacancies) is dominant under the negative voltage as well as the positive voltage in the range ($0 \text{ V} < V_{ap} < 0.25 \text{ V}$). In case of a formation energy of 0.75 eV, the forward and the reverse reactions are balanced in the lower voltage so that the reverse reaction becomes prominent under the only negative voltage. Therefore, the set switching and the reset switching can be achieved by the negative voltage and the positive voltage, respectively.

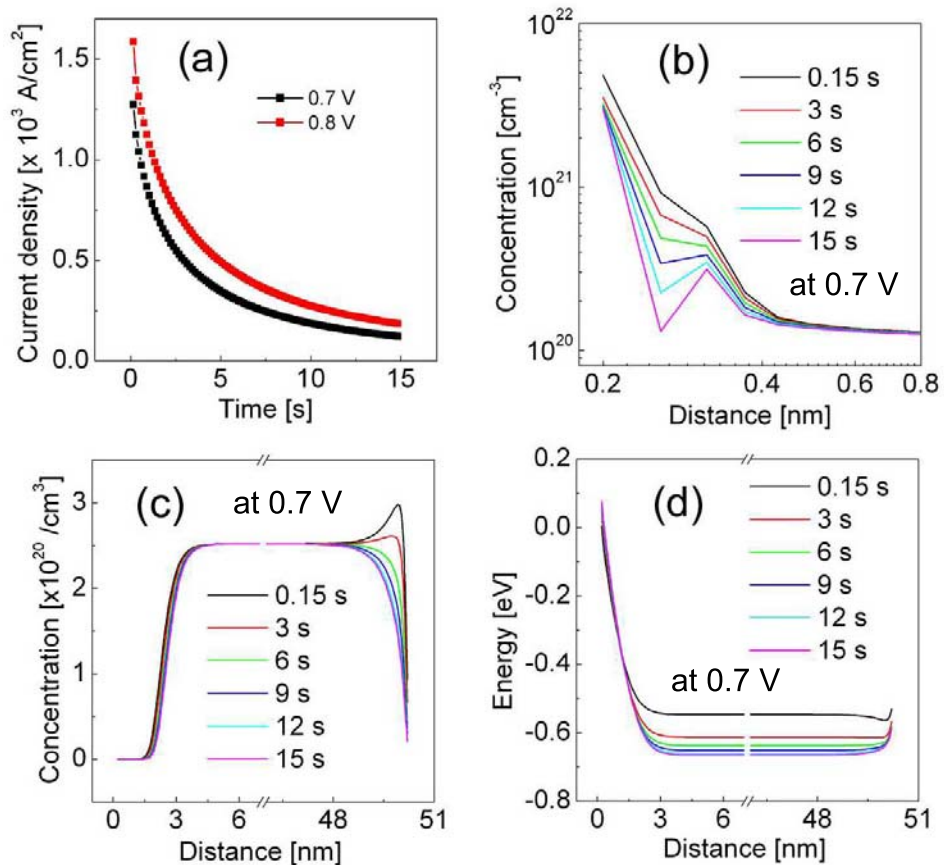


Figure 7.24: (a) J - t curves under applied voltages of 0.7 and 0.8 V, undergoing a reset switching. (b) Time-dependent distribution of the oxygen vacancies in the vicinity of the LE/ TiO_x interface at 0.7 V. Time-dependent variation of (c) the electrons and (d) the conduction band minimum profile in TiO_x at 0.7 V. In Fig. (d) the Fermi energy of the LE is taken as 0 eV.

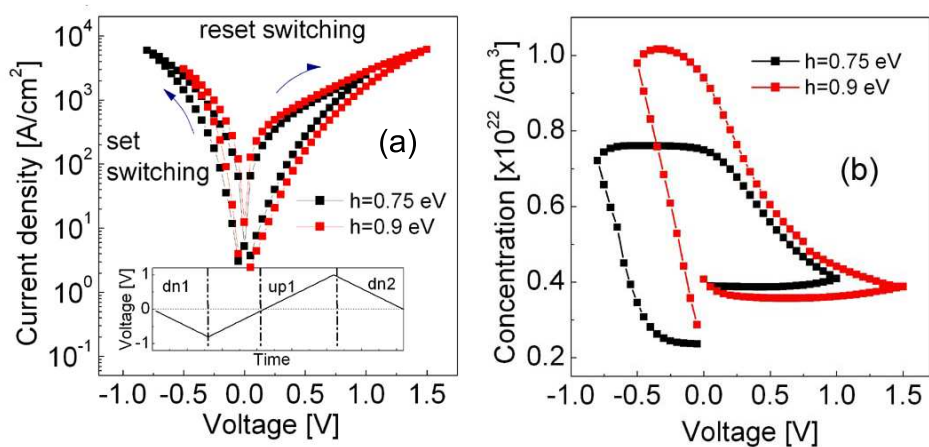


Figure 7.25: (a) J - V curves calculated using a formation energy h of 0.75 and 0.9 eV. The inset depicts the applied voltage cycle. (b) Corresponding concentrations of the oxygen vacancies at the LE/TiO_x interface.

Summary

The electric conduction behavior in Pt/TiO₂/Pt switching cells was characterized for three different resistance statuses of TiO₂, i.e. pristine, unipolar resistive switching (URS)-activated, and bipolar resistive switching (BRS)-activated status. The characterized conduction behavior was interpreted in terms of the oxygen ions/vacancies migration due to the drift-diffusion. This work involved both experimental and theoretical investigations.

For all three resistance statuses of TiO₂ current-voltage (*I*-*V*) hysteresis was observed. The pristine status showed volatile *I*-*V* hysteresis, implying the resistance underwent easy relaxation with respect to time. The relaxation was considered to be attributed to the relaxation of ions, which was in a good agreement with the characterized impedance spectra in a low frequency domain. The URS-activated and the BRS-activated statuses gave non-volatile *I*-*V* hysteresis indicating two characteristic resistance states, a high resistance state (HRS) and a low resistance state (LRS).

From the experimental point of view, the main achievement was the understanding of the role of oxygen ions in the electroforming and the BRS. Some important evidences revealing the role of oxygen ions in the electroforming were obtained from the structural changes induced by the electroforming and their voltage polarity dependence. The atmosphere dependence of the electroforming also revealed oxygen ions to play an important role in the electroforming. Furthermore, some chemical analysis proved that the non-homogeneous evolution of oxygen gas over the electroformed switching cell occurred during the electroforming. The non-homogeneous evolution of oxygen gas might indirectly show the non-uniform distribution of conductivity, implying that local conduction paths are in existence. The atmosphere dependence of the BRS behavior revealed the influence of the oxygen-related electrochemical reaction at a Pt/TiO_x interface on the BRS behavior.

From the theoretical point of view, the main accomplishment was to suggest the mechanism of the electric conduction in the electroformed cell and in the BRS-status in terms of the variation of the Schottky barrier height (SBH) at the Pt/TiO_x interface. The variation of the SBH results from the change in the oxygen vacancy concentration at the interface. For the description of the conduction behavior in the electroformed cell, the simulated *I*-*V* curves were well consistent with the experimental data and the suggested model nicely explained the several tendencies obtained from the experiments. For the description of the BRS behavior, the voltage and time-dependent distribution of the oxygen vacancies and the electrons in TiO_x was calculated using the finite difference method with taking into account the oxygen-related electrochemical reaction at a Pt/TiO_x interface. From the calculation of the time-dependent distribution of electrons and oxygen vacancies, the *I*-*V* hysteresis

showing the BRS characteristics was obtained.

Despite of these achievements, there are still many open questions about the electroforming as well as the BRS.

- The mechanism of the oxygen incorporation into Pt. As mentioned in Chapter 5, switching cells with 10 or 30 nm thick TE showed the destruction of the TE due to the evolution of oxygen gas, whereas cells with 70 nm thick TE showed no destruction of the TE. This might be due to the solubility of oxygen gas in Pt depending on the Pt thickness. However, the thickness dependence of the solubility has not been proven yet.
- The effect of external oxygen on the electroforming. The chemical oxidation of reduced $\text{Ti}^{(4-n)+}$ at the interface between the top electrode (TE) and TiO_x by virtue of the external oxygen was found to have influence on the electroforming behavior. However, the electroformed switching cells did not show the large variation of the resistance in spite of the chemical oxidation taking place at the TE/ TiO_2 interface. Therefore, the detail of the chemical oxidation should be clarified.
- The physical properties of the TiO_x phase. For instance, the electron mobility, the oxygen vacancy diffusivity, the electron effective mass, etc., should be evaluated to describe the BRS behavior precisely. And the electron band structure including the electron affinity and the location of the Fermi energy are also necessary for the description of the electric potential distribution.
- The physical properties of the Helmholtz layer at the Pt/ TiO_x interface. In order to describe the electrochemical reaction and the electric potential distribution in Pt/ TiO_x /Pt, the physical properties of the Helmholtz layer including the thickness and the dielectric constant should be known.

Outlook

The nature of the conduction paths in TiO_2 should be clarified. X-ray photoemission spectroscopy or Raman spectroscopy with very small incident beam diameter ($\sim \text{nm}$) would be helpful to shed light on the investigation on the electronic structure of the conduction paths. Using the conventional spectroscopy with large beam diameter obtaining the information of the localized conduction paths is quite limited because of the interference by the signal from the TiO_2 phase out of the conduction paths. Second, the source of the oxygen incorporated into the electrode is necessary to be more clearly identified. Oxygen isotope, for instance, O18, experiments would be a nice method to confirm the origin of the incorporated oxygen. For instance, by identifying the oxygen isotope contained in the electrode of electroformed Pt/ TiO_2 /Pt cells with TiO_2 grown with O18 gas, the origin of the incorporated oxygen can be clarified. Third, the first principle calculation of the oxygen vacancy formation energy at a Pt/ TiO_2 interface is needed to be obtained for the precise description of the oxygen ion/vacancy-related electrochemical reaction rate.

The effect of external oxygen on the BRS of TiO_2 can be identified by taking the oxygen flux entering into the Pt top electrode (TE) as a boundary condition for the drift-diffusion of oxygen ions in the TE. The incorporation of external oxygen into the TE can be described by several reaction steps, i.e. the chemisorption of oxygen molecules on the TE, the decomposition of the oxygen molecules, and their migration to the TE/ TiO_2 interface. Using this boundary condition the BRS behavior influenced by external oxygen can be simulated.

Bibliography

- [1] F. Argall, Solid-State Electron. **11**, 535 (1968).
- [2] B. J. Choi, D. S. Jeong, S. K. Kim, C. Rohde, S. Choi, J. H. Oh, H. J. Kim, C. S. Hwang, K. Szot, R. Waser, B. Reichenberg, and S. Tiedke, J. Appl. Phys. **98**, 033715 (2005).
- [3] D. S. Jeong, H. Schroeder, and R. Waser, Appl. Phys. Lett. **89**, 082909 (2006).
- [4] J. F. Gibbons and W. E. Beadle, Solid-State Electron. **7**, 785 (1964).
- [5] C. B. Lee, B. S. Kang, M. J. Lee, S. E. Ahn, G. Stefanovich, W. X. Xianyu, K. H. Kim, J. H. Hur, H. X. Yin, Y. Park, I. K. Yoo, J.-B. Park, and B. H. Park, Appl. Phys. Lett. **91**, 082104 (2007).
- [6] T. W. Hickmott, J. Vac. Sci. Tech. **6**, 828 (1969).
- [7] C. Rossel, G. I. Meijer, D. Bremaud, and D. Widmer, J. Appl. Phys. **90**, 2892 (2001).
- [8] H.-S. Lee, J. A. Bain, S. Choi, and P. A. Salvador, Appl. phys. Lett. **90**, 202107 (2007).
- [9] J. R. Contreras, H. Kohlstedt, U. Poppe, R. Waser, C. Buchal, and N. A. Pertsev, Appl. Phys. Lett. **83**, 4595 (2003).
- [10] K. Szot, W. Speier, G. Bihlmayer, and R. Waser, Nature Materials **5**, 312 (2006).
- [11] R. Waser (Ed.), *Nanoelectronics and Information Technology* (Wiley-VCH, Weinheim, 2003), p. 526
- [12] A. Beck, J. G. Bednorz, C. Gerber, C. Rossel, and D. Widmer, Appl. Phys. Lett. **77**, 139 (2000).
- [13] M. Kund et al., IEDM Tech. Digest, 754 (2005).
- [14] Y. Hirose and H. Hirose, J. Appl. Phys. **47**, 2767 (1976).
- [15] C. Schindler, S. C. Puthen Thermadam, M. N. Kozicki, and R. Waser, IEEE Trans. Electron Dev.
- [16] T. W. Hickmott, J. Appl. Phys. **33**, 2669 (1962).
- [17] M. Janousch *et al.* Adv. Mater. **19**, 2232 (2007).

- [18] Y. B. Nian, J. Strozier, N. J. Wu, X. Chen, and A. Ignatiev, Phys. Rev. Lett. **98**, 146403 (2007).
- [19] T. Fujii, M. Kawasaki, A. Sawa, Y. Kawazoe, H. Akoh, and Y. Tokura, Phys. Rev. B **75**, 165101 (2007).
- [20] R. Waser and M. Aono, Nature Mater. **6**, 833 (2007).
- [21] R. Pinto, Phys. Lett. A **35**, 155 (1971).
- [22] R. P. Beaulieu, D. V. Sulway, and C. D. Cox, Solid-State Electron. **3**, 428 (1973).
- [23] K. Kinoshita, T. Tamura, M. Aoki, Y. Sugiyama, and H. Tanaka, Appl. Phys. Lett. **89**, 103509 (2006).
- [24] K. M. Kim, B. J. Choi, Y. C. Shin, S. Choi, C. S. Hwang, Appl. Phys. Lett. **91**, 012907 (2007).
- [25] R. Oligschlaeger, R. Waser, R. Meyer, S. Karthäuser, and R. Ditmann, Appl. Phys. Lett. **88**, 042901 (2006).
- [26] D. S. Jeong, H. Schroeder, and R. Waser, Electrochem. Solid-State Lett. **10**, G51 (2007).
- [27] S. Springer, Ph. D. thesis, École Polytechnique Fédérale de Lausanne, Switzerland (2004).
- [28] Theo Hahn, T. Hahn, *International Table for Crystallography*, 5th ed. (Springer, Dordrecht, 2005).
- [29] M. Horn, C. F. Schwerdtfeger, and E. P. Meagher, Zeitschrift für Kristallographie **136**, 273 (1972).
- [30] P. G. Wahlbeck and P. W. Giles, J. Am. Ceram. Soc. **49**, 180 (1966).
- [31] M. Marezio and P. D. Dernier, J. Solid state chem. **3**, 340 (1971).
- [32] L. Kihlborg and I. Olovsson, Acta Cryst. A **53**, 103 (1997).
- [33] H. K. Ardakani, Thin Solid Films **248**, 234 (1994).
- [34] M. Shirkhanzadeh, J. Mat. Sci. Mater. Med. **6**, 206 (1995).
- [35] D. S. Jeong and C. S. Hwang, J. Appl. Phys. **98**, 113701 (2005).
- [36] D. S. Jeong, H. B. Park, and C. S. Hwang, Appl. Phys. Lett. **86**, 072903 (2005).
- [37] C. R. Crowell and S. M. Sze, Solid-State Electron. **9**, 1035 (1966).
- [38] J. D. Baniecki, T. Shioga, and K. Kurihara, Mater. Res. Soc. Symp. Proc. **748**, 441 (2003).
- [39] G. W. Dietz and R. Waser, Integrated Ferroelectrics **2**, 317 (1995).

- [40] P. Kofstad, *J. Phys. Chem. Solids* **23**, 1579 (1962).
- [41] K. S. Förland, *Acta Chem. Scand.* **18**, 1267 (1964).
- [42] U. Balachandran and N. G. Eror, *J. Mater. Sci.* **23**, 2676 (1988).
- [43] E. H. Greener *et al.* *J. Am. Ceram. Soc.* **48**, 623 (1965).
- [44] D. S. Jeong, K. H. Ahn, W. Y. Park, and C. S. Hwang, *Appl. Phys. Lett.* **89**, 94 (2004).
- [45] W. Heywang, *Solid-State Electron.* **3**, 51 (1961).
- [46] J. D. Baniecki, R. B. Laibowitz, T. M. Shaw, P. R. Duncombe, D. A. Neumayer, D. E. Kotecki, H. Shen, and Q. Y. Ma, *Appl. Phys. Lett.* **72**, 498 (1998).
- [47] J. Curie, *Ann. Chim. Phys.* **18**, 203 (1889).
- [48] E. von Schweidler, *Ann. Phys.* **24**, 711 (1907).
- [49] C. H. Hamann, A. Hamnett, and W. Vielstich, *Electrochemistry*, 2nd ed. (Wiley-VCH, Weinheim, 2007).
- [50] A. K. Jonscher, *Dielectric Relaxation in Solids*, (Chelsea Dielectric Press, London, 1983).
- [51] R. Jung, M.-J. Lee, S. Seo, D. C. Kim, G.-S. Park, K. Kim, S. Ahn, Y. Park, I.-K. Yoo, J.-S. Kim, and B. H. Park, *Appl. Phys. Lett.* **91**, 022112 (2007).
- [52] D. C. Kim *et al.* *Appl. Phys. Lett.* **88**, 202102 (2006).
- [53] V. E. Henrich and P. A. Cox, *The Surface Science of Metal Oxides*, 1st ed., (Cambridge University Press, Cambridge, 1994).
- [54] I. G. Baek, D. C. Kim, M. J. Lee, H.-J. Kim, E. K. Kim, M. S. Lee, J. E. Lee, S. E. Ahn, S. Seo, J. H. Lee, J. C. Park, Y. K. Cha, S. O. Park, H. S. Kim, I. K. Yoo, U-In Chung, J. T. Moon, and B. I. Ryu, Technical Digest-International Electron Devices Meeting
- [55] C. H. Tung, K. L. Pey, L. J. Tang, M. K. Radhakrishnan, W. H. Lin, F. Ralumbo, and S. Lombardo, *Appl. Phys. Lett.* **83**, 2223 (2003).
- [56] K. L. Pey, C. H. Tung, L. J. Tang, W. H. Lin, and M. K. Radhakrishnan, *Appl. Phys. Lett.* **83**, 2940 (2003).
- [57] T. W. Hickmott, *J. Appl. Phys.* **35**, 2678 (1964).
- [58] J. G. Simmons and R. R. Verderber, *Proc. Roy. Soc. A* **301**, 77 (1967).
- [59] R. R. Verderber, J. G. Simmons, and B. Eales, *Phil. Mag.* **16**, 1049 (1967).
- [60] P. D. Greene, E. L. Bush, and I. R. Rawlings, *Proc. Symp. on Deposited Thin Film Dielectric Materials*, Montreal, Ed. F. Vratny (New York: The Electrochemical Society, 1969), p. 167 (1968).

- [61] G. Dearnaley, *Thin Solid Films* **3**, 161 (1969).
- [62] E. Cho, S. Han, H.-S. Ahn, K.-R. Lee, S. K. Kim, and C. S. Hwang, *Phys. Rev. B* **73**, 193202 (2006).
- [63] K. C. Park and S. Basavaiah, *J. Non-Cryst. Solids* **2**, 284 (1970).
- [64] K. Kinoshita, T. Tamura, H. Aso, H. Noshiro, C. Yoshida, M. Aoki, Y. Sugiyama, and H. Tanaka, *IEEE Non-Volatile Semiconductor Workshop* 2006.
- [65] B.-S. Jeong, D. P. Norton, and J. D. Budai, *Solid-State Electron.* **47**, 2275 (2003).
- [66] B. J. Choi, S. Choi, K. M. Kim, Y. C. Shin, and C. S. Hwang, *Appl. Phys. Lett.* **89**, 012906 (2006).
- [67] R. Waser, *Integrated Ferroelectrics* **15**, 39 (1997).
- [68] K. Szot, W. Speier, and W. Eberhardt, *Appl. Phys. Lett.* **60**, 1190 (1992).
- [69] W. X. Li, L. Österlund, E. K. Vestergaard, R. T. Vang, J. Matthiesen, T. M. Pedersen, E. Lægsgaard, B. Hammer, and F. Besenbacher, *Phys. Rev. Lett.* **93**, 146104 (2004).
- [70] D. Schroeder, in *Proceedings of the 4th International Conference on Simulation of Semiconductor Devices and Processes*, Zurich, edited by W. Fitchner and D. Aemmer (Hatung-Gorre, Konstanz, 1991), p. 313.
- [71] W. H. Press, S. A. Teukolsky, W. T. Vetterling, and B. P. Flannery, *Numerical Recipes in C: The Art of Scientific Computing*, 2nd ed. (Cambridge University Press, 1992).
- [72] E. Kreyszig, *Advanced Engineering Mathematics*, 8nd ed. (Wiley, New York, 1999), p. 870.
- [73] R. Merkle and J. Maier, *Phys. Chem. Chem. Phys.* **4** (17), 4140 (2002).
- [74] K. W. Morton and D. F. Mayers, *Numerical Solution of Partial Differential Equations, An Introduction*, (Cambridge University Press, 2005).
- [75] L. R. Velho and R. W. Bartlett, *Metal. Trans.* **3**, 65 (1972).
- [76] S. M. Sze, *Physics of semiconductor devices*, (Wiley, New York, 2007).
- [77] C. T. Black and J. J. Black, *IEEE Trans. Electron Devices* **ED-46**, 776 (1999).
- [78] D.-K. Lee and H.-I. Yoo, *Solid State Ionics* **177**, 1 (2006).
- [79] M. J. Rozenberg, I. H. Inoue, and M. Sanchez, *Phys. Rev. Lett.* **92**, 178302 (2004).

Curriculum vitae

Name	Doo Seok Jeong
Born	August 17th in Donghae-si, South Korea
Nationality	Korean
Address	Marktstrasse 10, 52428 Jülich, Germany
E-mail address	d.s.jeong@fz-juelich.de

Education

03.1987 - 02.1993	Moungyoun elementary school in Wonju
03.1993 - 02.1996	Hakseong middle school in Wonju
03.1996 - 02.1999	Wonju high school in Wonju
03.1999 - 08.2002	Seoul National University: B.S. in School of Materials Science and Engineering
09.2002 - 02.2005	Seoul National University: M.S. in School of Materials Science and Engineering under the supervision of Prof. Cheol Seong Hwang
04.2005 - 08.2008	Ph.D student at Research center Jülich in support of DAAD (Deutscher Akademischer Austausch Dienst) scholarship under the supervision of Prof. Rainer Waser of RWTH Aachen

Professional experience

07.2004 - 10.2004	Visiting research scientist in Fujitsu lab. in Japan
-------------------	--

Languages	First language Korean, fluent in English, basics in German
-----------	--

Publications

- Doo Seok Jeong, Kun Ho Ahn, Woo Young Park, and Cheol Seong Hwang, Appl. Phys. Lett. **84**, 94 (2004).
- Tae Joo Park, Doo Seok Jeong, Cheol Seong Hwang, Min Soo Park, and Nam-Seok Kang, Thin Solid Films **471**, 236 (2005).
- Chihoon Lee, Jihoon Choi, Moonju Cho, Doo Seok Jeong, Cheol Seong Hwang,

and Hyeong Joon Kim, *Appl. Phys. Lett.* **84**, 2868 (2004).

- Moonju Cho, Doo Seok Jeong, Jaehoo Park, Hong Bae Park, Suk Woo Lee, Tae Joo Park, Cheol Seong Hwang, Gi Hoon Jang, and Jaehack Jeong, *Appl. Phys. Lett.* **85**, 5953 (2004).
- Jaehoo Park, Moonju Cho, Hong Bae Park, Tae Joo Park, Suk Woo Lee, Sug Hoon Hong, Doo Seok Jeong, Chihoon Lee, Jihoon Choi, and Cheol Seong Hwang, *Appl. Phys. Lett.* **85**, 5965 (2004).
- Doo Seok Jeong, and Cheol Seong Hwang, *Phys. Rev. B* **71**, 165327 (2005).
- Doo Seok Jeong, Hong Bae Park, and Cheol Seong Hwang, *Appl. Phys. Lett.* **86**, 072903 (2005).
- Doo Seok Jeong, and Cheol Seong Hwang, *J. Appl. Phys.* **98**, 113701 (2005).
- C. Rohde, B. J. Choi, D. S. Jeong, S. Choi, J.-S. Zhao, and C. S. Hwang, *Appl. Phys. Lett.* **86**, 262907 (2005).
- W. D. Kim, G. W. Hwang, O. S. Kwon, S. K. Kim, M. Cho, D. S. Jeong, S. W. Lee, M. H. Seo, C. S. Hwang, Y.-S. Min, and Y. J. Cho, *J. Electrochem. Soc.* **152**, C552 (2005).
- B. J. Choi, D. S. Jeong, S. K. Kim, C. Rohde, S. Choi, J. H. Oh, H. J. Kim, C. S. Hwang, K. Szot, R. Waser, B. Reichenberg, S. Tiedke, *J. Appl. Phys.* **98**, 033715 (2005).
- D. S. Jeong, C. S. Hwang, J. D. Baniecki, T. Shioga, K. Kurihara, N. Kamehara, and Ishi, *Appl. Phys. Lett.* **87**, 232903 (2005).
- S. H. Hong, J. H. Jang, T. J. Park, D. S. Jeong, M. Kim, and C. S. Hwang, *Appl. Phys. Lett.* **87**, 152106 (2005).
- Doo Seok Jeong, Byung Joon Choi, and Cheol Seong Hwang, *J. Appl. Phys.* **100**, 113724 (2006).
- Doo Seok Jeong, Herbert Schroeder, and Rainer Waser, *Appl. Phys. Lett.* **89**, 082909 (2006).
- K.-M. Kim, B. J. Choi, B. W. Koo, S. Choi, D. S. Jeong, and C. S. Hwang, *Electrochemical and Solid-State Lett.* **9**, G343 (2006).
- K.-M. Kim, B. J. Choi, D. S. Jeong, C. S. Hwang, and S. Han, *Appl. Phys. Lett.* **89**, 162912 (2006).

- Doo Seok Jeong, Herbert Schroeder, and Rainer Waser, *Electrochemical and Solid-State Lett.* **10**, G51 (2007).
- Herbert Schroeder and Doo Seok Jeong, *Microelectronic Engineering* **84**, 1982 (2007).

Schriften des Forschungszentrums Jülich
Reihe Information / Information

1. **Ferrocenes as Potential Building Blocks for Molecular Electronics**
Self-Assembly and Tunneling Spectroscopy
by L. Müller-Meskamp (2008), 153 pages
ISBN: 978-3-89336-509-8
2. **Magnetic Proximity Effects in Highly-ordered Transition Metal Oxide Heterosystems studied by Soft x-Ray Photoemission Electron Microscopy**
by I. P. Krug (2008), XX, 180 pages
ISBN: 978-3-89336-521-0
3. **Seltenerd-basierte ternäre Oxide als alternative Gatedielektrika**
von J. M. Roeckerath (2008), 148 Seiten
ISBN: 978-3-89336-543-2
4. **Strominduzierte Magnetisierungsdynamik in einkristallinen Nanosäulen**
von R. Lehndorff (2009), I, 86 Seiten
ISBN: 978-3-89336-564-7
5. **Magnetization Dynamics in Magnetically Coupled Heterostructures**
von A. Kaiser (2009), X, 121 Seiten
ISBN: 978-3-89336-577-7
6. **Resistive switching in Pt/TiO₂/PT**
by D. S. Jeong (2009), vii, 133 pages
ISBN: 978-3-89336-579-1

